



國立中山大學材料與光電科學學系

博士論文

Department of Materials and Optoelectronic Science

National Sun Yat-sen University

Doctorate Dissertation

低維度應力對寬能隙單晶半導體的機性和光電特性影響

Mechanical and Optoelectronic Response of Wide Band Gap

Semiconductors under Low Dimensional Stress

研究生：宋大豪 撰

Welson Ta-Hao Sung

指導教授：黃志青博士

Dr. Jacob Chih-Ching Huang

中華民國 一百零一年 十二月

December 2012



國立中山大學研究生學位論文審定書

本校材料與光電科學學系博士班

研究生宋大豪（學號：D973100014）所提論文

低維度應力對寬能隙單晶半導體的機性和光電特性影響
Mechanical and Optoelectronic Response of Wide Band Gap
Semiconductors under Low Dimensional Stress

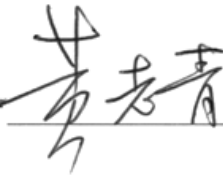
於中華民國 101 年 12 月 12 日經本委員會審查並舉行口試，符合博士學位論文標準。

學位考試委員簽章：

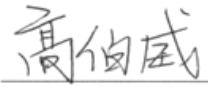
召集人 周明奇



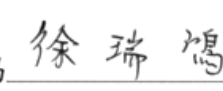
委員 黃志青



委員 高伯威



委員 徐瑞鴻



委員 簡騰瑞



委員

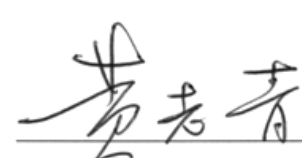
委員

委員

委員

委員

指導教授(黃志青)



(簽名)

謝誌

十年，從大學部一路念上來到博士畢業才有資格寫的這個謝誌，真提筆時卻不知該從何處謝起，原本想著：要謝的人太多了，不如寫個「謝天」就帥氣作結，然而寒窗數載幾經波折，如果不是這些貴人，現在的我可能還在學海裡浮沈。在這人生中的一個重要頓點，我想在這裡表達最誠摯的謝意：

首先我要感謝家人們給我的支持，蛋頭老爸感謝你給我這個書蠹蟲從小鐵與血的教育，鍛鍊我的心智上能在逆境中堅持、在唸書之餘完成三項鐵人、全程馬拉松、衝浪、龍舟金牌…等等，能讓你覺得驕傲的事情就是我會去做的事，你老是掛在嘴邊「生命的意義在於創造宇宙繼起之生命」，而我存在的意義就是超越你，讓你以我為榮。我也要感謝堅強的媽媽，謝謝妳在我叛逆的時候沒有放棄我，妳犧牲掉所有人生中該享樂的時間去照顧家人，讓我們能無後顧之憂的成長並唸完學位，妳用身教告訴我們什麼是孝順與無怨無悔的付出，並教導我們無論在怎樣的困境中都要記得笑，畢業後最大的心願是帶妳環遊世界！感謝我兩個姊姊 Misty & Alice 對我這個么弟老是存著不知道哪裡來的信心，妳們在各自領域裡的努力就是對我的砥礪。

再來要感謝我的指導教授黃志青老師，感謝您這十年來耐心地提攜我這個問題學生，讓一頭藍髮的班代參加的您的秘密結社、碩一偷跑出國打辯論、論文計畫口試前一天在校內搞學運、博班還在實驗室裡組樂團，感謝您常忍著高血壓上升的風險改我大小錯不斷的論文，願意拉拔我到現在還沒踢出實驗室。謝謝老師在家裡出事的時候給我極大的空間與諒解，讓我能在學業與家庭衝突時不放棄的走出一條路來。我想這都要感謝老師，您不懈的努力與對研究上的熱情一直都是我心目中的表率，期望日後的表現將不愧於您創立第一屆材光系的首位博士生。此外，要感謝美國田納西大學的聶台岡教授，來台半年的時間給予我研究上莫大

的討論與幫助，不管是對科學的態度或是追求人生上的目標，都讓我瞻仰到國際級大師的風範。系上徐瑞鴻老師在光電物理方面提共熱心與細心的指導使我獲益良多，願意讓我擔任教學助理讓自己在就讀研究所時能不依靠家裡自食其力。還有義守大學的簡贍瑞教授亦師亦友的關係，除了提供研究的題目找出實驗方向之外，像個大學長一樣不斷鼓勵並指導我。也感謝系上老師與系辦小姐，從大學部以來對我的幫助與包容，謝謝你們！

最後，要感謝好朋友小易，從大一室友到決定念博班，幾乎所有做過的好事壞事都有你一份，我的好對手與好伙伴，很高興求學時的夢想能和你一起實現。會救人的 Dr. 陳，你對自己目標無畏地堅持與對哲學的思考激發我對自己的要求，感謝你不時的當聆聽者並適時的給予我支持。土地、阿強、大姊頭、大眼睛、喜孜孜，謝謝你們這群好朋友在我最需要幫助的時候，有源源不絕的能量堅持住。還有實驗室裡許多學長們是我學習的目標，會走路的百科全書大神學長教導我博學與行萬里路的重要、有杰與宇庭學長遠負國外求學工作優異表現、家爸子翔學長跟我分享博班的心路歷程、敬仁學長教我對實驗的嚴謹與自我要求、炎暉學長教我超高 EQ 的自我控制、斯威特學長與 KB 浩然學長教我待人處事的道理。一起在中山努力的肌溝、小雞、大牛以及材光第一屆老同學們、現在成為實驗室不可或缺的棟梁阿官、碩士就發 APL 的 BASS 手婷子、還在努力的 GT 安迪、準備接手光電組的 Nick 以及實驗室優秀的學弟妹們，謝謝這段時間裡你們對我的幫助與陪伴，雖然你們不一定會看到，但是我想你們應該都能感受得到，我愛你們！（抱）

給自己：博士畢業，只是人生中的一個頓點，日後你可能會一再回顧這段求學時光，這段你對未來迷惘，探索著一條屬於自己的路並不斷地嘗試改變自己，期許成為更好的人、能幫助更多的人。我希望未來的你，能找到每天早晨起床的意義以及願意奉獻的目標。我希望你正在做對的而且快樂的事情，因為這兩者是不衝突的。我希望你記得自信不是你現在擁有著什麼，而是你相信著自己，相信

上天不會給人過不去的坎，在接下來的路程都能鼓起勇氣面對。記得，要做自己！

Aint busying living, Aint busying dying.

Wen Sun.

December, 2012 於中山西子灣

Content

Content	I
List of tables	V
List of figures	VII
Abstract	XIV
中文摘要	XVI
Chapter 1. Introduction	1
1.1. GaN.....	1
1.2. ZnO.....	2
1.3. Other wide band gap semiconductors.....	3
1.4. Motivations.....	4
Chapter 2. Background and literature review	6
2.1. The direct and indirect band gap of optoelectronic materials.....	6
2.2. The polar, semi-polar and non-polar plane of the wurtzite structure.....	6
2.3. The substrates and buffer layer of hetero-epilayer GaN.....	7
2.3.1. Substrates.....	9
2.3.2. Buffer layer.....	12
2.4. The methods of fabricating single crystal thin films.....	13
2.4.1. Chemical vapor deposition (CVD).....	14
2.4.2. Metal-organic chemical-vapor deposition (MOCVD).....	15
2.5. Basic properties of the hexagonal wurtzite structure.....	15
2.5.1. Group theory of hexagonal systems.....	15
2.5.2. Characters of dislocations in the wurtzite structure.....	17

2.6.	Introduction of nanoindentation testing	17
2.6.1.	Mechanical properties	17
2.6.2.	Deformation mechanisms	20
2.7.	Introduction of microcompression testing	23
2.7.1.	Micropillar preparation	23
2.7.2.	Force loading and measurement	25
2.7.3.	Parameters of microcompression tests	26
2.7.4.	Microscale characterization of mechanical properties.....	28
2.8.	Thermal treatment of ion implanted semiconductors	30
2.8.1.	Defects and ion implantation	31
2.8.2.	Defects recovery	33
2.9.	Luminescence properties of semiconductors	35
2.9.1.	Raman spectrum.....	36
2.9.2.	Luminescence spectrum.....	38
Chapter 3. Experimental procedures		41
3.1.	Sample preparation	41
3.2.	Nanoindentation testing	42
3.3.	Microcompression testing.....	42
3.3.1.	Microcompression sample fabrication using FIB	43
3.3.2.	Thermal treatment	43
3.3.3.	Microcompression test using the nanoindentation system.....	44
3.3.4.	TEM sample fabrication using FIB.....	44
3.4.	Property measurement and analyses	45
3.4.1.	X-Ray diffraction analyses.....	45
3.4.2.	Scanning electron microscopy (SEM) analysis	46
3.4.3.	Transmission electronic microscopy (TEM) analyses	46

3.4.4. Raman spectrometer analyses	47
3.4.5. Cathodoluminescence (CL) spectrum analyses	48
Chapter 4. Experimental results	49
4.1. Structure quality identifications	49
4.1.1. X-ray diffraction analyses	49
4.1.2. EBSD analyses	49
4.1.3. Theoretical values calculations	50
4.2. Nanoindentation testing	55
4.2.1. ZnO	55
4.2.2. GaN	58
4.3. Microcompression testing	58
4.3.1. ZnO	58
4.3.2. GaN	60
4.3.3. Raman spectrometer analyses	61
4.4. SEM observations	62
4.5. XTEM analyses	63
4.6. Cathodoluminescence analysis	64
Chapter 5. Discussion	67
4.7. Low dimensional stress comparison	67
4.7.1. Theoretical and experimental results	67
4.7.2. Nanoindentation testing	68
4.7.3. Microcompression testing	69
4.7.4. Low dimensional measurements	71
4.8. Deformation mechanisms	72
4.9. Thermal treatment effects	73
4.10. Polarity effects	74

4.11. Hexagonal and cubic structure influence	74
4.11.1.Elasticity	75
4.11.2.Deformation mechanisms	76
4.11.3.Deformation energy analysis	78
Chapter 6. Conclusions	80
Chapter 7. Prospective and future work.....	84
References.....	85
Tables	101
Figures	121

List of tables

Table 1	Fundamental properties of III-V group semiconductors [11].	93
Table 2	The mechanical properties of polycrystalline ZnO, single crystallize ZnO wafer, thin films, nanowires, nanobelts measured by different testing techniques [59, 94, 100].	94
Table 3	The plane abbreviation and polarity of two semiconductors which used in this thesis.	95
Table 4	Comparison of the relevant III-V nitride material properties with perspective substrate materials [11, 29, 30].	96
Table 5	Structure, lattice constant, space group and density of five different LAO phases [89, 105].	97
Table 6	Lattice mismatch and thermal expansion coefficient between (200) γ -LAO and GaN [90, 106].	98
Table 7	Lattice parameters of a number of the prospective substrate materials for ZnO [16].	99
Table 8	The elastic constants list of ZnO [18].	100
Table 9	Hardness and Young's modulus of GaN from different kinds of indentation methods [20, 91].	101
Table 10	List of main luminescence lines and bands in GaN [72].	102
Table 11	Valance and ionic radii of candidate dopant atoms [30].	103
Table 12	Migration barriers for native defects in Wurtzite GaN [74].	104
Table 13	Comparison of the theoretical and experimental mechanical properties of ZnO.	105
Table 14	The elastic constants and estimated mechanical properties of GaN [108].	

.....	106
Table 15 Comparison of the theoretical and experimental mechanical properties of GaN.	107
Table 16 The Raman spectra peak position and FWHM of bulk ZnO.	108
Table 17 The fundamental optical modes of the Wurtzite crystal (frequency expressed in cm^{-1}) [82].	109
Table 18 The measurement of Raman E_2 peak position and FWHM of GaN films and micropillars [54].	110
Table 19 Young's modulus measured from different kinds of indentation methods [56, 60, 70].	111
Table 20 Comparison of the crystal structure, mechanical data, and dominant deformation modes in the four optoelectronic materials [54, 60, 110].	112

List of figures

Figure 1	Three structure types of II-IV group binary compound (a) Rocksalt (b) Zincblende (c) Wurtzite [16].	113
Figure 2	The corresponding band gap range of luminescence semiconductors [13, 18].	114
Figure 3	Schematic diagrams showing the transitions across (a) a direct band gap and (b) an indirect band gap [107].	115
Figure 4	Direct band gap of GaN [11].	116
Figure 5	Direct band gap of ZnO [16].	117
Figure 6	Wurtzite hexagonal structure.	118
Figure 7	Wurtzite structure along [0001] c-axis.	119
Figure 8	A sketch of induce the intrinsic electric field [37, 51].	120
Figure 9	Non-polarity directions of GaN.	121
Figure 10	The figures show the reflectance spectra of unstrained A-plane GaN with the light polarized parallel (a) and perpendicular (b) to the c-axis. Clearly, the A exciton is visible only in (b), demonstrating a polarization anisotropy of 100% in this spectral range [22-25].	122
Figure 11	Growth of hetero-epilayer (a) pseudomorphic (b) strain free layer [92, 108].	123
Figure 12	Schematic diagram showing the epitaxial relationships of c-plane ZnO grown on sapphire (0001) [16].	124
Figure 13	Chemical vapor deposition (CVD) process [93, 109].	125
Figure 14	Low temperature, pressure and high gas velocity conditions of CVD [93, 109].	126

Figure 15	High temperature, pressure and low gas velocity conditions of CVD [93, 109].	127
Figure 16	Two-Flow MOCVD (TF-MOCVD) [48].	128
Figure 17	Projection of wurzite hexagonal structure [55].	129
Figure 18	The sketch of the nanoindentation testing [52].	130
Figure 19	The sketch of the nanoindentation load-displacement (p-h) curve [52].	131
Figure 20	Contour plot of the CRSS of Berkovich tip at $(01\bar{1}2)$ slip plane (a) and $(2\bar{1}\bar{1}3)$ slip plane (b), where distances r and z are normalized by the contact radius a [53].	132
Figure 21	The bright field cross section TEM image of spherical indent in ZnO at maximum load of 50 mN, the black arrow point out the basal plane (0001) and the red arrow point out the pyramidal plane $\{1011\}$ [57].	133
Figure 22	The sketch of slip directions. Red lines represent the first slip system. Blue lines represent the secondary slip system [53].	134
Figure 23	Typical nanoindentation load–displacement data for annealed (100) Ni obtained using a 0.58 μm radius spherical indenter. Elastic contact (Hertzian) solutions are shown for the data below the pop-in loads [69].	135
Figure 24	The sketch of resolve shear stress.	136
Figure 25	Annular milling patterns have been used to mill a roughly defined micropillar sample of Ni single crystal [48, 62].	137
Figure 26	The microcompression samples were fabricated into (A) a Ni_3Al alloy and (B) Ni-based superalloy by using lathe milling program. The diameter of microcompression samples are 43 μm and 2.3 μm , respectively [48, 62].	138
Figure 27	SEM micrographs of the flat-punch tip: (a) top view and (b) side view and	

	(c) projected area of the punch tip.	139
Figure 28	Schematic of the microcompression test setup [64].	140
Figure 29	Schematic of a cylindrical pillar and its base [64].	141
Figure 30	Effect of fillet radius/pillar radius ratio on numerical simulation output. The inset shows an enlargement of the circled region to facilitate comparison [21].	142
Figure 31	(a) Deformed configuration of a circular cylindrical pillar with an aspect ratio $\alpha = 5$ at a strain of 0.1. (b) Deformed configuration of the pillar at the same strain of 0.1, but now considering friction. (c) Input and output stress-strain curves for a pillar with an aspect ratios $\alpha=2\sim 5$, both with friction and without friction (NF) [21].	143
Figure 32	Effect of taper on numerical simulation output [21].	144
Figure 33	Effect of misalignment of the system on the error in elastic modulus [21].	145
Figure 34	(a) The microcompressive engineering stress-strain curve of the $\text{Ni}_{76}\text{Al}_{24}$ alloy with 2 μm diameter. (b) SEM micrograph of a micropillar after microcompression test. Strain bursts are indicated by arrows in figure (a), and appearance of slip lines are also observed on the micropillar surface, as also indicated by arrows [67].	146
Figure 35	Typical load–penetration curve for a maximum load of 250 mN showing a pop-in event. Inset: Load–penetration curve for a maximum load of 50 mN showing multiple pop-in events at 28 and 34 mN [57].	147
Figure 36	Room-temperature monochromatic CL images of spherical indents in GaN. The maximum loads and horizontal field widths are (a) 25 mN and 15 mm, (b) 50 mN and 15 mm, and (c) 200 mN and 30 mm. CL imaging conditions: electron beam energy 520 keV, CL wavelength =366 nm, and	

	CL bandpass 52.5 nm [57].	148
Figure 37	The threading dislocation density decreases with increasing thickness for thin film GaN/sapphire [80, 96].	149
Figure 38	Formation energies as a function of Fermi level for native point defects in GaN [74].	150
Figure 39	Transition levels and formation energy of native defects in GaN [74]. ..	151
Figure 40	Experimental set up of a micro-Raman spectrometer [82].	152
Figure 41	The diagram of anti-Stokes scattering [82].	153
Figure 42	The Raman spectra of back scattering, near forward scattering and right angle scattering modes [82].	154
Figure 43	The backscattering diagram of wurtzite micro-Raman spectrum. (a) input-output z axis [0001], (b, c and d) input-output a-axis $[10\bar{1}0]$ [82].	155
Figure 44	The right angle scattering diagram of wurtzite micro-Raman spectrum [82].	156
Figure 45	The E_1 phonon propagation in the (0001) plane. The transverse phonon is illustrated by the solid-line polarization vector, and the dashed line corresponds to the $(11\bar{2}0)$ polarization component of Raman spectrum. The k2 and k3 lines represent the quasi QA peak between the $E_{1(TO)}$ and $A_{1(TO)}$ peaks.	157
Figure 46	Deconvolution of c-plane GaN XRD rocking curve (0002) Peaks. [80, 96].	158
Figure 47	Schematic illustration of TEM sample procedure using FIB [97].	159
Figure 48	The XRD pattern shows GaN has a sharp peak located at $2\theta = 34.62^\circ$..	160
Figure 49	The XRD pattern of GaN estimate by CaRine software.	161
Figure 50	The XRD Rocking curve pattern shows a broad peak ranging from 16.45° to	

	17° with full width of middle height (FWMH) = 0.341°	162
Figure 51	The EBSD patterns and SEM SEI image of c-plane ZnO.	163
Figure 52	The EBSD pattern and SEM SEI image of c-plane GaN.....	164
Figure 53	Showing the load-displacement and modulus-depth curves of c-plane ZnO at CSM constant displacement rate mode.	165
Figure 54	Representative nanoindentation load-displacement curves of the as-grown, annealed wafer and the curve predicted by the Hertzain contact theory.	166
Figure 55	Representative nanoindentation load-displacement curves of the c-plane, a-plane, m-plane ZnO wafer and the curve predicted by the Hertzain contact theory.	167
Figure 56	Showing the data of c-plane GaN CSM mode depth 1000 nm nanoindentation testing.	168
Figure 57	Showing the first pop-in data of CSM mode depth 500 nm (~10% to total thickness) indentation testing.....	169
Figure 58	Representative as-grown preset 300 nm pillar and annealed preset 300 nm pillar stress-strain curves of microcompression testing.	170
Figure 59	Representative load-displacement curves for microcompression of c-plane GaN micropillars.....	171
Figure 60	Representative load-displacement curves for microcompression of a-plane ZnO micropillars.....	172
Figure 61	Representative load-displacement curves for microcompression of m-plane ZnO micropillars.....	173
Figure 62	The recorded data and Gaussian fitting Raman spectra of film ZnO.....	174
Figure 63	The Raman spectra of ZnO after Ufine, middle and rough beam FIB Ga implanted conditions.....	175

Figure 64	The recorded data and Gaussian fitting Raman spectra of as-grown ZnO.	176
Figure 65	The recorded data and Gaussian fitting Raman spectra of preset 40 nm ZnO pillar.....	177
Figure 66	The recorded data and Gaussian fitting Raman spectra of preset 300 nm ZnO.....	178
Figure 67	The recorded Raman spectra of GaN film, as-milled pillar, preset 100 nm pillar and preset 200 nm pillar.	179
Figure 68	Showing the SEM image of (a) as-grown c-ZnO pillar and (b) annealed c-ZnO pillar after microcompression.....	180
Figure 69	Showing the SEM image of m-ZnO pillar after microcompression.	181
Figure 70	Showing the SEM image of a-ZnO pillar after microcompression.....	182
Figure 71	SEM images of (a) mark, (b) carbon protection layer and (c) side view of c-plane ZnO HR-XTEM sample.....	183
Figure 72	Representative c-plane GaN (a) 1 μm as-FIB-milled pillar SEM images and (b) first strain burst micropillar SEM image.....	184
Figure 73	Showing the SEM image of (a) r-GaN thin film morphology, (b) cross section and (c) as-milled micropillar.....	185
Figure 74	(a) XTEM bright filed image of the ZnO micropillar compressed to a preset displacement of 300 nm, and (b) the associated selected area diffraction pattern, with an indexed zone axis of $[10\bar{1}0]$	186
Figure 75	TEM characterization of the GaN micropillar compressed to a preset displacement of 200 nm: (a) bright field image from the longitudinal section, (b) selected area diffraction pattern for the upper region, and (c) selected area diffraction pattern for the lower region of the compressed pillar, with an indexed zone axis of $[10\bar{1}0]$	187

Figure 76	XTEM characterization of the 200 mN nanoindentation mark of the c-plane GaN thin film, with an indexed zone axis of $[10\bar{1}0]$.	
Figure 77	The recorded cathodoluminescence spectrum of GaN from NSYSU.....	189
Figure 78	The recorded cathodoluminescence spectrum of bulk ZnO from ISU....	190
Figure 79	The a-plane ZnO pillar CL spectra of just focus and over focus plane...	191
Figure 80	Representative c-plane ZnO CL spectra, and corresponding SEM SEI image and CL image of 383 nm.....	191
Figure 81	The m-plane ZnO CL spectra of wafer, preset 50, 300 and 400 nm pillars.	201
Figure 82	Representative c-plane ZnO X-CL spectra, and corresponding SEM SEI image.....	194
Figure 83	The center dark field (0001) image of c-plane ZnO micropillar, with an indexed zone axis of $[10\bar{1}0]$.	

Abstract

Wide band gap semiconductors ZnO/GaN attracted a great deal of interests for decade, due to their wide direct band, high electron binding energy, excellent chemical and thermal stability, good heat conductivity and capability, high electron mobility and transparent properties at room temperature. They have many potential applications such as laser, biosensor, piezoelectric power generator, nano-electromechanical systems and flat panel field emission displays. However, unexpected contact loading during processing or packaging may induce residual stresses and/or an increase in defect concentration in ZnO/GaN wafer or thin film, causing possible degenerated reliability and efficient operation of the piezoelectric and photonic device. To ensure and improve the performance of devices based on ZnO/GaN, a better understanding of the mechanical/optoelectronic response under different processing and loading conditions and even the measuring methods are necessary.

In this thesis, our aim is to reveal a comprehensive investigation of the mechanical responses on polar/non-polar GaN/ZnO single crystal under low dimensional stress. We try to provide the fundamental theoretical and experimental studies for further application and researches, such as tension testing, residual stress, low temperature cathodoluminescence and Raman spectroscopy analysis.

In this study, the theoretical Young's modulus and Poisson ratio of ZnO/GaN are extracted from elastic constants for comparison and further estimation. The nano-scaled mechanical properties, such as Young's modulus, hardness and yield

stress, are identified by using the nanoindentation system. The experimental values were fitting by the Hertzian contact theory. The results are in good agreement with the theoretical predictions. No significant strain rate influence is observed over the strain rate from $1 \times 10^{-2} \text{ s}^{-1}$ to $1 \times 10^{-4} \text{ s}^{-1}$. The comparisons of mechanical properties between the polar and non-polar planes of ZnO are firstly examined. The results reveal that the non-polar planes are softer than the polar plane. Both a-plane and m-plane ZnO have lower hardness and yield stress than c-plane ZnO. The microstructure and deformation mechanism are analyzed by using X-TEM and SEM. No pop-out or slope changing was found in their load-displacement curves, suggesting no phase transformation, twinning or crack domain deformation occurred under microcompression and nanoindentation testing. Taking all considerations for the higher resulting Schmid factor and lower Burgers' vector, the most possible slip system for c-plane hexagonal structures is the pyramidal plane. The a-plane has shorter burger's vector on the slip plane which leads the lower yield stress than c-plane.

To erase the effect of FIB induced Ga ion implantation, the c-plane ZnO was annealed at 900°C for 1 hour. We found that the yield stress under microcompression decreases and the intensity of the cathodoluminescence spectrum increases after the annealing process. This result indicates that the thermal treatment is a good way to refine the crystal quality and decrease the defects density. The E_2 peak of Raman spectrometer exhibits high residual compression stress constrain in the c-plane GaN thin film. Due to the high surface/volume ratio of pillar, nil residual stress remains in the GaN pillar after the FIB milling process. Even after the yield point, nil residual stress remains in the c-GaN pillar. Results indicate that the one dimensional geography is a good way to erase residual stress.

中文摘要

近數十年來，寬能隙氧化鋅與氮化鎵半導體引起科學界廣泛與熱烈的興趣。主因於其優異的室溫物理性質，諸如：直接能隙、高電子束縛能、良好的化學與熱穩定性、優異的熱傳導、高電子移動能力與其光學透明性。他們被廣泛的利用於雷射、生物偵測器、壓力發電機、奈米機電系統，並被視為取代現有平面顯示器核心元件之潛力材料。然而在製造元件或封裝過程中，外在的接觸應力會造成材料內部的殘留應力或增加材料缺陷濃度，造成光電或壓電性元件其效能降低。為了確保以及改善元件品質，更深入的瞭解氧化鋅與氮化鎵，在施加應力的情況下其光電性質與機械性質的反應是必需的。

本研究主要是先利用彈性常數去估算理論楊氏模數與波松比，再將理論波松比帶入實驗結果，將實驗楊氏模數與理論值做確認，確保波松比在更進一步計算中準確。此外，利用奈米壓痕實驗探討奈米尺度下的楊氏模數與硬度，並與微奈米尺度的一維壓應力實驗結果做比較。再將實驗結果帶入 Hertzian 彈性模型，得出破壞降伏強度與臨界剪切應力。實驗結果與理論值吻合，在奈米與微奈米尺度下均無應變速率對機械性質影響，非極性面與極性面比較結果發現，非極性面有較低的硬度。利用掃瞄式與穿透式電子顯微鏡做塑性變形的圍觀組織分析結果得知，在二維奈米壓痕與一維壓應力測試中都沒有發現相變化、雙晶與裂縫。差排滑移為主要變形機制，變形系統為錐面。在熱處理、光電性質與幾何形狀部分相關研究，我們發現但氧化鋅在常壓 900°C 下加熱一小時，可有效提升晶體表面品質，減少因離子殖入造成非晶層的厚度，而陰極射線光譜藍光帶之強度也增加了 1.5 倍。拉曼光譜分析發現長在藍寶石基版的氮化鎵薄膜中含有的殘留應力，可以經由高表面/體積比的幾何形狀得到釋放。釋放殘留應力後，由高斯分佈分析拉曼光譜 E_2 波峰發現有紅位移的現象。

本論文試圖對六方對稱之氧系與氮系發光半導體材料提出廣泛的研究，對於日後更深入的探討理論機械性質、變形機制、缺陷分析、殘留應力、極性與非極性、熱處理、發光性質、微觀結構、幾何形狀與尺寸效應，提出理論與實驗基礎。最後，我們比較了四種常見半導體材料的機械性質與破壞機制，並對於日後的實驗發展提出粗略的方向。

Chapter 1. Introduction

Over the past few decades, scientific researchers raised a great deal of interests in the wide (>3 eV) band gap semiconductors, such as GaN and ZnO. Because of their high exciton binding energy, high thermal conductivity, high chemical stability, they have been widely used in electrically pumped ultraviolet–blue light-emitting diodes (LED), lasers, piezoelectric generator and photon detectors [1, 2]. At the end of 80's, Akasaki et al. [3-6] and Nakamura et al. [7, 8] successfully grew high quality GaN on the (0001) sapphire substrate, and hence, produced high efficiency blue light LED. It is a landmark of lighting evolution and gives rise to a great series of researches on extensive issues, e.g. substrate, size effect, polarity, mechanical properties, or optoelectronic properties.

Moreover, one dimension (tip-like or needle-like) semiconductors have attracted considerable attention in various applications, such as biosensor, laser and field emitted displays (FED). It can replace the carbon nanotubes (CNTs) and become one of the potential materials to make the key devices of field emitted displays. It is because ZnO has good chemical stability, mechanical stability and work functions electron affinities (4.5 eV) [9]. The fundamental properties of GaN, ZnO, and other wide band gap semiconductors are briefly introduced in the following sections.

1.1. GaN

Gallium nitride is a binary III/V semiconductor with a 3.3 eV direct band gap. The

compound is very hard and stiff (hardness $H \sim 15$ GPa and Young's modulus $E \sim 272$ GPa). There are two structure types, namely, the most common hexagonal wurtzite structure (space group $C_{6v}/P6_3mc$) and cubic zincblende structure, depending on substrate symmetry and growing conditions [10]. The lattice constant c/a ratio of hexagonal GaN is ~ 1.626 which is close to the ideal hexagonal closed packing (~ 1.633), and the Poisson ratio is about 0.35 (along the c -axis). Its high thermal stability (melting point $T_m \sim 2500^\circ\text{C}$), high electron mobility ($440 \text{ cm}^2/\text{V}\cdot\text{sec}$), high exciton binding energy (25 meV), high thermal conductivity ($1.3 \text{ W}/\text{cm}\cdot\text{K}$ at room temperature) and good chemical stability make it possible to be applied in high power and frequency optoelectronic devices or solar cell array in satellites. Table 1 [11] shows the rest properties of III-nitride group compounds.

1.2. ZnO

Zinc oxide is an inorganic II/VI group semiconductor with 3.4 eV direct band gap. Compared with GaN, ZnO has relatively soft mechanical properties ($H \sim 4.2$ GPa and $E \sim 140$ GPa). In comparison with GaN/sapphire, ZnO/sapphire has approximately equivalent X-ray-diffraction (XRD) and photoluminescence (PL) line width, and even lower dislocation densities [12]. ZnO has three phases. The most stable structure is hexagonal wurtzite which is usually observed at ambient condition. The cubic zincblende structure can be grown by using cubic substrate. The cubic rocksalt structure (NaCl type) is high pressure phase (pressure greater than 10 GPa). The lattice parameter c/a ratio is about ~ 1.633 ($a=3.252 \text{ \AA}$ and $c= 5.313 \text{ \AA}$) and the Poisson ratio is about 0.34 (along the c -axis). ZnO has high electron binding energy ~ 60 meV (which means electrons need higher energy to escape from molecule orbits onto its surface). Its high ionicity ~ 0.616 (cp. GaN ~ 0.5) causes the best piezoelectricity in III/V and II/VI

groups. Moreover, the good chemical and thermal stability, heat conductivity, high electron mobility and transparent properties make ZnO possible to be applied in non-toxicity transparent thin film, transparent thin film transistor, piezoelectric power generator (~7% efficiency) [16] and flat panel field emission displays.

1.3. Other wide band gap semiconductors

The bandgap of GaN can be changed by doping other group III nitrides, such as InN or AlN. The adapted bandgap can fully cover the range from infrared to ultra-violet light wavelength. The single crystal indium nitride InN exhibits a narrow direct band gap (~0.7 eV) which is slight function of temperature. InN has the same hexagonal wurtzite structure with a lattice parameter c/a ratio ~1.623 in ambient condition. It is usually mixed with GaN as a ternary group III nitride $\text{In}_x\text{Ga}_{1-x}\text{N}$ (where x is between 0.02~0.3) to apply in blue/green optoelectronic devices. But when the In/Ga ratio >0.4 , non-radiation defects and phase separation dominated which degenerated the efficiency of high frequency light emitting diodes [13]. The single crystal aluminum nitride AlN exhibits the largest direct band gap (6.2 eV at room temperature), high melting point ($T_m \sim 3237$ K), relatively high thermal conductivity (285 W/m-K), electron mobility (~300 $\text{cm}^2/\text{V}\cdot\text{sec}$) in semiconductor ceramics [14]. It has loose hexagonal wurtzite structure (c/a ratio ~1.600). It can be used to fabricate UV LED or high electron mobility transistor (HEMT) [15].

For ZnO, group II-IV semiconductor magnesium oxide and cadmium oxide have three kinds of structures, which are hexagonal wurtzite, cubic rocksalt and zinblende, as shown in Figure 1 [16]. By composing these three oxides, the wide band gap can be adopted from 161 nm (7.7 eV) to 539 nm (2.3 eV) wavelength [17]. Figure 2 shows

various band gaps of the II-IV groups, III-V groups and other semiconductors [13, 18].

1.4. Motivations

The unexpected contact loading during processing or packaging might induce residual stress and/or defect concentration of the wide bandgap semiconductors, causing possible degradation of the device performance. Thus, to improve the successful fabrication of devices, based on epitaxial thin films and wafer, a better understanding of the mechanical characteristics is necessary and meaningful.

So far, there have been some reports addressing the macroscaled or macroscaled mechanical responses of the bulk or thin film crystalline by using indentation (Table 2), but there is appreciable disparity in the measured values among various samples (e.g., shape and size), in particular single crystals. Microcompression testing can provide a simple uniform stress to study the mechanical properties and the corresponding luminescence responses for the single crystal wide bandgap semiconductor which is hard to be fabricated into bulk scale.

In this thesis, our aim is to reveal a comprehensive investigation of the mechanical responses on polar/non-polar GaN and ZnO single crystal under low dimensional stress. In addition, we try to investigate the luminescence responses of the defects, residual stress, thermal treatment by using Raman and cathodoluminescence spectroscopy, particularly in the sub-microscale and nanoscale region [21].

Chapter 2. Background and literature review

2.1. The direct and indirect band gap of optoelectronic materials

Wide band gap semiconductors have been used in order to produce high power lightening devices. The band gap can be simply distinguished as direct and indirect band gap. Figure 3 shows the schematic diagrams of direct and indirect band gap. For direct band gap materials, such as III-V series semiconductor (GaN/AlN/InN in Figure 4 [11]) or II-IV series semiconductors (ZnO/MgO/CdO in Figure 5 [16]), the electron-hole pairs can be produced by giving electric or solar energy. The electron-hole pairs are then recombined in a very short time and released most energy by photon. Only energy conservation should be considered in the recombination process of direct band gap. In comparison, the electron-hole pairs of indirect band gap material, such as GaAs, have to obey both energy and momentum conservation during the recombination process. Energy was released into photon and phonon which lead the degeneration of the lightening efficiency. In this thesis, we focus on the direct band gap material (GaN and ZnO) because of their better transition efficiency than the indirect band gap materials.

2.2. The polar, semi-polar and non-polar plane of the wurtzite structure

Single crystal wurtzite structure (Figure 6) has anisotropic properties in different directions. The c-plane has polarity in [0001] (c-axis) direction. The cations and anions stock at different layers of the (0001) c-plane. Although the whole structure

remains electrical neutrality, there is a little distance between the cation and anion atoms along the *c*-axis (Figure 7). The small deviation from ideal position causes an electrical dipole momentum and induces the intrinsic electric field along the *c*-axis (Figure 8). The *c*-plane is regarded as a polar plane and for those planes which include partial quantity of *c*-plane, such as, *r*-plane ($1\bar{1}02$), is regard as the semi-polar plane. Both of them would cause the decrease of the luminescence efficiency of optoelectronic devices. On the other hand, the non-polar planes (Figure 9), such as the *m*-plane ($10\bar{1}0$) and the *a*-plane ($2\bar{1}\bar{1}0$), have no intrinsic electric field along the $\langle 10\bar{1}0 \rangle$ and $\langle 2\bar{1}\bar{1}0 \rangle$ directions. Figure 10 reveals that light polarized parallel to the non-polar plane can stimulate higher energy excitons than light polarized perpendicular to the polar plane, thus enable to fabricate higher energy ultraviolet light-emitting devices [22-25]. In this thesis we focus on the anisotropic material properties on polar, semi-polar and especially non-polar plane. Table 3 lists the plane abbreviation and polarity of two semiconductors used in this thesis.

2.3. The substrates and buffer layer of hetero-epilayer GaN

Because it is difficult and expensive to grow some macro-scaled high quality single crystal semiconductor wafers as homo-epitaxy substrates, to find a suitable substrate material becomes an important issue, especially for producing thin film material. The threading dislocations, residual stress and other defects from hetero-epitaxy substrate could greatly change the performance of the luminescence device.

The affection of threading dislocation density on thin film can be confirmed by the nanoindentation system and cathodoluminescence spectroscopy (CL). The pop-in

event in load-displacement curve of nanoindentation system is related to the threading dislocation density. The load of the critical pop-in decreases with increasing pre-existing threading dislocation density [26]. The CL spectrum reveals the non-radiation zone at the threading dislocations and indentation points. Which means the high threading dislocation density not only creates non-radiation regions at the surface but also makes the non-radiated dislocations easier to be increased under the pressure.

To ensure the high crystal quality, three important coefficients should be considered when choosing a suitable hetero-epitaxy substrate:

1. lattice mismatch,
2. buffer layer,
3. thermal expansion

The formula of lattice mismatch strain can be represented by

$$f = \frac{a_s - a_e}{a_e}, \quad (2-1)$$

where a_s is lattice constant of substrate, a_e is lattice constant of epitaxy thin film, and positive f is tension strain and negative f is compression strain. If $f < 1\%$, the thin film structure will be strongly influenced by the substrate. The pseudomorphic layer will grow on the substrate (Figure 11 [92, 108]). If $f > 1\%$, the lattice mismatch will create a residual stress field. As the thickness increases, more energy would be stored in the sample. When the thickness grew over a critical thickness, dislocations are then

created to release the strain energy. The large lattice mismatch leads the higher build-in threading dislocation density [27, 28].

The other consideration is the difference of the thermal expansion. The epilayers are often cracked after post-growth cooling due to the large thermal strain difference between substrate and thin film. The comparison of the relevant III-V and II-IV group material properties with perspective substrate materials is shown in Table 4 [11, 29, 30].

To reduce the lattice mismatch and thermal expansion difference, some buffer layers are grown not only on the hetero-epitaxy substrates but on the homo-epitaxy substrate as well. The threading dislocations density and residual stress can be reduced by growing hetero-buffer layers, defect free wires or low temperature buffer layers between the substrate and the targeting thin film.

Thus, substrates play an important role in producing high quality semiconductor wafer and thin film. Both mismatch and thermal strain will strongly affect the dislocation density. The following sections list some brief considerations of common substrates as well as buffer layer in the wide band gap semiconductor growing process.

2.3.1. Substrates

Silicon has been widely researched in various fields by silicon industry for decades. Its relatively mature procedure and adaptable semiconductor properties, such as larger size, cheaper cost, good thermal conductivity and electrical conductivity,

make it become one of the main substrates to produce single crystal GaN. However, the mismatch between Si and GaN is 16.9% (c-GaN on (111)_{Si}) [22, 31]. To reduce misfit dislocations, AlN (hexagonal structures) epitaxy thin film is usually grown between (Si-AlN-GaN) as a buffer layer. The cubic (111)_{Si} plane is used to be the growing plane. The direction and plane between GaN, AlN and Si are shown as following [32, 33]:

$$[11\bar{2}0]_{\text{GaN}} // [11\bar{2}0]_{\text{AlN}} // [\bar{1}10]_{\text{Si}}, (0001)_{\text{GaN}} // (0001)_{\text{AlN}} // (111)_{\text{Si}}. \quad (2-2)$$

The other popular substrate for growing is sapphire (Al₂O₃). Single-crystal films have been grown on sapphire with a high degree of surface flatness, which is essential for device fabrication. It is another common material which is chosen to be the substrate of GaN thin film in this study. The benefit of choosing sapphire to be the substrate of growing process is because it has relatively small lattice mismatch than single crystal cubic silicon. The c-plane GaN thin film can grow on (0001)_{Sapphire} and the a-plane GaN epilayer can grow on (1 $\bar{1}$ 00)_{Sapphire}. The lattice mismatch between a-axis sapphire and c-axis GaN is 13.6% [34] and the difference of thermal expansion coefficient is 34% [35]. The lattice mismatch and thermal expansion difference will form a compression stress field in the film during process. For ZnO grown on sapphire, films usually display large mismatch and high residual strain, it is most likely due to defect-induced native centers carrier concentrations (in the 10¹⁷ cm⁻³ range), and low mobility (less than 100 cm² V⁻¹ s⁻¹ at room temperature) as compared to an electron concentration of 10¹⁵ cm⁻³ and Hall mobility of 200 cm² V⁻¹ s⁻¹ typical for bulk single crystals. The epitaxial relationship of

$$[0001]_{\text{ZnO}} // [0001]_{\text{sapphire}}, [10\bar{1}0]_{\text{ZnO}} // [11\bar{2}0]_{\text{sapphire}} \quad [16]. \quad (2-3)$$

A low temperature AlN buffer layer can reduce the threading dislocation density and residual stress. Although the sapphire substrate has good chemical and thermal stability, the good stability brings out another tough issue of processing thin film into a free standing sample.

LiAlO₂ (LAO) is another potential substrate material of producing free standing thin film. Due to its various advantages, such as lower lattice mismatch and thermal expansion mismatch than silicon and sapphire. Furthermore, LAO can be easily cleaved off from substrate by thermal decomposition. It is easier to produce the free standing sample. LAO was firstly compounded by Weyberg in 1906. Table 5 [89, 105] lists the structure, lattice constant, space group and density of five different phases of LAO. In particular, the (200) γ -LAO has been used as a substrate of non-polar GaN because of its lowest misfit ratio (<2% for a-plane). Table 6 [90, 106] lists the misfit between LAO, c-plane and a-plane GaN. Because of the small misfit ratio, there is of no need to grow a buffer layer between the substrate and thin film which can simplify the process. Nevertheless, there is still some problem to be solved out. The difference of thermal expansion coefficient between LAO and GaN is still large (55% along [100] and 63% along [001]). It will induce high threading dislocation density, cracks and even stripping during the cooling process.

For ZnO, homoepitaxy with its perfect lattice matching in-plane and out-of-plane has the potential for providing no strain induced by thermal-expansion mismatch, absence of highly defective substrate-layer interface, lower overall defect density, easy control over the material polarity by using Zn-face or O-face (0001) substrate, and simple device design ZnO substrates can be made very conductive. In addition to homoepitaxy, ZnO single-crystal substrates could also be useful for heteroepitaxy of

GaN-based active layers. The stacking order of ZnO is the same as that of GaN, with a lattice mismatch of only 1.8% [16]. Due to the complexity of the growing process, it should be mentioned that availability of high-quality ZnO substrate does not automatically pave the way for high-quality epitaxial layers.

Although high-quality ZnO substrates are available, making homo-epitaxy possible, most of the growth still has been done on sapphire (Figure 12 [16]). Despite its poor structural and thermal match to ZnO, it still has advantages such as low cost and availability as large-area wafers and its wide energy-band gap. Hetero-epitaxial ZnO layers have been grown on several other substrates, such as CaF₂ [36], Si [37], GaAs [38, 39], and ScAlMgO [40] as well as on GaN/sapphire templates [41]. Table 7 [16] lists the lattice parameters of a number of prospective substrates. There is much work remains to be done to attain epitaxial layer matching the bulk in quality.

2.3.2. Buffer layer

The large differences of the lattice parameter and the thermal expansion would induce internal stress field during the cooling process. The residual stress field would cause high density threading dislocations or film cleavage to the single crystal film. To solve this problem, growing a buffer layer by different methods can highly improve the thin film quality.

Yoshida et al. found that growing an AlN buffer layer could substantially improve the quality of epitaxy GaN grown on the sapphire substrate [42]. The same research team has done a series of studies to find the role of AlN buffer layer. Firstly the AlN will deposit as an amorphous structure at low temperatures. The amorphous

layer can cover the surface and improve the substrate uniformly. The temperature then heated to the normal growth temperature, the AlN phase transformed into crystalline structure (which has only 2.4% lattice mismatch along a-axis, as listed in Table 1 [11]). It provided an excellent template for epitaxy [3-6]. The procedure of GaN growing on AlN buffer layers successfully improved 10 times of carrier concentration and mobility, two orders of intense detected by photoluminescence (PL) and one fourth narrower of the full height at middle width (FHMW) by X-Ray diffraction peak.

2.4. The methods of fabricating single crystal thin films

The GaN thin films and ZnO wafers can be grown on various substrates by following methods: molecular beam epitaxy (MBE) [43-46], halide vapor phase epitaxy (HVPE) [41, 47], chemical vapor deposition (CVD) and metal-organic chemical-vapor deposition (MOCVD) methods [41, 48].

The mechanism of growing single crystal semiconductor on hetero-epitaxy substrates in different geometric shape should consider the surface energy and molecular mobility. Take the free surface energy between substrate-film (γ_i), film (γ_f) and substrate (γ_s) into consideration. There are three different growing modes: the Frank-van der Merwe mode (thin film), the Volmer-Weber mode and the Stranski-Krastanov mode [106]. According to thermodynamics, if single crystal epi-layer thin film needs to be deposited on substrate without peeling off, the total surface energy of film and interface should be less than the free surface energy of substrate.

$$\Delta\gamma = \gamma_f + \gamma_i - \gamma_s < 0. \quad (2-4)$$

Using the Frank-van der Merwe mode to deposit a flat 2D thin film, substrate-film interface free surface energy can be neglected by small lattice mismatch, the free surface energy of film should be larger than the free surface energy of substrate (γ_f). Substrate would be easily wet if lattice mismatch $\cong 0$ and $\gamma_f < \gamma_s$ [49]. The following is the briefly introduction of the manufacturing procedures of epi-layer GaN thin film by CVD and MOCVD in laboratory.

2.4.1. Chemical vapor deposition (CVD)

The chemical vapor deposition process can be separated into five steps (Figure 13 [93, 109]):

1. Input highly volatile reactant (precursor) into reaction tube.
2. Reactant diffuses in by main gas flow, passes through boundary layer and reaches the surface of substrate.
3. Reactant is absorbed by surface.
4. Precursor reacts and becomes deposition.
5. Product (gas) desorbs, diffuses out and excludes by main gas flow.

The last step determines the deposition rate. Total gas flux, tube pressure and orientation, surface area, geometric direction of substrate could also affect the deposition rate. At low temperatures, pressure and high gas velocity conditions (Figure 14 [93, 109]), reactant can easily reach surface, but reaction will become slower, and dynamics dominate whole process due to the lack of kinetic energy. At high

temperatures and high pressures with low gas velocity, Figure 15 [93, 109] shows when the reaction rate increases, boundary layer becomes thicker and diffusion rate dominates the whole process.

2.4.2. Metal-organic chemical-vapor deposition (MOCVD)

At the end of 1980s, Nakamura of Nichia chemical company modified MOCVD as two-flow MOCVD (TF-MOCVD, Figure 16 [48]) and produced high quality GaN in Figure 17 [55], based on the reaction below:



Substrates should be heated to at least 800°C to deposit the high quality GaN. 1050°C was the right temperature to gain highest quality of GaN. Once the temperature was higher than 1100°C, GaN would crack due to the high vacancy density [50].

2.5. Basic properties of the hexagonal wurtzite structure

In this study, two wurtzite structure materials (GaN and ZnO) in four orientations (Table 3) are analyzed of their mechanical properties and the luminescence performance. For clarity of presentation, the following sections list the basic group theory, formulas of mechanical properties, deformation mechanism and defects.

2.5.1. Group theory of hexagonal systems

Both GaN and ZnO are hexagonal system, four indices direction [uvtw] and three

indices system [UVW] can be converted by the following relations:

$$\begin{aligned}
 h=u-t & \quad u=(2h-k)/3, \\
 k=v-t & \quad v=(2k-h)/3, \\
 l=w & \quad t=-(h+k)/3, \\
 & \quad w=l.
 \end{aligned}
 \tag{2-6}$$

Three indices direction system (UVW) can be converted to four indices system (uvtw) by adding $t = -(U+V)$. In the other side, simply take t term away from four indices system can convert back into three indices system. In addition, unlike the cubic system, not all the indices of direction [abc] is the normal vector of plane (abc). To get the normal directions of other planes, space directions should be converted into three indices. Then pick arbitrarily two vectors on the plane and cross them into one vector. The normal direction can be calculated by transforming back to four indices. The following contains the name of the main planes and their plane directions:

$$\begin{aligned}
 & \text{Basal plane, c-plane } \{0001\} \langle 0001 \rangle, \\
 & \text{m-plane } \{10\bar{1}0\} \langle 10\bar{1}0 \rangle, \\
 & \text{a-plane } \{11\bar{2}0\} \langle 11\bar{2}0 \rangle. \\
 & \text{Pyramidal plane } \{10\bar{1}1\} \langle 10\bar{1}1 \rangle, \\
 & \text{r-plane } \{1\bar{1}02\} \langle 1\bar{1}02 \rangle.
 \end{aligned}
 \tag{2-7}$$

Reciprocal unit vectors and real lattice unit vectors share the following relation:

$$b_1 = \frac{a_2 \times a_3}{a_1 \cdot a_2 \times a_3}, b_2 = \frac{a_3 \times a_1}{a_1 \cdot a_2 \times a_3}, b_3 = \frac{a_1 \times a_2}{a_1 \cdot a_2 \times a_3} . \quad (2-8)$$

Because the reciprocal lattice has the property of orthonormality, reciprocal direction [hkl] would always be normal to reciprocal plane (hkl). For reciprocal lattice, the length of reciprocal vector $|\vec{g}|$ ($|\vec{g}| = hb_1 + kb_2 + lb_3$) equal to $1/d_{hkl}$, where d is d spacing of periodicity lattice.

2.5.2. Characters of dislocations in the wurtzite structure

The Burgers vector of threading dislocations in a hexagonal structure could be found by Thompson tetrahedron. For basal planes {0001}, there are 6 edge dislocations which lied on the plane (Burgers vector $\frac{1}{3}\langle 11\bar{2}0 \rangle$) and two screw dislocations (Burgers vector $\langle 0001 \rangle$) which perpendicular to the plane. Combining edge and screw dislocations could get extra 12 sets of mixed dislocations (Burger vector $\frac{1}{3}\langle 11\bar{2}3 \rangle$). The partial dislocations could be classified as Shockley partial dislocation $\frac{1}{3}\langle 1\bar{1}00 \rangle$ (lied on the basal plane) and Frank partial dislocation $\frac{1}{3}\langle 0001 \rangle$ (perpendicular to the basal plane). Combining Shockley and Frank partial dislocations can gain another partial dislocation group $\frac{1}{6}\langle \bar{2}203 \rangle$ [37, 51] .

2.6. Introduction of nanoindentation testing

2.6.1. Mechanical properties

The basic mechanical properties, hardness (H) and Young's modulus (E) can be calculated by using the Oliver-Pharr model (Figure 18) [20, 52]. The formula of hardness is:

$$H = \frac{P_{\max}}{A_c}, \quad (2-9)$$

where P_{\max} is the maximum indentation load in load-displacement curve (Figure 19 [52]), A_c is the projected contact area which can be extend to a series:

$$A = F(h_c) = C_0 h_c^2 + C_1 h_c + C_2 h_c^{1/2} + C_3 h_c^{1/4} + C_4 h_c^{1/8} + C_5 h_c^{1/16}. \quad (2-10)$$

C_0 to C_5 can be obtained by testing a standard sample, in this case silica, and h_c is the contact depth. In the limit of $h_c \ll R$ (here R is the radius of indenter tip), the relationship can approximately reduce to

$$A = 2\pi R h_c = C_0 h_c^2 + C_1 h_c. \quad (2-11)$$

The tip radius R can then be extract from the projected contact area of the shallow depth [53]. The formula of reduced Young's modulus E_r is:

$$\frac{E_r}{1-\nu_s^2} = \frac{\sqrt{\pi}}{2} \frac{1}{\sqrt{A_c}}, \quad (2-12)$$

where ν_s is Poisson ratio of the sample. Considering the displacement from the tip, the Young's modulus of the sample can be extract by

$$\frac{1}{E_r} = \left(\frac{1-\nu_s^2}{E_s} \right) + \left(\frac{1-\nu_i^2}{E_i} \right) \quad (2-13)$$

The E_i and ν_i are the Young's modulus and Poisson's ratio of the diamond indenter. Our MTS nanoindentation system gives the measured value of diamond tip, the Young's modulus is $E_i = 1141$ GPa and the Poisson's ratio is $\nu_i = 0.07$. The Poisson ratio of sample act important role in both formula. For anisotropic material, the Poisson ratio ν_s of different direction can be derived by the elastic constant matrix C_{ij} . For Hexagonal wurtzite structure, the symmetry can simplify the matrix as following:

$$\begin{bmatrix} \sigma_1 \\ \sigma_2 \\ \sigma_3 \\ \sigma_4 \\ \sigma_5 \\ \sigma_6 \end{bmatrix} = \begin{bmatrix} C_{11} & C_{12} & C_{13} & 0 & 0 & 0 \\ C_{12} & C_{11} & C_{13} & 0 & 0 & 0 \\ C_{13} & C_{13} & C_{33} & 0 & 0 & 0 \\ 0 & 0 & 0 & C_{44} & 0 & 0 \\ 0 & 0 & 0 & 0 & C_{44} & 0 \\ 0 & 0 & 0 & 0 & 0 & C_{66} \end{bmatrix} \begin{bmatrix} \varepsilon_1 \\ \varepsilon_2 \\ \varepsilon_3 \\ \varepsilon_4 \\ \varepsilon_5 \\ \varepsilon_6 \end{bmatrix}, \quad (2-14)$$

where σ_1, σ_2 and σ_3 is the normal stress along a_1 -axis, a_2 -axis and c -axis, respectively. The elastic constants $C_{11}, C_{12}, C_{13}, C_{33}, C_{44}$, and C_{66} are listed in Table 8 [16]. The equation of stiffness (S) and damping (C) are

$$S = \left[\frac{1}{(P_{\max} / h(\omega)) \cos \phi - (K_s - m\omega^2)} - K_f^{-1} \right]^{-1}, \quad (2-15)$$

$$\omega C = \frac{P_{\max}}{h(\omega)} \sin \Phi ,$$

where Φ is the phase angle between P_{\max} and $h(\omega)$, m is the mass of the indentation column, K_s is the is spring constant in the vertical direction, K_f is frame stiffness, ω is angular speed which equals $2\pi f$, f is the driven frequency of the ac signal of 45 Hz for CSM mode [54]. Table 9 summarizes the mechanical properties by using different kinds of indentation methods [20]. Because m , K_s and K_f are all constant values for the specified indentation system, there are deviation of E and H between different indentation tips. E and H values extracted by Berkovich tip are larger than other shape of tips.

2.6.2. Deformation mechanisms

So far, there is no evidence of twining or phase transformation induced during deformation in GaN and ZnO. It is believed the dislocation is the dominated deformed mechanism. The preferred slip plane would be changed as c/a ratio is changed. According to theoretical lattice strength:

$$\tau_{\max} = \frac{Gb}{2\pi a} = \tau_0 , \tag{2-16}$$

where G is shear modulus, b is Burger's vector, a is distance between planes, τ_0 is critical shear stress. Dislocations are preferred to slip on close packing planes (a_{\max}) and along close packing direction (b_{\min}).

For nanoindentation system, the Berkovich tip creates a complex stress field into the specimen (Figure 20 [53]). For hexagonal close packed structure, the c/a ratio is 1.633. The close packed plane and main prefer slip plane is basal plane (0001). The c/a ratio of epitaxial layer GaN (hexagonal wurtzite structure) is ~ 1.626 , which is close to the hexagonal close structure [11]. As the loading increasing along the c -axis, the structure is compressed. Dislocations preferred to slip on other plans, such as $\{2\bar{1}\bar{1}3\}$ or $\{10\bar{1}2\}$ pyramidal plane, during nanoindentation testing (Figure 17, [55]). On the other hand, when the c/a ratio is over the ideal value >1.633 , the preferred slip plane remain on basal plane. As the indent depth increasing, more dislocations slip on the basal plane and pyramidal plane. The slip planes keep extending by dislocation stacking. Two planes eventually cross together (Figure 21 [57]). To keep the deformation going, the secondary slip planes starts to be active at deeper depths (Figure 22 [53]).

To determine the prefer slip plane, we have to look back to the fundamental theory of the resolved shear stress.

$$\tau_{\text{RSS}} = \sigma \times (\cos\gamma \times \cos\phi)_{\text{max}} , \quad (2-17)$$

where $(\cos\gamma \times \cos\phi)$ is usual seen as the Schmid factor, ϕ represents the angle between the normal vector of the slip plane and the applied stress and γ represents the angle between the slip and stress directions.

The yield stress is the transition point between elastic and plastic deformation. The yielding point can be extracted from the pop-in effect of the nanoindentation load-displacement curve. The load-displacement relationship (P-h) can be well fitted

by the Hertzian contact solution [44, 58]:

$$P = \frac{4}{3} E_s \sqrt{Rh^3}, \quad (2-18)$$

where E_r is the effective modulus of the pair of contacting solids, R is the indenter tip radius. The onset of plastic deformation during nanoindentation is marked by a large displacement burst, as shown in Figure 23 [69]. The large displacement does not imply that the specimen has undergone large plastic deformation. It is mainly a reflection of the major shearing along the slip plane which is called as the pop-in effect. The first pop-in is regard as the initiation of the first slip plane. One should notice that the critical pop-in depth could decrease with decreasing tip radius. The experimental equation of maximum shear stress can be estimated by

$$\tau_{\max} = 0.12 \left(\frac{P_{\text{crit}} E_s^2}{R^2} \right)^{1/3}, \quad (2-19)$$

where P_{crit} is the first pop-in load in nanoindentation. The maximum normal stress is given by [53]

$$\sigma_{\max} = \left(16 P_{\text{crit}} E_r^2 / 9 \pi^3 R^2 \right)^{1/3} = 0.39 \left(P_{\text{crit}} E_r^2 / R^2 \right)^{1/3}. \quad (2-20)$$

It can be seen that, under nanoindentation, τ_{\max} at the contact center is in the range $0.3\sigma_{\max}$. Figure 24 shows the sketch of relationship between resolve shear stress and normal stress.

2.7. Introduction of microcompression testing

In 2004, Uchic et al. [61] published “sample dimensions influence strength and crystal plasticity” in the well known journal, Science. It contains the detailed study of the size effect in single crystal of Ni, intermetallic alloy of Ni₃Al-1%Ta and Ni superalloy single crystal on mechanical properties, using the focused ion beam (FIB) and the nanoindentation system to fabricate micrometer sized compression samples. Three benefits of the microcompression process in this study are: (1) the microcompression samples remain attached to the substrate and easy to handle; (2) the microcompression samples are loaded with the commercial nanoindentation system; (3) the fabrication of microcompression samples by the FIB can be scripted and automated. This technique has been used for the investigation of sample size effects on the mechanical properties of single crystals of metals and alloys, as well as metallic glasses. These methodologies are discussed in the following sections.

2.7.1. Micropillar preparation

The FIB is a very powerful instrument to make transmission electron microscopy (TEM) samples, advanced circuit editing, pattern machining and mostly, site-specific milling. Ga ions operating at 25-30 keV is generally used for fabricating micrometer sized compression samples, termed as the micropillars. Methods of microscale compression sample preparation can be mainly classified into two ways, the annular-milling method and the lathe-milling program method. Generally speaking, the annular-milling is used in preparing a small diameter sample (less than 2 μm) and the lathe-milling program method is for the sample which is larger than 2 μm . Comparisons are described below.

The standard procedure of the annular-milling microscale compression sample preparation process usually consists of two steps [48, 62]. In the first step, rough etching with a high beam current of Ga ions is used to mill the outer crater and outline a pillar. In this step, it is important to fabricate a large crater to make sure that the flat punch indenter will contact the pillar of interest. Additionally, this step is usually performed by using high current (5~20 nA) of the FIB, since the goal is to quickly remove the material around the sample of interest. In the second step, a series of concentric annular milling patterns by a finer beam current are made to reach the final desired diameter. But due to the convergence angle of the Ga ion beam, there is a tapered angle (Figure 25 [48, 62]). The stress or Young's modulus would increase with increasing tapered angle and would cause overestimated values. To solve this problem, it is possible to minimize such taper angle by adjusting the annular milling patterns and decreasing the beam current. But still, it is nearly impossible to produce perfect micropillar samples which having both a uniform cross-section and a well-defined gauge length by using this method alone.

Thus, in order to eliminate the taper of the microcompression sample, Uchic et al. [48, 62] developed another fabrication method of the FIB milling process, the lathe-milling program method, which can possibly lathe off the side of the microcompression sample with the FIB by tilting an angle ($2\sim 5^\circ$). The automatic build-in program is developed to take place of user operating tedious and monotonous steps. Firstly, tilt the sample in $2\sim 5^\circ$, lathed off the side of the pillar with a relatively higher beam currents (1~7 nA), then rotated a small angle ($5\sim 10^\circ$) and milled again. The circular pattern on the top of the pillar is a fiducial mark used as a reference point to reorient the specimen during the incremental milling and unit rotation process. The radius of this mark is a half radius of the expected sample. Through 360° trimming, then

finer beam currents (0.05~1 nA) were used for subsequent steps. Still, there are some disadvantages of this method. Holder should be able to rotate precisely and quickly, or procedure would take too much time. Secondly, there are difficulties in milling a well-defined circular fiducial marker with the diameter smaller than 0.5 μm . Thus, microcompression samples smaller than 2 μm in diameter would be difficult to prepare by the lathe-milling program method (Figure 26 [48, 62]). Considering the rate of milling ($\sim 1000 \mu\text{m}^3/\text{min}^{-1}$) [49, 63], a large microscale sample need not to use this method as well. There are still other micro-machining methods, such as the micro-electrodischarge machining (micro-EDM), femto-second laser ablation, micro-electron-chemical milling and photolithography. The latter methods are used to prepare a slightly larger length scale relative to the previous mentions of two FIB milling methods.

In terms of the micro-electrodischarge machining, it is a critical technology to fabricate high-aspect-ratio 3D microscale samples. However, the surfaces of microscale samples fabricated by the micro-electrodischarge machining will exhibit micro-cracks, resulting in stress concentration and reduction of fatigue strength. For the micropillar preparation, the FIB milling technique seems to be the best choice for this research.

2.7.2. Force loading and measurement

Once the micropillars are fabricated, the samples are then tested in uniaxial compression by using a flat punch tip (Figure 27) in a commercially available nanoindentation system (MTS Nano indenter XP). Due to the conventional nanoindentation system with angstrom displacement resolution of 0.1 nm and load

resolution of 1 nN, it makes the technique popular in many applications such as the measurement of mechanical properties of thin films and tribological measurements of coatings. In particular, the modified nanoindentation plays an important role in performing the microcompression test because the use of a flat punch tip enables the diamond indenter to act as a compression platen. The flat punch tip is also truncated by using FIB, and the schematic description of microcompression test is shown in Figure 28 [64].

2.7.3. Parameters of microcompression tests

According to the two-dimensional and three-dimensional finite element modeling, Zhang et al. [21] have made recommendations regarding allowable fillet radius (r_c), pillar aspect ratio (α), tapered angle (θ) and misalignment of the system. Parameters are shown below respectively.

The first important geometric factor, fillet radius (r_c), is defined as the curvature at the bottom of the pillar which connects to the base (Figure 29 [64]). Compared with input stress, 6% of flow stress error from microcompression would cause by radius/pillar radius ratio $r_c/r = 1$. Error decreases with decreasing r_c/r ratio. This would cause an overestimate of flow stress (Figure 30 [21]). Another issue should be addressed is the distribution of the von Mises stresses in the pillar and the base. The results show that with increase r_c/r , the stress concentration at the fillet is alleviated. It is well known that the stress concentrations may result in localized the sample failure prior to yield. In the case of $r_c/r > 0.5$, there was no obvious stress concentration. Thus, the choice of the r_c/r ratio needs to be judicious. One needs a small r_c/r ratio to obtain the accurate material behavior in the plastic region; another needs a large r_c/r to avoid

the localized failure at the pillar root. In the 2D simulations, the value of r_c/r in the range of 0.2~0.5 is the optimum condition for the microcompression testing. Therefore, this suggests that if the r_c/r is well controlled, the microcompression test can still be used to probe the mechanical properties of materials.

The second important geometric factor is the pillar aspect ratio α . The aspect ratio of the pillars has a relatively small effect on the output flow stress curves when it is larger than 2. The smaller α is the larger output flow stress would be. Because of the constraint result from the pillar base and the output strain hardening of the pillar during the microcompression test, these two reasons will cause the output flow to deviate from the input value. However, the increase of the aspect ratio could increase the affects of the bucking, and causes the decreasing of the output stress. The reason is if pillars are not at just the same stress axis as the tip is, the friction between the pillar top and the indenter tip interface should be considered. Interacting due to these two conflicting affects is displaced in Figure 31 [21], leveling off or stress drop could be seen at the stress-strain curve. The results indicate that the plastic buckling is suppressed by the friction when the aspect ratio is less than 5. Hence, for both 2D and 3D simulation results, Zhang et al. [21] recommended that the aspect ratio of pillars should be around 2~3.

The third important geometric factor is the taper of the pillar. The angle of taper is defined as below:

$$\theta = \tan^{-1}\left(\frac{r_{bottom} - r_{top}}{2h}\right), \quad (2-21)$$

where r_{bottom} and r_{top} are the radius of the bottom and top of the pillar, respectively. h is the height of the pillar. The top surface of the pillar is often smaller than the bottom of the pillar caused by the fabrication of FIB or other micromachining processes. The effects of taper result in an overestimate of the elastic modulus. Due to the taper angle of $\sim 2.86^\circ$, the measured elastic modulus is obviously larger than the input data. Figure 32 [21] shows the contrast taper affects with different aspect ratios, though the small aspect ratio would cause overestimation. Figure 32 shows that the overestimation of output stress caused by taper is increased more than the aspect ratio did. Thus, to avoid the load drop and minimize the overestimate of the output stress, the small aspect ratio and small taper angle must be chosen.

Finally, the last important factor that might cause the primary deviation of the stress-strain curve and affect the accuracy of testing elastic region of microcompression is the effect of misalignment of the system. This misalignment is the angle between the normal direction of the flat punch indenter tip and the pillar axis. It gives rise to an underestimate of the elastic modulus of the material (Figure 33). [21] The measured elastic modulus decreases with misalignment increasing. The excessive misalignment may result in buckling of the pillar. From 3D simulation, the results indicate that even perfect alignment ($\theta = 0^\circ$) has 20% of underestimating the elastic modulus. Therefore, the elastic modulus should time at least 1.25 from the microcompression testing.

2.7.4. Microscale characterization of mechanical properties

In 2004, Uchic et al. [61] have discovered the size effect of Ni, intermetallic alloy of Ni_3Al -1%Ta and Ni superalloy single crystal. In their results, the strength of small sample size (5 μm , Ni_3Al -1%Ta alloy) rose dramatically from 250 MPa for a

20- μm -diameter sample to 2 GPa for a 0.5- μm -diameter sample. Sample size larger than 20 μm had similar mechanical properties with bulk samples. In contrast, 10- μm -diameter Ni superalloy single crystal did not show the same effect as the Ni_3Al -1%Ta alloy, due to its fine precipitates that provide the strong internal hardening mechanisms and preempt the influence of the external dimensions.

In 2005, Greer et al. [65] observed the same phenomenon on microscale Au samples too. Strength significant increased for more than one order of magnitude in submicron pillar samples. They claimed that the high strengths in microcompression were caused by an indication of dislocation starvation. Dislocations are believed to pass through the sample free surface and out of the crystal before they have an opportunity to interact and multiply. Without the contribution of dislocations, the strength will tend toward to theoretical strength. To confirm this explanation and to exhaust the artifact condition during the sample preparation process, Greer et al. [65] developed an alternative fabrication technique based on lithographic patterning and electroplating. Their results on microspecimen fabricated by both FIB milling and lithographic patterning and electroplating indicate that the strength increase is not artificial. Volkert et al. [66] have also examined the similar sample size effects in submicron pillar sample and attributed their results to source-limited behavior in small volumes.

In 2006, Uchic and co-workers [67] demonstrated the microscale compressive behavior of the $\text{Ni}_{76}\text{Al}_{24}$ alloys by means of microcompression tests. They found that the events of strain burst were observed in the stress-strain curves of microscale samples. The strain burst means that the strain (or displacement) takes place almost instantly and it was much similar to the so-called the pop-in effect for the nanoindentation compression testing. Figure 34 [67] shows the SEM micrograph

analysis, indicating the number of observable slip bands is approximately the same as the number of strain bursts.

Similar research published in 2006 by Schuster et al. [68], the maximum yield strength of the microscale compressive properties of electrodeposited nanocrystalline Ni is 1498 MPa for the 20 μm diameter samples. The result of the Mo-10Al-4-Ni alloy was reported by Bei and co-workers in 2007 [69]. The results show that the micropillars are all yielded, regardless of the size, at a critical resolved shear stress of $G/26$, where G is the shear modulus, it is in the range expected for the theoretical strength, from $G/30$ to $G/10$.

To date, the microcompression tests on single-phase metals have generally shown distinct size effects, the yield and flow strength increase with decreasing pillar diameter. These dramatic effects are attributed to dislocation starvation because the size of the sample is smaller than the characteristic length scale of dislocation multiplication. It would result in a strength approaching to the theoretical strength.

2.8. Thermal treatment of ion implanted semiconductors

Zinc oxide and its allied binary MgO and CdO, as well as gallium nitride and its allied binaries InN and AlN, have risen the interesting due to their adaptable wide bandgap. Band gap can be adopted by doping ions into the sample. But the implantation usually follows with the surface and crystal quality damage. Besides, the unintentional implantation during process, such as Ga ion implantation during the focus ion beam processing, will increase the point defects density and affect the performance of luminescence as well. Hence, to enhance the luminescence intensity

and signal/noise ratio of spectra, two methods: inductive couple plasma etcher (ICPE) and thermal treatment are considered as solutions to improve the surface quality. In this study, we focus on the annealing process because it provides a relatively convenient method to refine the crystalline [70, 71]. The following is the brief introduction of the surface damage and crystalline effect from ion implanting.

2.8.1. Defects and ion implantation

The luminescence is very sensitive with the defects and ion implantation. Table 10 reveals the relationship of the related dopant to band gap energy for the GaN PL spectrum [72]. Defects usually are attributed to the cause of reducing efficiency, laser lifetime, signal/noise ratio and stability of electrical/lightening devices. The low dimensional defects can be classified as point defects and line defects. Figure 35 [57] and Figure 36 [57] show the nanoindentation induced defects caused the degeneration of CL luminescence. The line defects can be classified as in-growth threading dislocations and stress-induced dislocations. The in-growth dislocation density is typically in the range of 10^9 - 10^{10} cm^{-2} on sapphire substrate. Threading dislocations can be observed and quantized by high resolution transmission electron microscopy images (HRTEM). The dislocation density decreases with increasing thickness (Figure 37 [80, 96]). In this study, the threading dislocation density of ZnO and GaN are $\sim 10^2$ cm^{-2} (c-plane) and $\sim 10^9$ cm^{-2} (c-plane), respectively. Following is the character of each type of defects and its influence.

There are not many methods able to quantize individual point defects, but the character of point defects can be simply classified as following. The point defects include native isolated defects (anion and cation vacancies, interstitial and

substitutional native atoms), intentional impurity (GaN: Al or In, ZnO: Mg or Cd) and unintentional impurity (hydrogen, oxygen or gallium ion in FIB process). Equation 2-22 gives the upper limited of concentration point defects (c) under thermodynamic equilibrium,

$$c = N_{\text{sites}} \exp\left(\frac{S_f}{k} - \frac{E_f}{kT}\right), \quad (2-22)$$

where N_{sites} is the concentration of sites which defects can be incorporated in the lattice ($\sim 4.4 \times 10^{22} \text{ cm}^{-3}$ for substitutional defects in GaN), S_f is the formation entropy ($\sim 6k$), k is Boltzmann constant, E_f is the defect formation energy, and T is environment temperature. The formation energy becomes the key parameter to estimate the point defect concentration at high temperatures. Figure 38 lists the formation energy of substitutional sites (Ga_N : gallium at nitrogen site and N_Ga : nitrogen at gallium site), interstitial sites (Ga_i and N_i) and vacancies (V_Ga and V_N). The slope in Figure 38 represents the charge state of each point defect which is shown in Figure 39 [74]. It is clear to see that native substitutional defects in GaN have relatively high formation energy. Thus, the gallium and nitrogen vacancies are much easier to be formed than substitutional or interstitial defects during the growing processing. The V_Ga may be the dominant native defects in n-type GaN and V_N may be formed numerously in p-type GaN.

For intentional impurity, many researchers are trying to improve several properties, such as bandgap, carrier density, carrier mobility, of GaN and ZnO by adding impurities. Both GaN and ZnO are intrinsic n-type characteristic semiconductors. It is because the formation energy of V_cation is less than other defects. The

self-compensation and unintentional hydrogen implantation cause the intrinsic n-type character as well [71, 73]. For increasing donors in n-type semiconductors, one can intentionally substitute zinc by group III elements (aluminum gallium or indium) in ZnO, or substitute gallium by doping silicon, oxygen, germanium in GaN [72]. But to make the high quality laser/LED device, more steady and reliable p-type semiconductor is needed. ZnO can be alternative as a p-type semiconductor by doping group I element (Li, Na and K), group V element (N, P and As), copper or even silver into the semiconductors [30]. For substituting group V element (for example nitrogen) in oxygen sites, one extra carrier gains and provides a shallow acceptor. The hole mobility measured by Hall measurement increase to $\sim 2 \text{ cm}^2/\text{Vs}$, hole concentration to $9 \times 10^{16} \text{ cm}^{-3}$ and the acceptor energy level is about 170-200 meV. In addition, doping Group I atom, lithium, introduces a deep acceptor levels and induces ferroelectric properties [30]. For GaN, it can dope carbon, beryllium, calcium, cadmium or manganese for gaining more acceptors [72]. But there are still difficulties to produce reliable p-type semiconductors. One is the radii difference between atom and impurity. Table 11 [30] lists the ionic radii of dopant in growing p-type ZnO.

2.8.2. Defects recovery

The annealing process is widely used to refine the crystal and to enhance the luminescence quality. To know the relationship between defects migration and bandgap changing, we should look into the detail of the energy level of each dominated defects. Although the ionic vacancies have relatively low formation energy than other defects, one should note that higher charge native defects or interstitial/substitutional defects could be formed after the electron irradiation or ion implantation.

For n-type GaN, the donor-like defects, such as V_{Ga} , have the lowest formation energy than any other type of defects in n-type. The abundantly formed Ga vacancies become the dominated defects which are completely filled with electrons, and capture of a photo-generated hole. During photoluminescence measurements (such as cathodoluminescence or photoluminescence), may lead to radiative transition of an electron from the conduction band/a shallow donor level to the level of $V_{\text{Ga}}^{3-/2-}$ (Figure 38 [74]). For wide bandgap semiconductor (ZnO and GaN), the conduction band level is about 3.3 eV. The acceptor-like gallium vacancy V_{Ga}^{3-} has relatively high formation energy than other level of Gallium vacancy. The migration barrier is 1.9 eV to V_{Ga}^{3-} . Therefore, the Ga vacancies are mobile in a wide range of temperatures typically used during growth or thermal annealing. It is likely that they migrate and form complexes with more stable defects [72]. For p-type GaN, the dominated $V_{\text{N}}^{3+/+}$ defects are acceptor-like defects in Ga-rich p-type GaN. The migration barrier of +1 charge is 2.6 eV. The estimation is not as high as the theoretical value (>3eV) due to the defects migrate through the saddle point (from near octahedral site to tetrahedral site then go back to octahedral site). The rest migration barriers of native defects are listed in Table 12 [74]. Shallow native defects, such as interstitial defects and vacancies, have low migration barriers which make the annealing process be able to drive the shallow defects to the surface.

In this study, focus ion beam (FIB) is used to mill the GaN and ZnO pillars. The unintentionally implanted Ga ion, hydrogen and vacancies will change the bandgap and luminescence performance. The minimum atomic radius mismatch is Zn^{2+} (0.75 Å) substituted by Ga^{3+} (0.6 Å) [30]. So far, Ga implantation in ZnO and GaN is yet to be investigated in details. But related researches have been published, such as crystalline

structure recovery from argon (Ar) [71], phosphorous (P) [75], cobalt (Co) [76], antimony (Sb) [77] and thulium (Tm) [78] implanted damage in bulk ZnO, vanadium (V) implanted in ZnO nano-rods [79], electron-irradiated induced vacancies [73] as well as nitrogen (N), argon (Ar) and erbium (Er) implanted damage at low temperatures (~15 K) [80] by annealing process. The Raman, photoluminescence and cathodoluminescence spectrums provide fine measurements on structure and band gap identification in submicron-scale. The studies indicate when ZnO is annealed at 800°C for one hour, the surface becomes flatter (from 1.3 nm to 0.2 nm by atomic force microscopy). The FWHM (full width at half height) of the X-ray diffraction rocking curve mode is narrower than the implanted sample. The increased intensity of photoluminescence shows better lighting performance. The decreased intensity of $A_{1(LO)}$ peak in Raman spectrum reveals lower point defects in structures [71]. All this researches imply the possibility to refine the crystal quality by thermal treatment [70, 71].

2.9. Luminescence properties of semiconductors

In order to research the contact loading during processing and packaging degradation of the optical and electrical performance, the photoluminescence (PL), cathodoluminescence (CL) and the Raman spectrums have been widely used in this field. To analysis implantation and indentation induced defects of semiconductor films, The Raman spectrum and X-ray diffraction rocking curve mode provide accurate methods of measuring structure quality. The FWHM of X-ray rocking curves can roughly indicate the defect densities and the micro-Raman spectroscopy system can provide a good resolution (~300 nm beam size) in surface identification of the defect types, distribution and residual stress after annealing process, indentation testing and

compression testing [14, 81-84]. The CL and PL spectroscopy provide a precise way to investigate the relationship between defects and luminescence performance changing in details.

2.9.1. Raman spectrum

In 1996, Wolf reviewed the studies of micro-Raman spectroscopy to study local mechanical stress in semiconductor material silicon [69, 85]. Figure 40 reveals the sketch diagram of micro-Raman spectrometer [82]. The laser beam goes through the polarizer then incidents on the crystal. The high frequency photons induce the electrical in the structure. Then the vibration or rotation of the molecules causes the energy lost by generating both phonons and low frequency photons. This kind of photon-phonon interaction is called “anti-Stokes scattering” (Figure 41 [82]). The ideal scattering must obey the conservation of the energy, which can be presented in wavenumber as below:

$$\omega_l = \omega_s + \omega_o, \quad (2-23)$$

where ω_l , ω_s and ω_o are the wavenumber of laser, scattering phonon and photon respectively. It is the most common interaction and the main intensity of Raman spectrums.

Two tensors of optical phonon are defined as transverse optical phonons (TO) and longitudinal optical phonons (LO). The characterizations of these two phonons are depending on which surface is indicated and observed. Figure 42 implies the main Raman active peaks (E_1 , A_1 , E_2) of the Raman spectrum of wurtzite structure ZnO [82]. The A_1 peak has polarized direction on c-axis [0001] and the E_1 peak has polarized

plane on c-plane (0001). E_2 peak can be seen as a standard peak which has no sensitivity to the optic axis [54]. Both GaN and ZnO are electrostatic force dominated, which means $A_{1(LO)}$ and $E_{1(LO)}$ peaks are closer than $E_{1(LO)}$ and $E_{1(TO)}$. Other geometry effects of sub-Raman peak, such as surface optical phonon, are affected by the $A_{1(TO)}$ peak. The relationship between surface optical and $A_{1(TO)}$ mode phonon is shown as following:

$$\omega_{SO}^2 = \omega_{A_{1(TO)}}^2 \frac{\varepsilon_0 + 2\varepsilon_m}{\varepsilon_\infty + 2\varepsilon_m}, \quad (2-24)$$

where ω_{SO} and $\omega_{A_{1(TO)}}$ are the wavenumber of surface optical phonon and $A_{1(TO)}$ peak respectively, ε_0 (~ 10.4 for GaN) and ε_∞ (~ 5.8 for GaN) are the static and high frequency dielectric constant of material, ε_m is the dielectric constant of material [86].

Two types of measured modes, back scattering and right angle scattering are considered in this study. For ideal back scattering Raman spectrum (Figure 43 [82]), laser beam indicated and detected through the same direction. Some of the peaks are invisible due to the different indicated and detected direction. By the selection rule, both $A_{1(TO)}$ and $E_{1(TO)}$ peak are forbidden, only E_2 and $A_{1(LO)}$ peaks can be shown in c-axis [0001] back scattering Raman spectrum. The ideal right angle scattering means the angle between incident and detected direction is 90 degree (Figure 44). In this case, $A_{1(LO)}$ and $E_{1(LO)}$ are combined into a quasi-peak between $A_{1(LO)}$ and $E_{1(LO)}$ wavenumber (Figure 45). But in reality, the slight deviation of alignment, the rotation of crystalline and the solid angle of laser beam will induce small intensity of forbidden peaks [54, 87].

The analysis of Raman spectrum in this study are mainly focused on the E_2 peak

shifting and the intensity changing on A_1 peak, which are corresponding to the residual stress and native point defects concentration. The hydrostatic residual stress in GaN can be calculated by the wave number of E_2 peak shifting. For hydrostatic residual stress, the literature values of E_2 peak shifting is 2.4 to 3 $\text{cm}^{-1}/\text{GPa}$ [88, 89]. For the uniaxial stress, the corresponding E_2 peak shifting value is 1.9 $\text{cm}^{-1}/\text{GPa}$ [90]. In addition, the boarding of E_2 and $A_{1(\text{LO})}$ peak can be seen as a rough symbol of the degradation of crystal quality [71]. Raman mapping can imply the distribution of defects as well as the residual stress at the particularly place of sample. By comparing the results of the Raman mapping, the cross section transited electron microscopy (XTEM) and the atomic force microscopy (AFM), one can get the planar analysis in details.

The near surface vertical analysis can be roughly achieved by changing laser source into shorter wavelength laser beam. For most of the materials, different wavelengths have different absorption coefficients. The relationship of penetration depth and the absorption coefficient is shown below:

$$d_p = \frac{2.3}{2\alpha}, \quad (2-25)$$

where d_p is penetration depth and α is the absorption coefficient in the crystalline for different wavelengths.

2.9.2. Luminescence spectrum

Photoluminescence (PL) and cathodoluminescence (CL) can be good tools to study the relationship between stresses, deformation induced defects and

luminescence band gap changing. Both PL and CL spectrometers are set to detect the changing of band gaps by using photon and electron to emit the electron, but there are still some differences between PL and CL spectrometers. The PL spectrometer can easily be set at ambient environment with optical microscopy, but the planar resolution ($\sim 10 \mu\text{m}$) is limited by optic lens aberrations, monochromater and laser wave length. The CL spectrometer is built in scanning electron microscopy (SEM). Due to the high accelerated voltage (30 kV), it can provide smaller beam size, better resolution and stronger intensity to emit electron. It could also verify the morphology and peak changing by comparing the secondary electron images (SEI) and CL mapping images in real-time [91].

Table 10 reveals the band gaps corresponding to different defects or dopants of GaN. The main band gap of GaN and ZnO can roughly distinguish as ultra-violet (UV) and blue luminescence (UV/BL $\sim 3.3 \text{ eV}$), green luminescence (GL $\sim 2.4 \text{ eV}$), yellow luminescence (YL $\sim 2.2 \text{ eV}$) and red luminescence (RL $\sim 1.9 \text{ eV}$) [92, 72, 93]. The region of UV band luminescence is considered as the perfect crystal region (3.3 eV). The degradation of UV band is usually referred to the defects, impurities or biaxial strain. The near edge peak shifting corresponding to the E_2 Raman peak is 6.4 meV/cm [89]. The GL band is imputed to the native structure defects (Ga vacancies), defects interaction ($V_{\text{Ga}}\text{-O}_{\text{N}}$) or Pt coating on Ga-face atomic layer. The YL band is attributed to the shallow structure defects on N-face atomic layer. The YL is easily to be saturated. The excess energy then transfers to the GL band gap, turns into a broad peak and induces the maximum peak shifting [72, 93]. Both GL and YL bands are hard to identify at ambient environment (272 K). The environmental radiation will cover these bands and become a hump in the spectrum. It requires low temperature CL and PL (4 K) to analysis further information in details. The RL band is referred to

the deep donor (V_N-C_N), acceptor ($V_{Ga}-O_N$), shallow donor (Pt) and other impurities. For dislocations induced luminescence changing, the screw dislocation component causes the non-radiation donor-acceptor recombination.

The relationship between mechanical properties and luminescence performance of semiconductors can be studied by using the nanoindentation system, the micro-Raman spectroscopy and the PL/CL spectroscopy [57, 92, 94, 95]. In 2002, Bradby et al. [57] used the spherical indenter tip with $\sim 4.2 \mu\text{m}$ radius to test the $2 \mu\text{m}$ thickness wurtzite epilayer GaN at the loads 25 mN, 50 mN, 200 mN and 250 mN. Figure 35 [57] shows the load-displacement curve at maximum load of 250 mN, a single discontinuity is clearly observed at the load ~ 35 mN. But when the load is set at 50 mN, the multi-pop-in are found at the load ~ 28 mN and ~ 34 mN. The pop-in effect was seen as a displacement burst and “footprint” of deformation. It can be seen as purely elastic region before the critical pop-in load (28 mN). Figure 36 [57] reveals the monochromatic CL images after loading at 25 mN, 50 mN and 200 mN. The average dark regions in the CL spectrum were $3 \mu\text{m}$, $5 \mu\text{m}$ and $11 \mu\text{m}$, respectively. The Star-David-like rosettes have been observed only at high loading indentation. It is reasonable that there is no detectable reduction of UV band intensity of the CL spectrum when the indentation loading (25 mN) is smaller than the critical pop-in load (28 mN).

Chapter 3. Experimental procedures

3.1. Sample preparation

The high quality GaN thin films and ZnO wafers used in this research were from MTI Corporation, USA. The c-plane, m-plane and r-plane GaN epitaxial template (5 mm × 0.5 mm × 5 μm) on m-plane sapphire is made by a hydride vapor phase epitaxy (HVPE)-based method. During the HVPE process, HCl reacts with molten Ga to form GaCl, which in turn reacts with NH₃ to form GaN. The FWHM of XRD rocking curve is 0.341° which shows high quality crystallize (Figure 46). The dislocation density is about 10⁸ cm⁻² (Figure 37). All the GaN thin films are grown by MTI Corporation, USA.

The ZnO wafers are grown by hydrothermal method under high pressure. ZnO crystals are manufactured by the hydrothermal technology. Its advantage is the size of the grown crystals and excellent quality. Growing ZnO by hydrothermal method is quite a slow process, which allows to achieve a very high quality of the crystal, without block marks, twins and dislocations. Hydrothermal ZnO single crystals are grown in high pressure autoclaves by means of direct temperature drop in aqueous solutions of KOH + LiOH at crystallization temperature 320 - 400°C and pressure 20-70 MPa. Inside the autoclaves there are special vessels made of corrosion-resistant alloys – they serve to protect autoclaves from corrosion. The charge, the bait and the chemical solution are put into the vessel, and then the vessel is hermetically sealed and placed into the autoclave. Finally the autoclave is filled with water and is also sealed hermetically. After that the autoclave is heated to the fixed temperature. The

whole production cycle takes 100-150 days. The dislocation density of c-plane is $<10^2$ cm^{-2} . The surface roughness Ra is $< 10 \text{ \AA}$. The FWHM of XRD rocking curve is 0.013° [80, 96]. All the ZnO wafers are grown by MTI Corporation, USA.

3.2. Nanoindentation testing

The fundamental mechanical properties are extracted by using commercially available nanoindentation system (MTS Nano indentation XP). Two Berkovich tips with different radius ($\sim 100 \text{ }\mu\text{m}$ and $\sim 600 \text{ }\mu\text{m}$) are used in this study. Both tips are calibrated by a standard silica sample with over 25 data. To get the depth-modulus/hardness relationship, tests were conducted under the continuous stiffness measurement (CSM) function with constant displacement rate mode at a strain rate of 1~10 nm/s. The allowable drift rate limit is $\sim 0.05 \text{ nm/s}$, which is 2.5% of harmonic displacement target (2 nm with 45 Hz). The depth limit is set to be $< 500 \text{ nm}$ to avoid the substrate effect. The distant between each indentation point is 10 times to the target depth for avoiding residual stress field. The loading rate control function (LRC) is used for analyzing near surface region nanoindentation and stimulating Hertzian contact theory. The constant loading rate is set to be $3.3 \times 10^{-5} \text{ N/s}$, which is about 1~10 nm/s. The datum collection rate is $5 \sim 30 \text{ s}^{-1}$.

3.3. Microcompression testing

The uniaxial mechanical properties are extracted by MTS nanoindentation system with FIB-milled flat punch tip. Micropillars were milled by FIB. After the annealing process and Microcompression testing, CL and Raman spectroscopy were used to address the changing. Then the micropillars were milled into XTEM sample

by the FIB system. The following is the detail of each process.

3.3.1. Microcompression sample fabrication using FIB

The microcompression samples are prepared using the dual focus ion beam system (FIB) of Seiko, SMI3050 SE, following the method developed by Uchic et al. [61]. A Ga beam operated at 30 keV and 7-12 nA is initially directed perpendicular to the surface of the GaN thin film to mill a crater with 35 μm in diameter. The bigger crater is necessary to leave sufficient space for the flat punch tip in the microcompression tests. Then, the same voltage and smaller currents of 0.7 to 0.09 nA are used to refine the preserved island in the center to a desired diameter and height of the pillar. A series of concentric-circle patterns are utilized to machine the pillars. The 1 μm -diameter-pillar in this study is defined as the diameter at the half height. The Ga ion side damage is about 20 nm thick with amorphous phase.

3.3.2. Thermal treatment

To reduce the degradation of luminance intensity and to refine the crystal quality after the FIB process, the samples are annealed in ambient environment by 1400°C electronic furnace of Kurt, K1-15FB-25-160. Samples are heated from room temperature to 800°C over the heating time of 80 min (with a heating rate of $\sim 10^\circ\text{C}/\text{min}$) and held for one hour. Then the samples are cooled down in air atmosphere. The thermal treatment can reduce the damage layer by vaporizing the amorphous layer or refining the crystal structure.

3.3.3. Microcompression test using the nanoindentation system

While calculate the Young's modulus of uniformly tapered pillar in elastic region, we should start from the basic definition of the Hook's law. The engineering strain-stress formula is defined as:

$$\sigma = E\varepsilon, \quad \sigma(x) = \frac{P}{A(x)}, \quad \varepsilon(x) = \frac{\Delta h(x)}{h_0}, \quad (3-1)$$

where P is the instantaneous load, A is the cross section area, Δh is the displacement and h_0 is the pillar height. As $\sin \theta \approx \theta$,

$$E_{pillar} = \left(\frac{P}{\Delta h} \right) \left[\frac{\ln \left(1 + \frac{2h\theta}{d} \right)}{2\pi d \theta} \right], \quad (3-2)$$

where $\left(\frac{P}{\Delta h} \right)$ can be found from the slope of loading p-h curves [21], d_0 is the pillar diameter and θ is the taper angle. Tests were conducted under the CSM mode with constant displacement rate ~ 10 nm/s. The allowable drift rate limit is ~ 0.05 nm/s, which is 2.5% of harmonic displacement target (2 nm with 45 Hz). The displacement limit is set to be one tenth of the film thickness to avoid the substrate effect for thin films.

3.3.4. TEM sample fabrication using FIB

In order to observe the detailed microstructure of pillar sample before and after the

deformation, the cross section TEM samples are prepared by the FIB system. Figure 47 is a schematic illustration of the trenching and liftout technique [97]. Firstly, in order to provide a supporter and protection of the pillar, a fine carbon layer was deposited around the surface with tilt angle 55° by electron beam. Then the main supporter ion-beam carbon layer was deposited from the top. Carbon layer was deposited for avoiding the ion-beam damages from the top. Then, the slope-etching mode is employed to cut a trapezium trenches around the pillar. The high resolution XTEM samples could be thinned to thickness <100 nm by using the lower voltages and currents Ga ion beam. Finally, the TEM samples were moved on a carbon-coated Cu grid.

3.4. Property measurement and analyses

3.4.1. X-Ray diffraction analyses

The quality and composition of sample were examined by the X-ray diffractometer (SIEMENS D5000 X-ray diffractometer, Cu K_α radiation $\lambda = 1.5406 \text{ \AA}$). The high quality crystalline structure causes high peak intensity which way beyond the limit of detector. Low voltages (20 kV), low currents (5 mA), 0.01 mm graphite monochromator with 1 mm filter and the 0.08 and 0.2 mm decreasing slits are used to reduce the intensity. Pre-scans are taken over at 2θ range of 20° to 80° with a scanning rate of 0.1° per second. After knowing the GaN c-plane (0001) K_α peak ($2\theta = 34.62^\circ$), the sample was tilted until the strongest counts appeared. Then the rocking curve mode could measure the misorientation range by rotating sample. The quality of the sample could be identified by scanning the rotation angle θ from 16° to 18.5° to measure the full width at middle height (FWMH). The narrower the FWMH is, the finer quality of

the sample would be.

3.4.2. Scanning electron microscopy (SEM) analysis

The scanning electron microscope (SEM, JEOL ISM-6330 TF) equipped with the energy dispersive X-ray spectrometer (EDS) is mainly used for measuring the composition of samples, the thickness, height, diameter of pillars and observing the morphology of deformed pillars. The accelerate voltage is 30 kV. The fringes on the pillar surface can help us to decide the milling direction of XTEM samples. Further texture analysis can be examined by electron back-scattered diffraction (EBSD) which is build in the SEM as well.

3.4.3. Transmission electronic microscopy (TEM) analyses

The TEM samples were examined by using the JOEL 3010 analytical scanning transmission electron microscope (JOEL 3010 TEM) at accelerated voltage 200-300 kV and the FEI E.O Tecnai F20 G2 MAT S-TWIN field emission gun transmission electron microscope (Tecnai TEM) at accelerated voltage 200 kV. The high quality TEM samples are milled to thickness less than 100 nm by the FIB system. The beam direction \vec{B} can be index by crossing two diffraction vectors:

$$\vec{B} = \vec{g}_1 \times \vec{g}_2 \quad . \quad (3-3)$$

There are three ways to indentify diffraction patterns:

- i. The length of \vec{g} could be measured from the distance between the transmit beam and the diffraction points, the length of vector \vec{g} is the reciprocal of d-spacing:

$$|\vec{g}_{hkl}| = \frac{1}{d_{hkl}} \quad . \quad (3-4)$$

We can find the closest d-spacing plane system by comparing to the main deformation systems in stimulated diffraction patterns (by the Carine program).

- ii. Measuring the angle between two \vec{g} vectors, and check if they are fitting with the theoretical value between two planes in the periodicity lattice.
- iii. By measuring the ratio of the length of two \vec{g} vectors, values should correspond to the ratios of two lengths in periodicity lattice.

The formula $\lambda L = Rd$ could be used to calculate the d-spacing by knowing that R is the length of \vec{g} vector, λ is the electron wavelength of electron gun (3 pm for the 200 kV TEM) and L is the camera length (160 - 2330 mm for select area diffraction aperture on current TEM).

3.4.4. Raman spectrometer analyses

The back scattering micro-Raman spectroscopy was conducted by mode-built confocal spectroscopy. The 532 nm He-Ni laser is used as the input source. The main peaks of Raman spectra are then fitted by Gaussian distribution. The planar resolution is about 300 nm. The mapping images are sketched by extracting 14 x14 points of E₂

peak shifting (compare to the literature value of free standing sample) by the MATLAB software.

3.4.5. Cathodoluminescence (CL) spectrum analyses

Cathodoluminescence spectroscopy (CL) is set in SEM (JEOL -JSM-6330 TF). The accelerated voltage is 15 kV. Measurement took place at room temperature. The effective range is about 3~4 μm^2 . The point, line and area scan are available in this system. The resolution of wavelength is 0.1 nm. The CL mapping and SEI images can reveal the degree of luminescent intensity changing and morphology changing at precise wavelength. The rosette pattern of CL mapping reveals the defect distribution after nanoindentation testing. The monochromater can show the details of bandgap changing.

The vertical analysis can possibly be reached by two methods. The non-destructed measurement is changing the effective region by adapting accelerated voltage. The destructive method is cross section cathodoluminescence measurement (X-CL). The specimens can be liftoff as X-TEM process. Only the thickness and width are larger. The X-CL specimens are then fixed on Cu foils. Low accelerating voltage is used to prevent the electron beam stabbed into the carbon film.

Chapter 4. Experimental results

4.1. Structure quality identifications

4.1.1. X-ray diffraction analyses

The quality of the c-GaN thin film is double-checked by the X-Ray diffraction (XRD), as shown in Figure 48. The XRD pattern shows a sharp peak located at $2\theta = 34.62^\circ$ with 28040 counts which corresponding to the estimation from CaRine software and reference (Figure 49). Under low voltages and low currents, the extremely high counts of the peaks suggest the GaN is a high quality single crystal structure. The rocking curve pattern shows a peak ranging from 16.45° to 17° with the full width of half maximum (FWHM) = 0.341° (Figure 50), the broad peak suggests pre-exist threading dislocations in the template GaN thin film. The result is similar to the data from MTI Co. (Figure 46, $1750''=0.486^\circ$) The FWHM of ZnO wafer is $47''=0.013^\circ$.

4.1.2. EBSD analyses

The EBSD patterns can identify the main direction groups of the specimens. Figure 51 and Figure 52 reveal the SEM SEI image and the corresponding EBSD patterns of c-ZnO and GaN, respectively. The identification of direction groups can provide a map to estimate the direction of deformation. So we can ensure the cross-sectional TEM samples are milled precisely at the main deformation planes.

4.1.3. Theoretical values calculations

For estimating the mechanical properties and confirming the experimental results, some fundamental theoretical values needs to be calculated. For ZnO, by filling in the elastic constants $C_{11} = 209.7$, $C_{12} = 121.1$, $C_{13} = 105.1$, $C_{33} = 210.9$, $C_{44} = 42.5$ and $C_{66} = 44.3$ (Table 8 [16]) into equation 2-14. We can get a determinant $\sigma_{ij} = C_{ij} \times \varepsilon_{ij}$:

$$\begin{bmatrix} \sigma_1 \\ \sigma_2 \\ \sigma_3 \\ \sigma_4 \\ \sigma_5 \\ \sigma_6 \end{bmatrix} = \begin{bmatrix} 209.7 & 121.1 & 105.1 & 0 & 0 & 0 \\ 121.1 & 209.7 & 105.1 & 0 & 0 & 0 \\ 105.1 & 105.1 & 210.9 & 0 & 0 & 0 \\ 0 & 0 & 0 & 42.5 & 0 & 0 \\ 0 & 0 & 0 & 0 & 42.5 & 0 \\ 0 & 0 & 0 & 0 & 0 & 44.3 \end{bmatrix} \begin{bmatrix} \varepsilon_1 \\ \varepsilon_2 \\ \varepsilon_3 \\ \varepsilon_4 \\ \varepsilon_5 \\ \varepsilon_6 \end{bmatrix} . \quad (4-1)$$

For calculating the Poisson ratio of the c-plane, we can assume no normal stress on a-axis, which leads the result $0 = C_{11}\varepsilon_1 + C_{12}\varepsilon_2 + C_{13}\varepsilon_3$. The definition of the Poisson ratio is

$$v_{s,c-plane} = -\frac{\delta\varepsilon_1}{\delta\varepsilon_3} . \quad (4-2)$$

By differentiate $0 = C_{11}\varepsilon_1 + C_{12}\varepsilon_2 + C_{13}\varepsilon_3$, the c-plane Poisson ratio can be calculated by

$$v_{s,c-plane} = -C_{13} / (C_{11} + C_{12}). \quad (4-3)$$

For calculation the a-plane Poisson ratio $v_{s,a-plane}$, we assume no normal stress on

c-axis and simplified a₁ stress $\sigma_1 = 1$, which leads two equations

$$\begin{aligned} 0 &= C_{13}\varepsilon_1 + C_{13}\varepsilon_2 + C_{33}\varepsilon_3, \\ 1 &= C_{11}\varepsilon_1 + C_{12}\varepsilon_2 + C_{13}\varepsilon_3. \end{aligned} \quad (4-4)$$

The a-plane Poisson ratio can be derived as

$$v_{s,a-plane} = \frac{C_{12}C_{13} - C_{11}C_{33}}{C_{13}^2 + C_{12}C_{33}} \quad (4-5)$$

By assuming uniaxial stress comes from only the c-axis ($\sigma_1 = 0$, $\sigma_2 = 0$ and $\sigma_3 = 1$), we can get the corresponding Poisson ratio of the c-plane ZnO to be $v_{s,c-axis} = 0.33$ which is compatible to the literature result [59]. By assuming uniaxial stress coming from only the a-axis ($\sigma_1 = 1$, $\sigma_2 = 0$ and $\sigma_3 = 0$), we firstly calculated the corresponding Poisson ratio of a-axis ZnO to be 0.25. There is apparent anisotropy for the c- and a-axis. The Poisson ratio strongly affects the results of modulus. The modulus is one of the fundamental mechanical properties that one material stands for.

For estimating the theoretical value of Young's modulus, we can simply follow the basic definition of modulus which is

$$E = \frac{\varepsilon}{\sigma}. \quad (4-6)$$

For low dimensional stress analysis, it is much easier to stimulate the stress than the

strain. The Young's modulus can be derived by the stiffness matrix. The stiffness matrix is the reverse matrix of elastic constant matrix. The relationship is shown below:

$$\begin{aligned}
(C_{11}+C_{12}) &= S_{33}/S \\
C_{13} &= -S_{13}/S \\
C_{44} &= 1/S_{44} \\
(C_{11}-C_{12}) &= 1/(S_{11}-S_{12}) \\
C_{33} &= (S_{11}+S_{12})/S \\
S &= S_{33}(S_{11}+S_{12})-2S_{13}^2.
\end{aligned} \tag{4-7}$$

The solution of equations is shown below:

$$\begin{aligned}
S_{11} &= \frac{1}{2} \left[\frac{1}{C_{11}-C_{12}} + \frac{C_{13}}{[(C_{11}+C_{12})C_{33}-2C_{13}^2]} \right] \\
S_{12} &= S_{11} - \frac{1}{C_{11}-C_{12}} \\
S_{13} &= \frac{-C_{33}}{[(C_{11}+C_{12})C_{33}-2C_{13}^2]} \\
S_{33} &= \frac{(C_{11}+C_{12})}{[(C_{11}+C_{12})C_{33}-2C_{13}^2]} \\
S &= [(C_{11}+C_{12})C_{33}-2C_{13}^2]^{-1}.
\end{aligned} \tag{4-8}$$

Considering the symmetric of wurtzite structure and taking normal stress only into consideration, the stiffness matrix can be present by:

$$\begin{bmatrix} \varepsilon_1 \\ \varepsilon_2 \\ \varepsilon_3 \end{bmatrix} = \begin{bmatrix} S_{11} & S_{12} & S_{13} \\ S_{12} & S_{11} & S_{13} \\ S_{13} & S_{13} & S_{33} \end{bmatrix} \begin{bmatrix} \sigma_1 \\ \sigma_2 \\ \sigma_3 \end{bmatrix}. \quad (4-9)$$

The stiffness matrix is more useful because one can simply input the stress field and get the corresponding strain without considering the Poisson's ratio.

By using stiffness matrix, the theoretical value of c-plane and a-plane Young's modulus can simply be derived by

$$\begin{aligned} E_{s,c-plane} &= S_{33}^{-1}, \\ E_{s,a-plane} &= S_{22}^{-1}. \end{aligned} \quad (4-10)$$

By reversing the matrix of elastic constant matrix, the reduced stiffness matrix of ZnO is shown below

$$\begin{bmatrix} \varepsilon_1 \\ \varepsilon_2 \\ \varepsilon_3 \end{bmatrix} = \begin{bmatrix} 0.0067 & -0.0046 & -0.0044 \\ -0.0046 & 0.0067 & -0.0044 \\ -0.0044 & -0.0044 & -0.0069 \end{bmatrix} \begin{bmatrix} \sigma_1 \\ \sigma_2 \\ \sigma_3 \end{bmatrix}. \quad (4-11)$$

The strain-stress ratio can simply be extracted by input uniaxial stress. The corresponding Young's modulus for c-plane and a-plane are 144 and 148 GPa, respectively. The estimation are in agreement with the literature values ($E_{c-plane} = 135 \pm 3$ GPa, $E_{a-plane} = 144 \pm 4$ GPa) [56, 95].

The yield stress can be extracted from $\sigma_{\max} = \tau_{\text{rss}} (\cos\theta\cos\phi)^{-1}$. The theoretical maximum shear stress is about one tenth of shear modulus. Under isotropic assumption, the theoretical value of shear modulus is:

$$G = \frac{C_{11} - C_{12}}{2} ,$$

$$\tau_{\max} = \frac{G}{10} . \quad (4-12)$$

The theoretical shear modulus and shear stress for ZnO are 40 and 4 GPa, respectively. A summary of ZnO theoretical and experimental results is listed in Table 13.

For GaN, the elastic constants are $C_{11} = 315$, $C_{12} = 118$, $C_{13} = 96$, $C_{33} = 324$, $C_{44} = 88$ and $C_{66} = 99$ [98]. The corresponding elastic constant matrix is shown below:

$$\begin{bmatrix} \sigma_1 \\ \sigma_2 \\ \sigma_3 \\ \sigma_4 \\ \sigma_5 \\ \sigma_6 \end{bmatrix} = \begin{bmatrix} 315 & 118 & 96 & 0 & 0 & 0 \\ 118 & 209.7 & 96 & 0 & 0 & 0 \\ 96 & 96 & 324 & 0 & 0 & 0 \\ 0 & 0 & 0 & 88 & 0 & 0 \\ 0 & 0 & 0 & 0 & 88 & 0 \\ 0 & 0 & 0 & 0 & 0 & 99 \end{bmatrix} \begin{bmatrix} \varepsilon_1 \\ \varepsilon_2 \\ \varepsilon_3 \\ \varepsilon_4 \\ \varepsilon_5 \\ \varepsilon_6 \end{bmatrix} . \quad (4-13)$$

The corresponding $E_{\text{c-plane}}$ and $E_{\text{a-plane}}$ are 281 and 341 GPa, respectively. The shear modulus and theoretic shear stress are 99 and 10 GPa, respectively. The corresponding stiffness matrix is shown below:

$$\begin{bmatrix} \varepsilon_1 \\ \varepsilon_2 \\ \varepsilon_3 \end{bmatrix} = \begin{bmatrix} 0.0029 & -0.0027 & -0.0027 \\ -0.0021 & 0.0029 & -0.0027 \\ -0.0027 & -0.0027 & 0.0036 \end{bmatrix} \begin{bmatrix} \sigma_1 \\ \sigma_2 \\ \sigma_3 \end{bmatrix} . \quad (4-14)$$

It should be noticed that the estimated Poisson ratio $\nu_{c\text{-plane}}$ (0.22) is not consistent with the literature value (0.35). The $\nu_{a\text{-plane}}$ is estimated to be 0.4. It should be remind that due to variety of measurement methods, growing conditions, substrate effects and growing conditions, there are still a large deviations between various reports (Table 14). In this study, we made the best estimation and used 0.35 and 0.4 as the Poisson ratios of the c-plane and a-plane GaN thin film, respectively. A summary of GaN theoretical and experimental results are listed in Table 15.

4.2. Nanoindentation testing

4.2.1. ZnO

The basic data on the ZnO wafer were obtained by the nanoindentation testing with the Berkovich tip under the XP system continuous stiffness measurement constant displacement rate mode. The displacement rates were set up to be 0.1 ~10 nm/s. No notable strain rate effect is found (E or H changing) within this range. For c-ZnO, the displacement rate is set to be 5 nm/s. Data are collected within the steady region. The indentation depth is set up to be 200 nm. The Poisson ratio is set to be 0.33. When the indentation depth is shallow, the nine parameters of area function can be reduced into two parameters. The area functions of two indentation tips with different radius which used in this study are shown below:

$$A_{R=100\mu m} = F(h_c) = 24.6h_c^2 + 649.1h_c, \quad (4-15)$$

$$A_{R=600\mu m} = F(h_c) = 22.8h_c^2 + 1352.88h_c.$$

Therefore, the relationship between the Young's modulus and indentation depth can be reduced as:

$$E_r = 0.072 \times \frac{(1 - \nu_s^2)}{h_c + 26.4h_c^{1/2}},$$

$$E_s = \left[\frac{E_r^{-1} - 0.995}{(1 - \nu_s)^2} \right]^{-1}, \quad (4-16)$$

where $E_{\text{tip}} = 1141$ GPa and $\nu_{\text{tip}} = 0.07$. In addition, the relationship between hardness and indentation depth can be derived as:

$$H = \frac{0.54E_s}{h_c^{1/2} + 26.4h_c^{-1/2}}. \quad (4-17)$$

The average E and H of the as-grown c-ZnO are 140 ± 7 GPa and 7.1 ± 0.4 GPa, respectively. Figure 53 shows the load-displacement curves of c-ZnO. The value is very close to the literature E value ~ 144 GPa [57]. The critical pop-in depth is ~ 20 nm. The average E and H of the annealed c-ZnO are 140 ± 9 GPa and 6.3 ± 0.3 GPa, respectively. The annealed c-ZnO wafer appeared to be softer.

The non-polar ZnO were examined by the nanoindentation testing with the Berkovich tip under the XP system continuous stiffness measurement constant displacement rate mode. The displacement rates were set up to be 0.1 \sim 10 nm/s. No notable strain rate effect is found (E or H changing) within this range. The Poisson ratio is setup to be 0.25. The average E and H of a-plane ZnO wafers are 150 ± 3 GPa

and 3.9 ± 0.2 GPa, respectively. The average E and H of the m-plane ZnO wafers are 147 ± 3 GPa and 4.0 ± 0.2 GPa, respectively.

To address the near surface analysis, the ZnO wafers are tested with the loading rate control mode by nanoindentation. The loading rates were set up to be 10^{-4} N/s. The goal load is set to be 3~10 mN. Based on over 20 indentations made on each specimen, the mean pop-in depth h_{crit} for as-grown and as-annealed ZnO (0001) was both around 20 nm. Taking tip contact radius ~ 100 nm, the relationship of critical pop-in load and indentation depth in this study is

$$P_{\text{pop-in}} = 133.3(E_s h_c^{3/2}) \quad (4-18)$$

The critical pop-in load P_{crit} is around 0.53 ± 0.15 mN (Figure 54). The maximum normal stress of nanoindentation in this study can be represented as:

$$\sigma_{\text{max}} = 9.26 \times 10^{-2} (E_s h_c^{1/2}) \quad (4-19)$$

The σ_{max} of c-plane ZnO is about 12 ± 1.0 GPa. The maximum shear stress as function as depth can be represented as

$$\tau_{\text{max}} = 2.85 \times 10^{-2} (E_s h_c^{1/2}) \quad (4-20)$$

The τ_{max} of c-plane ZnO is about 3.6 ± 0.3 GPa. Figure 55 reveals the representative nanoindentation load-displacement curves of the c-plane, a-plane, m-plane ZnO wafers and the curves predicted by the Hertzain contact theory. Based on over 10

indentations made on each specimen, the mean pop-in depth h_{crit} for the non-polar m-plane and a-plane ZnO wafer are around 33.0 and 21.5 nm. The corresponding maximum normal stress σ_y of the m-plane and a-plane ZnO wafers are 15.1 and 12.5 GPa, respectively.

4.2.2. GaN

The basic data on the GaN thin films were also extracted from nanoindentation with the Berkovich tip under the XP CSM constant displacement rate mode. The displacement rates were set up to be 0.005 ~ 1 nm/s. No notable strain rate effect of hardness and modulus is found within this range. For c-plane GaN, the displacement rate is set to be 1 nm/s. Data are collected within the steady region (200 - 400 nm) to avoid substrate effect (film thickness ~ 5 μm). The goal depth is set up to be 1000 nm. The Poisson ratio is set up to be 0.35. The average E and H of c-plane GaN are 272 ± 4 GPa and 15 ± 0.1 GPa, respectively. Figure 56 shows the load-displacement curve of c-GaN with the CSM constant displacement rate. The first pop-in is observed at depth $\sim 30.8 \pm 3.5$ nm (Figure 57). The corresponding maximum normal stress and a maximum shear stress are $\sigma_{\text{max}} = 29.8$ GPa and $\tau_{\text{max}} = 12.2$ GPa.

4.3. Microcompression testing

4.3.1. ZnO

The ZnO micropillars were milled by FIB system. Conducted layer Pt is coated on ZnO bulk for few nanometers in thickness to avoid the charging effect during milling process. The height and diameter of pillars are about 2 and 1 μm respectively.

The aspect ratio is about 2. The constant strain rate of this microcompression testing is set to be 2 nm/s, using the MTS nanoindentation system. The XP CSM H and E constant displacement rate mode are applied with the flat Berkovich with a triangle flat surface 14 μm on its edge. The Figure 58 represents the SEM images of the 1 μm as-grown pillar preset to 300 nm, the annealed pillar preset to 300 nm, as well as their associated stress-strain curves of microcompression testing.

The Young's modulus and flow stress of the tapered micropillars are corrected by a method suggested previously. To follow the mechanical response of the pillars, tests were interrupted at displacements of 300 nm, representing the fully plastic conditions. Since the micropillars are tapered at a small angle (specifically, 1.4° and 1.7° in the as-grown and annealed pillars, respectively). Taking $h_0 = 2 \mu\text{m}$ $d_0 = 1 \mu\text{m}$ and $\theta = 0.0262$ under consideration, the elastic modulus formula can be roughly corrected as:

$$E_{pillar} = 2.9 \times 10^{-3} \left(\frac{\delta P}{\delta h} \right), \quad (4-21)$$

where $(\delta P/\delta h)$ is the unloading part slope of load-displacement curve. Consequently, the corrected moduli of the as-grown and annealed micropillars are computed to be 123 ± 17 and 120 ± 15 GPa, respectively.

Particularly noted in Figure 58 is that there is an apparent strain burst occurring at load P. Taking pillar diameter = 1 μm under consideration, the corresponding normal yield stress of microcompression testing in this study is:

$$\sigma_{ys} = 1.27P. \quad (4-22)$$

The yield stress of as-grown c-plane ZnO pillar is 3 ± 0.5 GPa. With the calculated Schmidt factor of 0.41, the corresponding shear stress of pillar (τ_p) for the first strain burst in the deformed micropillar machined from the as-grown wafer to be $\sim 1.2 \pm 0.2$ GPa ($\tau_p = 0.41 \sigma_{ys}$). In parallel, the microcompression on the annealed sample shows σ_{ys} and τ_p of 2 ± 0.2 GPa and 0.8 ± 0.1 GPa, respectively.

The normal yield stress σ_{ys} of a-plane and m-plane ZnO wafer are 0.8 ± 0.04 GPa and 0.5 ± 0.02 GPa respectively. Comparing to c-plane, a-plane and m-plane have lower yield stresses, suggesting that the slip systems of both planes have lower Burgers' vector ($[10\bar{1}0]$ or $[2\bar{1}\bar{1}0]$) than c-plane $[\bar{1}011]$.

4.3.2. GaN

The GaN micropillars were milled by FIB system. Cu surface is coated on GaN by the Psur-100HB multi-target sputter with the 500 nm thickness for the indent tip alignment. The height and diameter of pillars are about 2 and 1 μm respectively. The aspect ratio is about 2. The constant strain rate is set to be 2 nm/s. The microcompression testing on GaN pillar are examined by MTS nanoindentation system. The XP CSM H and E constant displacement rate mode are also applied with the 14 μm flat Berkovich. Figure 59 represents the SEM images of the 1 μm as-FIB-milled pillar and the first strain burst micropillar, along with the load-displacement curves of microcompression. Figure 59 depicts the load-displacement and transformed engineering stress-strain curves of the compressed 1 μm micropillars at a strain rate of ~ 2 nm/s. There is an apparent strain burst occurring at 7.4 ± 1 mN in load. By using previous results, when the taper angle is small and

$\sin\theta \sim \theta$, the extracted elastic modulus E of 1 μm micropillars is $\sim 226 \pm 17$ GPa. And the engineering yield stress for the first strain burst is calculated to be $\sim 10 \pm 1$ GPa. Parallel compression tests were also conducted at $2\sim 0.02$ nm/s, there seems no significant influence from the strain rate over this range. Figure 60 and Figure 61 show the load displacement curve of non-polar plane a-plane and m-plane, respectively.

4.3.3. Raman spectrometer analyses

Figure 62 exhibits the back scattering Raman spectrum of the c-plane ZnO wafer. The shifting of E_2 peak can be indexed for characterizing the residual stress. Table 16 lists the main Raman spectra peaks position and FWHM of c-ZnO wafer. It is corresponding with the literature results (Table 17). No $A_{1(\text{LO})}$ peak is shown in ZnO film Raman spectrum. The appearance of $A_{1(\text{LO})}$ peak indicates the native point defects increase after FIB milling. Figure 63 shows the Raman spectra of the same ZnO film under four FIB processing condition. The spectra exhibit the increasing intensity of $A_{1(\text{LO})}$ peak, suggesting that the increasing of $A_{1(\text{LO})}$ peak intensity is caused by directly Ga ion implanted as well. Raman results show the E_2 peak center position of the as-grown pillar (438.6 cm^{-1} , Figure 64), preset 40 nm pillar (438.0 cm^{-1} , Figure 65) and the deformed pillar to a preset 300 nm displacement (438.2 cm^{-1} , Figure 66), essentially very similar to that of the free-standing ZnO wafer (438.6 cm^{-1}) with nil residual stress. This suggests that no apparent residual stress remains in the as-grown and as annealed wafers as well as the as-FIB-machined and deformed pillars.

The quality of GaN and ZnO single crystal can be identified by Raman spectrometer. For GaN, Figure 67 reveals the E_2 peak of GaN film located at 570.6 cm^{-1} with FWHM $\sim 2\text{ cm}^{-1}$. It is 3.6 cm^{-1} blue shifting compared with the literature

value of free standing GaN (568.0 cm^{-1}). After FIB milling, the E_2 peak of as-milled GaN pillar shifts to 567.6 cm^{-1} . It implies that most of the biaxial residual stress is released by the surface due to the high surface/volume ratio. The E_2 peak of preset 100 nm pillar (before strain burst) and preset 200 nm pillar (after strain burst) are 567.5 cm^{-1} and 567 cm^{-1} which is very similar to as-grown micropillars (567.6 cm^{-1}) or free standing GaN. Table 18 reveals the measurement of Raman E_2 peak position, FWHM and estimating residual stress of GaN films and micropillars.

The FWHM of E_2 peak and intensity of $A_{1(\text{LO})}$ reveal the quality of GaN film and micropillars. The narrow FWHM indicates the perfect crystalline quality, and the broadening implies the accumulated of crystal defects. As for the as-grown GaN film and as-milled GaN pillars, the FWHM is around 2.0 to 2.5 cm^{-1} , reflecting the low defects content in these two cases. After microcompression testing, the FWHM increases significantly to 5.7 cm^{-1} and 6.2 cm^{-1} . It means that even though GaN pillar has high surface/volume ratio to release most of the residual stress, the large defects accumulated still after compression even before the strain burst. In addition, the quasi-longitudinal optic phonon peak of pillars (QLO) at 732 cm^{-1} is seen to be the consequence of combination of $A_{1(\text{LO})}$ (727 cm^{-1}) and $E_{1(\text{LO})}$ (735 cm^{-1}) of c-plane GaN film. Due to the distortion of crystalline structure, the incident laser beam slightly deviates from the [0001] back scattering direction. The degradation of crystal quality and distortion of structure observations are consistent with the results of XTEM results.

4.4. SEM observations

The morphology of semiconductors is analyzed by using SEM secondary electron

(SEI) images. Figure 68 represents the SEM images of the 1 μm as-milled c-plane ZnO micropillar. The SEM SEI of deformed m-plane ZnO pillar and a-plane ZnO pillar are shown in Figure 69 and Figure 70, respectively. The cleavages are found at the surface of non-polar planes. Suggesting the slight deviation between the stress axis and a-axis as well as m-axis induced the slightly slip along basal plane. The further detail of microcompression deformation mechanism of non-polar plane will be studied by XTEM (Figure 71). Figure 72 represents the SEM images of the 1 μm as-milled c-GaN pillar and deformed c-GaN pillar. Figure 72(b) indicates the trace of main slip plane and some fringes which causes by other slip systems. The results of EBSD and XTEM confirmed the domain slip plane is the pyramidal plane. Figure 71 exhibits the process of fabricating XTEM sample. Firstly we used FIB to mark the direction of cross section plane (Figure 71(a)), then deposited the carbon to cover the pillar as a protection layer (Figure 71(b)), finally used ultra-fine beam to mill the HR-XTEM specimen (Figure 71(c)). Figure 73(a) reveals the rough surface morphology of r-plane GaN thin film. The cross section SEM images confirmed the thickness of thin film (Figure 73(b)). The SEM image shows a sharp top on the as-milled r-GaN micropillar (Figure 73(c)), suggesting there are other preferred orientations which have higher etching rate than r-plane.

4.5. XTEM analyses

A cross-sectional TEM micrograph of the deformed c-plane ZnO as-grown pillar is shown in Figure 74, with an image zone axis of $[10\bar{1}0]$. It reveals that the sample shears along a plane that forms a 62° angle with respect to the (0001) basal plane, or $\varphi=28^\circ$ with respect to the loading c-axis. For hexagonal systems, the angle θ between the plane $(h_1 k_1 l_1)$ and plane $(h_2 k_2 l_2)$ may be found from the following equation:

$$\theta = \cos^{-1} \left[\frac{h_1 h_2 + k_1 k_2 + \frac{1}{2} (h_1 k_2 + h_2 k_1) + \frac{3a^2}{4c^2} l_1 l_2}{\sqrt{\left(h_1^2 + k_1^2 + h_1 k_1 + \frac{3a^2}{4c^2} l_1^2 \right) \left(h_2^2 + k_2^2 + h_2 k_2 + \frac{3a^2}{4c^2} l_2^2 \right)}} \right], \quad (4-23)$$

where a and c are the lattice constants. This slip plane can be easily indexed to be $(10\bar{1}1)$.

XTEM characterization has been done on the nanoindentation mark, as-deposited and the compressed micropillar of c -plane GaN thin film. In the as-deposited GaN film, there is minimum defect with clean image. As shown in Figure 75(c), the longitudinal section of the compressed GaN micropillar reveals massive dislocation slip traces on the pyramidal planes $(10\bar{1}1)$, oriented at an acute angle of $\sim 62^\circ$ to the basal plane (0001) . Figure 76 reveals the XTEM bright film images and diffraction pattern of c -plane GaN thin film after indented at load 200 mN. The bright field image shows fringes on both basal and pyramidal planes which consistent with previous finding.

4.6. Cathodoluminescence analysis

Samples were investigated by using CL spectroscopy (step 1 nm per second) for studying the optoelectronic properties. Figure 77 and Figure 78 present the CL spectra of c -plane GaN thin film and c -plane ZnO wafer respectively. The ZnO has UV/BL (~ 3.3 eV), YL (~ 2.6 eV) and RL (1.6 eV). The GaN thin film has larger band gap (~ 3.4 eV) than bulk ZnO (~ 3.3 eV). The GaN thin film has UV/BL (~ 3.4 eV), YL

(~2.2 eV) and RL (1.7 eV). The results are consistent with the literature value. To exclude the artificial deviation from focusing, just-focus and over-focus plane CL spectra are compared in Figure 79. The BL peak position of just-focus as-grown ZnO wafer locates at wavelength 374.5 nm (3.3 eV). Only intensity changing is found. No detectable shifting is found after changing focal plane. The following intensity comparisons are examined at the same focal plane.

In this study, it was investigated the possible surface damage by Ga ions using CL spectroscopy. The sample were scanned after being Ga ion beam machined and sample with additional annealing at 800°C in air for 1 h to reduce the surface damage by Ga ions. Figure 80 reveals the CL spectra of as-grown and annealed ZnO wafers and the corresponding SEM SEI images. The spectra at the outer crater (30 kV, 6.4 nA Ga ion implantation for 1 min) at room temperature. The blue luminescence (BL) peak of the as-grown and annealed wafers located at 383 nm (3.2 eV) and 382 nm (3.2 eV), respectively. For comparison, the intensity of the BL peak increased ~1.5 times after annealing process. The CL images of 383 nm wavelength reveal the increasing of bright area after annealing process. Both results indicate the refinement of crystal quality and decreasing of defects density after the thermal treatment, consistent with previous results.

To invest the luminescence changing before/after microcompression testing, m-plane ZnO wafer, preset 50, 300 and 400 nm pillars were examined by CL monochromater (Figure 81). Preset 50 nm and 300 nm pillars represent the pillar deformed within elastic and plastic region respectively. The BL peak of as-grown m-plane wafer is 373 nm (3.3 eV). After FIB milling, the BL peak red shifts to 375 nm. No peak shifting is observed after the yielding point.

To investigate the luminescence changes in more detail, the cross-sectional CL (X-CL) spectra of the deformed c-plane ZnO pillar are shown in Figure 82. The BL peak of the outer crater is red-shifted to 421 nm, but the BL peak blue-shifts back from the bottom (418 nm) to the top (400 nm) of the pillar. The corresponding SEM SEI image is shown in Figure 82 as well. The CL behavior of the as-FIB-machined and deformed pillars reveals noticeable changes, which mechanism will be studied in detail in the future.

Chapter 5. Discussion

5.1. Low dimensional stress comparison

5.1.1. Theoretical and experimental results

Table 13 and Table 15 are the theoretical and experimental results of ZnO and GaN, respectively. The extracted Poisson ratio from c-plane ZnO elastic constants is coincided with the literature value. But the Poisson ratio of c-plane GaN (0.2) is lower than the literature one (0.35). The difference might be due to the deviation from different measuring methods, such as ultrasonic measurement, surface Brillouin scattering, acoustic investigation technique, polarized Brillouin scattering, ultrasonic resonance method, atomistic calculations based on an inter-atomic pair potential within the shell-model approach and calculated using ab initio periodic linear combination of the atomic orbital method.

Although there are some reports of nanoindentation testing on non-polar plane ZnO/GaN, we did not find any related study about the Poisson ratio of a-plane or m-plane. Since the Poisson ratio can possibly affects large deviation (about 10~20%) of the modulus and hardness. Poisson ratio might be one of the reasons to explain why there are large deviations in nano-scaled measurements of single crystal ZnO/GaN. We firstly report the theoretical Poisson ratio of the a-plane hexagonal wurzite structure. With the proper values of Poisson ratios, the experimental modulus and shear stress of c-plane ZnO and GaN are coincided for the theoretical and literature values.

5.1.2. Nanoindentation testing

Figure 53 and Figure 56 reveal the nanoindentation load-displacement curves of c-plane ZnO and GaN, respectively. Only multiple pop-in effect is found in the loading curve. No pop-out (the suddenly drawback of strain) or elbow (the slope changing of strain) is found in the unloading curve. Suggest that dislocation sliding dominates the deformation mechanism, nor phase transformation or twinning deformation. The XTEM results also confirmed that no crack, phase transformation or twinning occurred in all specimens.

Multiple pop-in effect is found in the loading part of the load-displacement curve on both materials. Suggesting the multiple slip systems are activated while increasing the indentation load. The first critical pop-in (depth <50 nm) is seen as the theoretical yielding point of high quality single crystal. For c-plane hexagonal wurzite structure, only pyramidal plane was activated. There is another larger pop-in found at depth 100~200 nm. Suggesting massive slip systems are activated then.

The XTEM images of GaN thin film (Figure 76) confirmed the conjecture. Both basal plane and pyramidal plane slip systems were activated under high stress. As the load increasing, the slip plane progressed and finally crossed together. A jog was then created. When dislocations slipped to a jog, more energy is needed to initiate the dislocation climbing. Dislocations were stock at the jog and created a stress field which lead other dislocation became harder to approach. The deeper slip systems were then activated. The CL image of UV band also confirmed this explanation. The Rosette pattern represented two slip system $\{10\bar{1}1\}$ and $\{2\bar{1}\bar{1}1\}$. It only shows after

the massive pop-in happened. In a recent study of the mechanical properties of c-plane ZnO single crystal, Jian [99] also reported the observation of massive $\{10\bar{1}1\}$ pyramidal slip, in addition to the basal slip, during nanoindentation testing.

The theoretical maximum shear stress can be estimated by shear modulus. The τ_{\max} is equivalent to $\mu/10$, where μ (~40 GPa) is the shear modulus calculated with the isotropic assumption [59]. The experimental shear stress can be estimated by fitting the critical pop-in depth into Hertzian contact theory. The experimental values of both c-plane ZnO/GaN are very close to the theoretical values (Table 13 and Table 15). We consider the near surface region (depth <50 nm) of high quality single crystal semiconductor has no oxide layer and can be viewed as a defect-free zone. That this maximum shear stress τ_{\max} extracted from the early stage of nanoindentation is already close to the theoretical shear stress level [60]. Meanwhile, the maximum normal stress σ_{\max} is at about $R/2$, where R is the contact radius. By multiply maximum shear stress to Schmid factor, we could estimate the theoretical yield stress.

5.1.3. Microcompression testing

The similar phenomena were observed in microcompression testing. Figure 58 to Figure 61 show the load-displacement curves of microcompression testing on ZnO/GaN micropillars. A main strain burst is found at the top of the loading curve. No pop-out or elbow is found in the unloading curve. The results indicate the dislocation sliding dominated the deformation mechanism of microcompression testing. Figure 75 exhibits the XTEM bright field image of preset 200 nm GaN pillar. The slip plane is traced by the massive slip dislocations. It oriented at the acute angle of $\sim 62^\circ$ to the

basal plane (0001). The domain slip plane is identified to be the pyramidal plane $\{10\bar{1}1\}$.

The selected area diffraction pattern (Figure 75(b)) shows there is a small distortion angle at the top of the pillars after the microcompression testing. The small bending angle causes the deviation from ideal back scattering laser incident direction [0001] and turns into near forward scattering. Figure 77 reveals the XTEM (0001) plane central dark field image of same pillar. The dark region on the top of the pillar shows the bending region. The slightly distortion might be caused by slightly misalignment from the [0001] c-axis. It is the reason why Raman spectrum shows the $A_{1(LO)}$ and $E_{1(LO)}$ peaks are combined into QLO peak and the appearance of $E_{1(TO)}$ peak which should be forbidden according to the selection rule from group theory. Both XTEM and Raman spectrum reveal no recrystallization or phase transformation after microcompression testing on GaN thin film. Closer examinations of the SEM micrographs of GaN/ZnO (Figure 68 to Figure 72), there are fringes other than the main slip plane. The results of SEM observation and Raman spectrum analysis reveal that other slip systems might also have activated in the later stage of deformation, as indicated by the non-parallel surface slip traces. These evidences can explain the small pop-in step of load-displacement curve at the early stage.

It is known that the presence of residual stresses can degrade the luminescence of ZnO. According to the Raman spectra, the E_2 peak position and FWHM of the as-grown wafer and the machined pillar is 438 cm^{-1} and 9 cm^{-1} , respectively. It agrees well with the literature data for high quality ZnO wafers. No significant shifting was observed after microcompression testing, suggesting that there is no significant residual stress in the as-grown wafer, as-milled and deformed micropillars.

Microcompression testing did not induce additional residual stresses. This is probably because induced stress during compression is accommodated by plastic deformation and also fully released upon unloading (Figure 62 to Figure 67). Similar results were obtained in GaN thin films and pillars (Figure 67).

5.1.4. Low dimensional measurements

The results of c-plane ZnO microcompression testing ($E_{\text{microcompression}} = 123 \text{ GPa}$) are compared with that measured from nanoindentation ($E_{\text{nanoindentation}} = 147 \text{ GPa}$) and calculated theoretic value ($E_{\text{theoretical}} = 140 \text{ GPa}$). Comparing with the value from elastic constant and nanoindentation data, the lower elastic modulus of microcompression is due to the high surface/volume ratio erased the small volume constrain effect. The semiconductors appeared to have higher mechanical properties in the nano-scaled than micro-scaled measurements. Comparing the critical shear stresses of theory ($\tau_{\text{theoretical}} = 4 \text{ GPa}$), nanoindentation ($\tau_{\text{nanoindentation}} = 3.6 \text{ GPa}$) and microcompression testing ($\tau_{\text{microcompression}} = 1.2 \text{ GPa}$), they show the same tendency. The micro-scaled shear stress is smaller than other two.

In macro scaled testing, nucleation of dislocations can occur homogeneously in the bulk as full dislocation loops, or occur heterogeneously at surfaces and edges as half or quarter dislocation loops. In nanoindentation testing, the stress state is non-uniform and the resolved shear stress on potential slip systems reaches a maximum in regions directly underneath the contact. Therefore, dislocation nucleation is expected to occur inside the solid. In micropillar compression testing, on the other hand, the stress field is in principle uniform and dislocation nucleation can occur anywhere within the gauge section, including at the free surfaces and edges. This

stress-state difference is crucial in understanding the deformation behaviors and the relevant mechanisms deduced from nanoindentation or micropillar compression tests. Suggesting micropillars contain more defects and the erased of small volume constrain effect.

The other interesting topic is the size effect. Although there is still lack of solid explanation of the deviation of mechanical properties between different examining scaled, methods and geometry, the Young's modulus seems to be affected by geometry size effect in nano-scaled. The c-plane ZnO with different geometry and methods have been reported, such as our study compression testing on micropillars ($E \sim 120$ GPa), nanoindentation testing on nano-rods ($E \sim 63$ GPa), bending testing on nano-belts ($E \sim 31$ GPa) and tension testing on nano-wires ($E \sim 21$ GPa). Since the nano-scaled geometry can induced the quantum confinement effect which can improve the luminescence performance, the mechanical properties of nano-scaled semiconductors with different geometry shape are needed and meaningful.

5.2. Deformation mechanisms

Since the luminescence performance will be affected seriously by defects and the main deformation mechanism is dominated by dislocation, it is important to know when the deformation will be initiated. The deformation will be activated when the shear stress exceed the critical resolved shear stress (CRSS). The CRSS can be estimated by timing normal stress to the largest Schmid factor. For c-plane hexagonal wurzite structure, As for the favorable slip plane, we have confirm the preferred slip plane is the pyramidal plane $\{10\bar{1}1\}$. But for the favorable slip directions, there could be many possible choices, such as $[\bar{2}112]$, $[\bar{2}113]$, or $[\bar{1}011]$. Although high Schmid

factor lead the larger shear stress, we still have to consider the Burger's vector. The activation energy increases with increasing Burger's vector. Taking all considerations for the higher resulting Schmid factor ($= \cos\phi\cos\lambda$, where λ is the angle between the slip direction and loading c-axis) and lower Burgers' vector, the most possible slip system should be $\langle \bar{1}011 \rangle \{10\bar{1}1\}$, and the Schmid factor is calculated to be 0.41 for uniaxial [0001] stress.

5.3. Thermal treatment effects

Annealing process did not affect the young's modulus, yield stress or critical shear stress of nanoindentation testing. This is expected since the young's modulus is an intrinsic property. The measured high resolved shear stress at first pop-in corresponds to the homogeneous nucleation of dislocations in a perfect ZnO single crystal [53]. The critical shear stress and the corresponding yield stress are extracted within the defect free region which is already approaching the theoretical level.

For microcompression testing, thermal treatment did not affect the young's modulus. Again, this is expected since the young's modulus is an intrinsic property. But the yield stress and critical shear stress is about 70% of the as-milled micropillars from the annealed pillar. Since the dislocation densities in both the as-grown and annealed samples are low, the reduction is probably not caused by dislocation-related mechanisms. The Raman spectra analysis excluded the effect of thermal expansion coefficient difference induced residual stress. The improved CL intensity in Figure 79 in the annealed wafer was apparently due to the reduction of defect density not residual stress. From the fact that the CL signal/noise ratio was enhanced by annealing, the decrease in yield strength might also be attributable to the reduction of defect

density after thermal treatment.

5.4. Polarity effects

Since the morphology of non-polar GaN thin films are still rocky. The comparisons between the polar and non-polar plane are only focused on the ZnO wafers. With the estimated Poisson ratio of a-plane ZnO, the experimental Young's modulus of a-plane $E = 150 \pm 3$ GPa is very close to the theoretic value $E = 148$ GPa and literature value $E = 144 \pm 4$ GPa (Table 19 [56, 60, 70]). The theoretical estimation of m-plane Poisson ratio is still not clear. Assuming m-plane has more similar character with a-plane than c-plane, $\nu_{a\text{-plane}} = 0.4$ is set as the Poisson ratio of m-plane. The Young's modulus of m-plane is then to be $E = 150$ GPa. There is not much different in Young's modulus between three planes. But by comparing the hardness of the polar and non-polar ZnO wafers, non-polar ZnO wafers seems to be softer. The hardness shows is about 55% of the c-plane ZnO wafer from the a-plane ZnO wafer.

5.5. Hexagonal and cubic structure influence

The similar microcompression testing experimental procedure of InP is included to compare within different structures. Jian et al. [110] experimentally studied the deformation behaviors of single-crystal (100)-plane-oriented InP pillars under uniaxial compression. InP has the face-centered cubic (zincblende) crystal structure. For the sample preparation, the InP micro-pillars were prepared using the same FIB experimental process. But the implantation induced amorphous layer in InP (~50 nm) is larger than GaN (3 nm) or ZnO (~15 nm). The milling rates of FIB system also

indicate that cubic structure is easier to be etched by Ga ion. Note that the etching rate of InP by FIB is about five times than GaN or ZnO, suggesting InP is more likely to be damaged. The damage layer can be refined and vaporized by thermal treatment.

5.5.1. Elasticity

Furthermore, another approximate formula is used for extracting the Young's modulus of the pillar (E_{pillar}) is employed to obtain the Young's modulus of the present InP pillars by assuming that the applied stresses are uniformly distributed over the entire cross-section of the pillar as following:

$$E_{pillar} = \left(1 + \frac{\pi D(1-\nu)}{8H}\right) \left[\frac{4PH}{\pi D(D + 2H \tan \theta)d} \right], \quad (5-1)$$

where ν , P , d , H , D , and θ are denoted as the Poisson's ratio of sample, the compressive load applied on the pillar, the total displacement of pillar upon compression, the height of pillar, the top diameter of pillar, and the taper angle, respectively. In this study we used

$$E_{pillar} = \left(\frac{P}{\Delta h} \right) \left[\frac{\ln \left(1 + \frac{2h\theta}{d} \right)}{2\pi d \theta} \right], \quad (5-2)$$

where $\left(\frac{P}{\Delta h} \right)$ can be found from the slope of loading load-displacement curves, d is the diameter of pillar, h is the height of pillar and θ is the taper angle. The anisotropy is considered in first formula which is more precise to estimate the Young's modulus

of microcompression testing on different planes. The Young's modulus of InP pillars is estimated to be approximately 73 GPa, which is in good agreement with the values obtained by nanoindentation, namely 82 GPa. The same tendency of small volume constrain effect is shown in InP as well. The extracted Young's modulus shows about 90% of the nanoindentation testing from the micropillar testing.

5.5.2. Deformation mechanisms

The deformation mechanisms of zincblende cubic structure and hexagonal wurzite structure are different. Even the zincblende cubic structure has different deformation mechanism between different semiconductors. Four semiconductors are compared in deformation mechanism of microcompression testing, GaAs (zincblende, face center cubic), InP (zincblende, face centered cubic), GaN (wurzite, hexagonal) and ZnO (wurzite, hexagonal).

For GaAs, the XTEM investigations on micropillars have indicated that significant dislocation slips on $\{111\}$ planes, high density twins as well as microcracks were generated during the microcompression testing. Therefore, it was suggested that the deformation behaviors of GaAs micro-pillars might have involved different combinations of the above mentioned activities at various deformation stages.

For InP, the compressions exerted along the $[100]$ direction, the Schmid factor for the $\{111\}\langle 110\rangle$ slip system is calculated to be about 0.41. Under the assumption of a perfectly uniaxial stress throughout the InP pillar, the resolved shear stress (τ_{RSS}) on the $\{111\}$ planes becomes ~ 1 GPa ($2.5 \text{ GPa} \times 0.41$), which is substantially smaller than

the critical resolved shear stress ($\tau_{\text{crss}} = 2.8 \sim 3.5$ GPa) for activating dislocation slip in nanoindentation testing. The extracted shear stress shows about only 30% of the nanoindentation testing from the micropillar testing. Thus, is consistent with twin dominated deformation behavior. Similar behavior has been observed in GaAs by Androussi et al. [111]. It was pointed out that, for face-centered cubic structured semiconductors under the high-stress compression condition, the micro-twinning produced by gliding of partial dislocations might become the dominant plastic deformation mechanism over the gliding of perfect dislocations. This suggests that twinning deformation becomes the dominated deformation mechanism of the InP micropillars.

It is thus interesting to explore the underlying mechanism that could lead to the apparent differences between the present observations and previous results. In compression tests carried out under MTS XP CSM displacement control mode, similar strain burst behaviors have been observed in the micropillars made of hexagonal close packed GaN and ZnO as well as the face centered cubic InP when the applied load exceeds the yield strength. For all the InP, GaN, and ZnO micropillars, inhomogeneous deformation has occurred. A closer look at the SEM photograph indicates that this inhomogeneous deformation may have been resulted from the slip bands asymmetrically localized in the gauge range of the deformed pillars. Nevertheless, it is worthwhile to indicate here that although the τ_{crss} values for the hexagonal structured c-plane GaN (4.1 GPa) and ZnO (1.2 GPa) are even higher than those of their fcc counterparts, InP (1 GPa) and GaAs (0.7 GPa), the deformation characteristics were predominantly associated with dislocation activities. The reason for this is not clear at present and certainly requires further studies. A detailed comparison of the deformation characteristics with the prominent mechanical

parameters collected from the literature for the above-mentioned compound semiconductors is displayed in Table 20 [54, 60].

5.5.3. Deformation energy analysis

The last section is the point of view on deformation energy which had been used on analyzing the twinning density of deformed InP micropillar. Since the ZnO and GaN micropillar only need to take dislocation sliding under consideration. With the help of XTEM and microcompression testing, the deformation energy can possibly be used for estimating the density of dislocation after compressed. Furthermore, to quantize the dislocation induced luminescence degradation.

For InP micropillars, the strong intensity of the twin spots in the selected area diffraction pattern indicates that the density of the stress-induced twins can be very high. The diffraction spots of the twins are slightly elongated because the twins are essentially consisting of very thin crystalline plates owing to the explosive generation of twins that eventually leads to the drastic strain burst observed. In addition, there is no indication of the formation of cracks or other phases, thus, the deformation behavior in the present case seems to proceed predominantly by the formation and propagation of twins. To give a simple estimation on the number of twins, the energies before and after a twin has traversed the pillar at an angle of 54.7° are compared. Thus, the formation energy (E_f) of a twin in the pillar is approximated by

$$E_f = (\cos \theta) \cdot (\pi r^2) \cdot \Gamma, \quad (5-3)$$

where r is the radius of pillar and Γ is the energy per unit area of twin, respectively. Taking $\Gamma = 1.8 \times 10^{-2} \text{ J/m}^2$, the number of twins formed can be estimated from the complete release of elastic strain energy. From the elastic strain energy is estimated to be around $1.7 \times 10^{10} \text{ J}$. Assuming this elastic strain energy is solely related to the formation of twins, we obtain that the number of twins generated by this process is approximately 2×10^3 . A higher number of 6×10^3 twins are obtained if the total dissipation energy (i.e., the entire area between the loading and unloading curves is taken into account for the formation of twins. Such estimation provides the upper limit of the number of twins can be generated within a micro-scale pillar.

Chapter 6. Conclusions

Nanoindentation, microcompression, X-ray diffraction, EBSD, Raman spectroscopy and cathodoluminescence spectroscopy tests are conducted on wurtzite semiconductors. Based on the results, the following conclusions are drawn:

1. The quality of GaN thin films and ZnO wafers are identified by X-ray diffraction and Raman spectrometer. The narrow FWHM of rocking curve and E_2 peak of Raman spectrometer implies the fine quality of samples.
2. The theoretical values of GaN epilayers and ZnO wafers are calculated in this study. For ZnO, the theoretical Poisson ratio are $\nu_{th, c-axis} = 0.33$ and $\nu_{th, a-axis} = 0.25$, the theoretical Young's modulus are $E_{th, c-plane}$ and $E_{th, a-plane}$ are 144 and 148 GPa respectively. The theoretical shear modulus and stress are $G_{th} = 40$ and $\tau_{th} = 4$ GPa. For GaN, the theoretical Poisson ratio are $\nu_{th, c-axis} = 0.25$ and $\nu_{th, a-axis} = 0.4$, the theoretical Young's modulus are $E_{th, c-plane}$ and $E_{th, a-plane}$ are 281 and 341 GPa respectively. The theoretical shear modulus and stress are $G_{th} = 99$ and $\tau_{th} = 10$ GPa. The estimated values are coincided with the literature value and experimental results, but the theoretical Poisson ratio of c-plane GaN (0.25) is different with the literature value (0.35). In this study, we choice 0.35 as the Poisson ratio of c-plane GaN thin film. The experimental values of ZnO/GaN coincide to the literature values. Table 13 and Table 15 list the comparison of theoretical and experimental results.

3. Taking all considerations for the higher resulting Schmid factor and lower Burgers' vector. The most possible slip system for c-plane hexagonal structure under [0001] stress should be $(10\bar{1}1)[\bar{1}011]$, and the Schmid factor is calculated to be 0.41.

4. Polar plane c-ZnO wafers are tested by nanoindentation system with CSM mode at strain rate from $1 \times 10^{-2} \text{ s}^{-1}$ to $1 \times 10^{-4} \text{ s}^{-1}$. No significant mechanical properties changing are found within this range. The E of as-grown and annealed ZnO is $E_{\text{as-grown}} = 140 \pm 7 \text{ GPa}$ and $E_{\text{annealed}} = 140 \pm 9 \text{ GPa}$. To address the near surface analysis, the c-plane ZnO wafers are tested with LRC mode by nanoindentation system. The mean pop-in depth h_{crit} for as-grown and as-annealed c-plane ZnO was both around 20 nm, the corresponding maximum normal stress and a maximum shear stress are $\sigma_{\text{max}} = 12 \pm 1.0 \text{ GPa}$ and $\tau_{\text{max}} = 3.6 \pm 0.3 \text{ GPa}$. The maximum shear stress is equivalent to $\mu/10$. The experimental τ_{max} is close to the theoretical shear stress level. Annealing process did not affect the young's modulus and maximum shear stress. This is expected since the near surface region can be seen as defect free zone for high quality single crystal. The Young's modulus and theoretical shear stress is an intrinsic property which will not be affected

5. For nanoindentation testing, the H of as-grown and annealed c-ZnO is $H_{\text{annealed}} = 6.3 \pm 0.3 \text{ GPa}$ and $H_{\text{as-grown}} = 7.1 \pm 0.4 \text{ GPa}$. For microcompression testing, the normal yield stress σ_{ys} of as-grown and annealed c-ZnO micropillar are $3 \pm 0.5 \text{ GPa}$ and $2 \pm 0.2 \text{ GPa}$ respectively. Both results reveal the annealed c-ZnO wafer appeared to be softer. Since the dislocation densities in both the as-grown and annealed samples are low, the reduction is probably not caused by

dislocation-related mechanisms. From the fact that the CL signal/noise ratio was enhanced by annealing, the decrease in yield strength might also be attributable to the reduction of defect density after thermal treatment.

6. 1 μm GaN and ZnO micropillars are fabricated successfully from the GaN thin film and ZnO wafer by using the focus ion beam. Samples are measured by microcompression testing at the strain rate range from $1 \times 10^{-2} \text{ s}^{-1}$ to $1 \times 10^{-4} \text{ s}^{-1}$. No significant influence from strain rate in this range is observed. The E of GaN and ZnO pillar are $226 \pm 17 \text{ GPa}$ and $123 \pm 17 \text{ GPa}$ respectively. Compared with the evaluated yield stress value from nanoindentation data, the higher value of elastic modulus and yield stress is due to the small volume constrain effect. The semiconductors appeared to have higher mechanical properties in the nanoscale than microscale measurements.
7. The E_2 peak of Raman spectrometer exhibits high residual compression stress ($\sim 1.5 \text{ GPa}$) constrain in the c-GaN thin film. Due to the high surface/volume ratio of pillar, nil residual stress remains in the GaN pillar after the FIB milling process. Even after yielding point, nil residual stress remains in the c-GaN pillar. No residual stress is detected in ZnO wafer.
8. The Raman spectra indicate a slightly distortion after microcompression testing. The $A_{1(\text{LO})}$ and $E_{1(\text{LO})}$ peaks combined into QLO peak which locate between them. Due to the back scattering incident laser beam deviate from the ideal $[0001]$ direction. The XTEM result implies the same results as Raman spectrometer. The massive dislocations leave the trace on pyramidal plane and are seen on bright field images. There is few degree of slightly distortion on the top of the pillar.

9. The FIB induced Ga ion implanted can be recovered by thermal treatment. The direct implantation reduced the intensity of CL spectrum. After annealing at 900°C for 1 hour, the S/N ratio of the BL peak increased ~1.5 times. Results indicate the refinement of crystal quality and decreasing of defects density after the thermal treatment, consistent with previous results.

10. The XCL specimen is fabricated successfully from the c-ZnO wafer by using the focus ion beam. The planar and cross section CL analysis of micropillar reveal the BL peak red shift after FIB milling process.

Chapter 7. Prospective and future work

In order to extend the present study, some future research directions of the mechanical optoelectronic behaviors on wide band gap semiconductors are suggested as follows:

1. The nano- and micro-scaled mechanical response of tension testing is still lack in this field. Since there are various micro- and nano-scaled applications and devices, a better understanding of the mechanical characteristics is necessary and meaningful.
2. High residual compression stress usually constrain in the hetero-epilayer thin film. The research of residual stress induced mechanical and optoelectronic response is still lacking. A systematic investigation of residual stress is meaningful and needed.
3. The luminescence performance is seriously affected by defects. For better understanding of defects type and corresponding response, low temperature Raman, cathodoluminescence and photoluminescence spectroscopy can suppress the heat disturbance and look into the detail of optoelectronic properties.

References

- [1] S. Gradecak, F. Qian, Y. Li, H. G. Park and C. M. Lieber, *Appl. Phys. Lett.*, 87 (2005) 173111.
- [2] J. C. Johnson, H. J. Choi, K. P. Knutsen, R. D. Schaller, P. D. Yang and R. J. Saykally, *Nature Mater.*, 1 (2002) 106.
- [3] H. Amano, I. Akasaki, K. Hiramatsu, N. Koide and N. Sawaki, *Thin Solid Films*, 163 (1988) 415.
- [4] I. Akasaki, H. Amano, Y. Koide, K. Hiramatsu and N. Sawaki, *J. Cryst. Growth*, 98 (1989) 209.
- [5] H. Amano, M. Kito, K. Hiramatsu and I. Akasaki, *J. J. Appl. Phys. Lett.*, 28 (1989) L2112.
- [6] H. Amano, N. Sawaki, I. Akasaki and Y. Toyoda, *Appl. Phys. Lett.*, 48 (1986) 353.
- [7] S. Nakamura, *J. J. Appl. Phys. Lett.*, 30 (1991) L1705.
- [8] S. Nakamura, T. Mukai, M. Senoh and N. Iwasa, *J. J. Appl. Phys. Lett.*, 31 (1992) L139.
- [9] S. Hasegawa, S. Nishida, T. Yamashita and H. Asahi, *J. Ceramic Proc. Res.*, 6 (2005) 245.
- [10] C. H. Hong, D. Pavlidis, K. Hong and K. Wang, *Mater. Sci. and Eng. B-Solid State Mater. for Adv. Tech.*, 32 (1995) 69.
- [11] H. Morkoc, S. Strite, G.B. Gao, M. E. Lin, B. Sverdlov and M. Burns, *J. Appl. Phys.*, 76 (1994) 1363.
- [12] J. Narayan, K. Dovidenko, A. K. Sharma and S. Oktyabrsky, *J. Appl. Phys.*, 84 (1998) 2597.

- [13] F. M. Morales, D. Gonzalez, J. G. Lozano, R. Garcia, S. Hauguth-Frank, V. Lebedev, V. Cimalla and O. Ambacher, *Acta Mater.*, 57 (2009) 5681.
- [14] S. R. Jian, G. J. Chen, J. S. C. Jang and Y. S. Lai, *J. Alloy Compd.*, 494 (2010) 219.
- [15] H. Lahreche, P. Vennegues, M. Vaille, B. Beaumont, M. Laugt, P. Lorenzini and P. Gibart, *Semi. Sci. and Tech.*, 14 (1999) L33.
- [16] U. Ozgur, Y. I. Alivov, C. Liu, A. Teke, M. A. Reshchikov, S. Dogan, V. Avrutin, S. J. Cho and H. Morkoc, *J. Appl. Phys.*, 98 (2005) 041301.
- [17] Y. Z. Zhu, G. D. Chen, H. G. Ye, A. Walsh, C. Y. Moon and S. H. Wei, *Phys. Rev. B*, 77 (2008) 245209.
- [18] Fujita In., Kyoto Japan, <http://www.iic.kyoto-u.ac.jp/sozo/fujita/>.
- [19] J. Michler, K. Wasmer, S. Meier, F. Ostlund and K. Leifer, *Appl. Phys. Lett.*, 90 (2007) 043123.
- [20] C. H. Chien, S. R. Jian, C. T. Wang, J. Y. Juang, J. C. Huang and Y. S. Lai, *J. of Phys. D-Appl. Phys.*, 40 (2007) 3985.
- [21] H. Zhang, B. E. Schuster, Q. Wei and K. T. Ramesh, *Scr. Mater.*, 54 (2006) 181.
- [22] P. Waltereit, O. Brandt, A. Trampert, H. T. Grahn, J. Menniger, M. Ramsteiner, M. Reiche and K. H. Ploog, *Nature*, 406 (2000) 865.
- [23] S. Ghosh, P. Waltereit, O. Brandt, H. T. Grahn and K. H. Ploog, *Phys. Rev. B*, 65 (2002) 075202.
- [24] P. Misra, O. Brandt, H. T. Grahn, H. Teisseyre, M. Siekacz, C. Skierbiszewski and B. Lucznik, *Appl. Phys. Lett.*, 91 (2007) 141903.
- [25] T. Flissikowski, O. Brandt, P. Misra and H. T. Rahn, *J. Appl. Phys.*, 104 (2008) 063507.
- [26] R. Navamathavan, Y. T. Moon, G. S. Kim, T. G. Lee, J. H. Hahn and S. J. Park, *Mater. Chem. and Phys.*, 99 (2006) 410.

- [27] X. J. Ning, F. R. Chien, P. Pirouz, J. W. Yang and M. A. Khan, *J. Mater. Res.*, 11 (1996) 580.
- [28] B. N. Sverdlov, G. A. Martin, H. Morkoc and D. J. Smith, *Appl. Phys. Lett.*, 67 (1995) 2063.
- [29] A. J. Slifka, B. J. Filla and J. M. Phelps, *J. of Res. of the Natl. In. of Stand. and Tech.*, 103 (1998) 357.
- [30] S. J. Pearton, D. P. Norton, K. Ip, Y. W. Heo and T. Steiner, *Prog. in Mater. Sci.*, 50 (2005) 293.
- [31] Y. Dikme, G. Gerstenbrandt, A. Alam, H. Kalisch, A. Szymakowski, M. Fieger, R. H. Jansen, M. Heuken, *J. Cryst. Growth*, 248 (2003) 578.
- [32] D. M. Follstaedt, J. Han, P. Provencio and J. G. Fleming, *Mrs Inter. J. of Nitride Semi. Res.*, 4 (1999) art. no.-G3.72.
- [33] K. Y. Zang, L. S. Wang, S. J. Chua and C. V. Thompson, *J. Cryst. Growth*, 268 (2004) 515.
- [34] J. Bai, T. Wang, P. J. Parbrook, K. B. Lee and A. G. Cullis, *J. Cryst. Growth*, 282 (2005) 290.
- [35] I. Ahmad, M. Holtz, N. N. Faleev and H. Temkin, *J. Appl. Phys.*, 95 (2004) 1692.
- [36] H. J. Ko, Y. F. Chen, Z. Zhu, T. Hanada and T. Yao, *J. Cryst. Growth*, 208 (2000) 389.
- [37] R. J. Lad, P. D. Funkenbusch and C. R. Aita, *J. of Vac. Sci. & Tech.*, 17 (1980) 808.
- [38] W. C. Shih and M. S. Wu, *J. Cryst. Growth*, 137 (1994) 319.
- [39] D. K. Hwang, K. H. Bang, M. C. Jeong and J. M. Myoung, *J. Cryst. Growth*, 254 (2003) 449.
- [40] A. Ohtomo, K. Tamura, K. Saikusa, K. Takahashi, T. Makino, Y. Segawa and H.

- Koinuma, M. Kawasaki, Appl. Phys. Lett., 75 (1999) 2635.
- [41] R. D. Vispute, V. Talyansky, S. Choopun, R. P. Sharma, T. Venkatesan, M. He, X. Tang, J. B. Halpern, M. G. Spencer, Y. X. Li, L. G. Salamanca-Riba, A. A. Iliadis and K. A. Jones, Appl. Phys. Lett., 73 (1998) 348.
- [42] S. Yoshida, S. Misawa, S. Gonda, J. of Vac. Sci. Tech. B, 1 (1983) 250.
- [43] M. J. Paisley, Z. Sitar, J. B. Posthill, R. F. Davis, J. of Vac. Sci. Tech. A Vac. Surfaces and Films, 7 (1989) 701.
- [44] S. Strite, J. Ruan, Z. Li, A. Salvador, H. Chen, D. J. Smith, W. J. Choyke and H. Morkoc, J. of Vac. Sci. & Tech. B, 9 (1991) 1924.
- [45] T. Lei, M. Fanciulli, R. J. Molnar, T. D. Moustakas and R. J. Graham, J. Scanlon, Appl. Phys. Lett., 59 (1991) 944.
- [46] Y. F. Chen, D. M. Bagnall, H. J. Koh, K. T. Park, K. Hiraga, Z. Q. Zhu and T. Yao, J. Appl. Phys., 84 (1998) 3912.
- [47] H. P. Maruska and J. J. Tietjen, Appl. Phys. Lett., 15 (1969) 327.
- [48] S. Nakamura, Y. Harada and M. Seno, Appl. Phys. Lett., 58 (1991) 2021.
- [49] G. Springholz, N. Frank and G. Bauer, Thin Solid Films, 267 (1995) 15.
- [50] A. G. Thompson, Mater. Lett., 30 (1997) 255.
- [51] R. Abbaschian, L. Abbaschian and R. E. Hill, *Physical Metallurgy Principles*, CL Engineering, Boston (2009) 142.
- [52] W. C. Oliver and G. M. Pharr, J. Mater. Res., 7 (1992) 1564.
- [53] W. G. Mao, Y. G. Shen and C. Lu, J. Eur. Ceram. Soc., 31 (2011) 1865.
- [54] T. H. Sung, J. C. Huang, J. H. Hsu and S. R. Jian, Appl. Phys. Lett., 97 (2010) 171904.
- [55] Z. Takkouk, N. Brihi, K. Guergouri and Y. Marfaing, Phys. B-Condensed Matt., 366 (2005) 185.
- [56] S. Basu and M. W. Barsoum, J. Mater. Res., 22 (2007) 2470.

- [57] J. E. Bradby, S. O. Kucheyev, J. S. Williams, C. Jagadish, M. V. Swain, P. Munroe and M. R. Phillips, *Appl. Phys. Lett.*, 80 (2002) 4537.
- [58] K. L. Johnson, *Contact Mechanics*, Cambridge University Press, UK Cambridge, (1985).
- [59] I. R. Shein, V. S. Kiiko, Y. N. Makurin, M. A. Gorbunova and A. L. Ivanovskii, *Phys. Solid State*, 49 (2007) 1067.
- [60] T. H. Sung, J. C. Huang, J. H. Hsu, S. R. Jian and T. G. Nieh, *Appl. Phys. Lett.*, 100 (2012) 211903.
- [61] M. D. Uchic, D. M. Dimiduk, J. N. Florando and W. D. Nix, *Science*, 305 (2004) 986.
- [62] M. D. Uchic and D. A. Dimiduk, *Mater. Sci. Eng. A*, 400 (2005) 268.
- [63] K. J. Hemker and W. N. Sharpe, *Annual Review of Mater. Res.*, 37 (2007) 93.
- [64] D. M. Dimiduk, M. D. Uchic and T. A. Parthasarathy, *Acta Mater.*, 53 (2005) 4065.
- [65] J. R. Greer, W. C. Oliver and W. D. Nix, *Acta Mater.*, 53 (2005) 1821.
- [66] C. A. Volkert and E. T. Lilleodden, *Phil. Mag.*, 86 (2006) 5567.
- [67] M. D. Uchic, D. M. Dimiduk, R. Wheeler, P. A. Shade and H. L. Fraser, *Scr. Mater.*, 54 (2006) 759.
- [68] B. E. Schuster, Q. Wei, H. Zhang and K. T. Ramesh, *Appl. Phys. Lett.*, 88 (2006) 103112.
- [69] H. Bei, S. Shim, E. P. George, M. K. Miller, E. G. Herbert and G. M. Pharr, *Scr. Mater.*, 57 (2007) 397.
- [70] V. A. Coleman, H. H. Tan, C. Jagadish, S. O. Kucheyev and J. Zou, *Appl. Phys. Lett.*, 87 (2005) 231912.
- [71] T. S. Jeong, M. S. Han, J. H. Kim, C. J. Youn, Y. R. Ryu and H. W. White, *J. Cryst. Growth*, 275 (2005) 541.

- [72] M. A. Reshchikov and H. Morkoc, *J. Appl. Phys.*, 97 (2005) 061301.
- [73] F. Tuomisto, K. Saarinen, D. C. Look and G. C. Farlow, *Phys. Rev. B*, 72 (2005) 085206.
- [74] S. Limpijumnong, C.G. Van de Walle, *Phys. Rev. B*, 69 (2004) 035207.
- [75] Z. Q. Chen, A. Kawasuso, Y. Xu, H. Naramoto, X. L. Yuan, T. Sekiguchi, R. Suzuki and T. Ohdaira, *J. Appl. Phys.*, 97 (2005) 013528.
- [76] A. Audren, A. Hallen, M. K. Linnarsson and G. Possnert, *Nucl. Instrum. Meth. in Phys. Res.*, 268 (2010) 1842.
- [77] X. W. Ke, F. K. Shan, Y. S. Park, Y. J. Wang, W. Z. Zhang, T. W. Kang and D. J. Fu, *Surf. Coat. Technol.*, 201 (2007) 6797.
- [78] M. Peres, J. Wang, M. J. Soares, A. Neves, T. Monteiro, E. Rita, U. Wahl and J. G. Correia, E. Alves, *Superlattices and Microstructures*, 36 (2004) 747.
- [79] E. Schlenker, A. Bakin, H. Schmid, W. Mader, S. Sievers, M. Albrecht, C. Ronning, S. Muller, M. Al-Suleiman, B. Postels, H. H. Wehmann, U. Siegner and A. Waag, *Nanotechnology*, 18 (2007) 125609.
- [80] K. Lorenz, E. Alves, E. Wendler, O. Bilani, W. Wesch and M. Hayes, *Appl. Phys. Lett.*, 87 (2005) 191904.
- [81] J. C. Yang, H. G. Na, M. A. Kebede, H. S. Kim and H. W. Kim, *J. Cryst. Growth*, 312 (2010) 1199.
- [82] C. A. Arguello, D. L. Rousseau and S. P. S. Porto, *Physical Review*, 181 (1969) 1351.
- [83] T. Suski, P. Perlin, H. Teisseyre, M. Leszczynski, I. Grzegory, J. Jun, M. Bockowski, S. Porowski and T. D. Moustakas, *Appl. Phys. Lett.*, 67 (1995) 2188.
- [84] L. Bergman, M. Dutta, C. Balkas, R. F. Davis, J. A. Christman, D. Alexson and R. J. Nemanich, *J. Appl. Phys.*, 85 (1999) 3535.
- [85] I. D. Wolf, *Soc. Sci. Tech.*, 11 (1996) 139.

- [86] C. R. Das, S. Dhara, H. C. Hsu, L. C. Chen, Y. R. Jeng, A. K. Bhaduri, B. Raj, K. H. Chen and S. K. Albert, *J. of Raman Spectrosc.*, 40 (2009) 1881.
- [87] T. Azuhata, T. Sota, K. Suzuki and S. Nakamura, *J. Phys.-Condes. Matter*, 7 (1995) L129.
- [88] S. H. Margueron, P. Bourson, S. Gautier, A. Soltani, D. Troadec, J. C. De Jaeger, A. A. Sirenko and A. Ougazzaden, *J. Cryst. Growth*, 310 (2008) 5321.
- [89] C. Kisielowski, J. Kruger, S. Ruvimov, T. Suski, J. W. Ager, E. Jones, Z. L. Weber, M. Rubin, E. R. Weber, M. D. Bremser and R. F. Davis, *Phys. Rev. B*, 54 (1996) 17745.
- [90] P. Puech, F. Demangeot, J. Frandon, C. Pinquier, M. Kuball, V. Domnich and Y. Gogotsi, *J. Appl. Phys.*, 96 (2004) 2853.
- [91] S. R. Jian, I. J. Teng and J. M. Lu, *Nanoscale Res. Lett.*, 3 (2008) 158.
- [92] V. A. Coleman, J. E. Bradby, C. Jagadish and M. R. Phillips, *Appl. Phys. Lett.*, 89 (2006) 3.
- [93] M. A. Reshchikov, H. Morkoc, S. S. Park and K. Y. Lee, *Appl. Phys. Lett.*, 78 (2001) 3041.
- [94] S. O. Kucheyev, J. E. Bradby, J. S. Williams, C. Jagadish and M. V. Swain, *Appl. Phys. Lett.*, 80 (2002) 956.
- [95] V. A. Coleman, J. E. Bradby, C. Jagadish, P. Munroe, Y. W. Heo, S. J. Pearton, D. P. Norton, M. Inoue and M. Yano, *Appl. Phys. Lett.*, 86 (2005) 3.
- [96] MTI In., <http://mtixtl.com>.
- [97] R. M. Langford and A. K. Petford-Long, *J. Vac. Sci. Techn. Intl. J. Dev. Vac.*, 19 (2001) 2186.
- [98] V. Y. Davydov, Y. E. Kitaev, I. N. Goncharuk, A. N. Smirnov, J. Graul, O. Semchinova, D. Uffmann, M. B. Smirnov, A. P. Mirgorodsky and R. A. Evarestov, *Phys. Rev. B*, 58 (1998) 12899.

- [99] S. R. Jian, *J. Alloy. Compd.*, 494 (2010) 214.
- [100] H. Ni and X. D. Li, *Nanotechnology*, 17 (2006) 3591.
- [101] X. D. Yan, M. Dickinson, J. P. Schirer, C. W. Zou and W. Gao, *J. Appl. Phys.*, 108 (2010) 056101.
- [102] A. V. Desai and M. A. Haque, *Sens. Act. A Phys.*, 134 (2007) 169.
- [103] F. Xu, Q. Q. Qin, A. Mishra, Y. Gu and Y. Zhu, *Nano Res.*, 3 (2010) 271.
- [104] X. D. Bai, P. X. Gao, Z. L. Wang and E. G. Wang, *Appl. Phys. Lett.*, 82 (2003) 4806.
- [105] L. J. Ming, Master thesis, National SunYat-Sen University, (2006).
- [106] D. S. Huang, Master thesis, National SunYat-Sen University, (2008).
- [107] B. Rafferty and L. M. Brown, *Phys. Rev. B*, 58 (1998) p. 10326.
- [108] J. E. Ayers, *Heteroepitaxy of Semiconductors*, CRC Press, Boca Raton, (2006) 105.
- [109] H. O. Pierson, *Handbook of Chemical Vapor Deposition*, Noyes Publications, N. J., Norwich, NY, (1999) 20.
- [110] S. R. Jian, T. H. Sung, J. C. Huang and J. Y. Juang, *Appl. Phys. Lett.*, 101 (2012) 151905.
- [111] Y. Androussi, G. Vanderschaeve and A. Lefebvre, *Philos. Mag. A* 59 (1989) 1189.

Table 1 Fundamental properties of III-V group semiconductors [11].

	GaN		AlN		InN	
Structure	Wurtzite	Zinc blende	Wurtzite	Zinc blende	Wurtzite	Zinc blende
Band gap energy (eV)	3.4	3.3	6.2	5.1	1.9	2.2
Lattice constants a-axis (Å)	3.189	4.52	3.112	4.38	3.548	4.98
Lattice constants c-axis (Å)	5.185	-	4.982	-	5.76	-
c/a ratio	1.626	-	1.601	-	1.623	-
Thermal expansion $\Delta a/a$ (10^{-6} K)	5.59	-	4.2	-	4	-
Thermal expansion $\Delta c/c$ (10^{-7} K)	3.17	-	5.3	-	3	-
Thermal conductivity (W/m-K)	130	-	200	-	80	-

Table 2 The mechanical properties of polycrystalline ZnO, single crystallize ZnO wafer, thin films, nanowires, nanobelts measured by different testing techniques [59, 94, 100].

	Structure	Method	E	H	Slip system	Ref.
			(GPa)	(GPa)		
Poly crystal	Bulk	Calculation	120	-	-	[59]
		Experiment	140	-	-	[59]
Single crystal	Bulk	Calculation	140	-	-	[59]
Nanorod		Nanoindentation	111	5	Pyramidal	[57]
			112	5.4	Pyramidal	[99]
			140	7.1	-	[60]
Nanowire		Tension	63	9.7	-	[101]
Nanobelt			Bending	21	-	-
		160		-	-	[103]
Micropillar		Microcompression	31.1	2.5	-	[100]
			51	-	-	[104]
				123	-	Pyramidal

Table 3 The plane abbreviation and polarity of two semiconductors which used in this thesis.

Material	Polarity	Plane
ZnO	Polar	c-plane (0001)
	Non-polar	m-plane ($10\bar{1}0$)
	Non-polar	a-plane ($2\bar{1}\bar{1}0$)
GaN	Polar	c-plane (0001)
	Semi polar	r-plane ($1\bar{1}02$)

Table 4 Comparison of the relevant III-V nitride material properties with perspective substrate materials [11, 29, 30].

Substrate material	Lattice parameters (Å)	Thermal conductivity (W/m-K)	Coefficients of thermal expansion (K ⁻¹)
GaN	a = 3.189	130	5.59x10 ⁻⁶
	c = 5.185		3.17x10 ⁻⁶
AlN	a = 3.112	200	4.2x10 ⁻⁶
	c = 4.982		5.3x10 ⁻⁶
Sapphire	a = 4.758	50	7.5x10 ⁻⁶
	c = 12.99		8.5x10 ⁻⁶
ZnO	a = 3.252	100	2.9x10 ⁻⁶
	c = 5.213		4.75x10 ⁻⁶
MgO	a = 4.216	30	10.5x10 ⁻⁶
Si	a = 5.430	150	3.59x10 ⁻⁶
GaAs	a = 5.653	50	6.00x10 ⁻⁶

Table 5 Structure, lattice constant, space group and density of five different LAO phases [89, 105].

Name	Crystal structure	Lattice constant				Space Group	Density (g/cm^3)
		a(A)	b(A)	c(A)	Angle		
α - LiAlO_2	Hexagonal	2.799		14.180		$\bar{R}3_m$	3.413
β - LiAlO_2	Orthorhombic	5.280	6.300	4.900		Pna21	2.686
β - LiAlO_2	Monoclinic	8.147	7.941	6.303	$93^\circ 18'$		2.600
γ - LiAlO_2	Tetragonal	5.172		6.284		P4212	2.605
δ - LiAlO_2	Cubic	12.650				I4132	2.600

Table 6 Lattice mismatch and thermal expansion coefficient between (200) γ -LAO and GaN [90, 106].

Plane	Direction	Mismatch	Thermal expansion
$(10\bar{1}0)$ GaN	$[0001]$ GaN $[010]$ LAO	0.62%	-25%
	$[1\bar{2}10]$ GaN $[001]$ LAO	-0.65%	
	$[0001]$ GaN $[010]$ LAO	0.3%	-25%
	$[1\bar{2}10]$ GaN $[001]$ LAO	1.7%	
	$[1\bar{2}10]$ GaN $[010]$ LAO	9.08%	-25%
	$[0001]$ GaN $[001]$ LAO	22.19%	
(0001) GaN	$[1\bar{2}10]$ GaN $[010]$ LAO	9.08%	
	$[10\bar{1}0]$ GaN $[001]$ LAO	14.72%	
	$[10\bar{1}0]$ GaN $[010]$ LAO	-5.53%	
	$[1\bar{2}10]$ GaN $[001]$ LAO	-0.65%	

Table 7 Lattice parameters of a number of the prospective substrate materials for ZnO [16].

Material	Crystal structure	Lattice parameters (Å)	Lattice Mismatch (%)	Thermal-expansion (K ⁻¹)
ZnO	Hexagonal	a = 3.252	-	$\alpha_a = 2.9 \times 10^{-6}$
		c = 5.213		$\alpha_c = 4.75 \times 10^{-6}$
GaN	Hexagonal	a = 3.189	1.8	$\alpha_a = 5.17 \times 10^{-6}$
		c = 5.185		$\alpha_c = 4.55 \times 10^{-6}$
AlN	Hexagonal	a = 3.112	4.5	$\alpha_a = 5.3 \times 10^{-6}$
		c = 4.980		$\alpha_c = 4.2 \times 10^{-6}$
α -Al ₂ O ₃	Hexagonal	a = 4.757	(18.4% after 30° in-plane rotation)	$\alpha_a = 7.3 \times 10^{-6}$
		c = 12.983		$\alpha_c = 8.1 \times 10^{-6}$
6H-SiC	Hexagonal	a = 3.080	3.5	$\alpha_a = 4.2 \times 10^{-6}$
		c = 15.117		$\alpha_c = 4.68 \times 10^{-6}$
Si	Cubic	a = 5.430	40.1	$\alpha_a = 3.59 \times 10^{-6}$
ScAlMgO ₄	Hexagonal	a = 3.246	0.09	-
		c = 25.195		
GaAs	Cubic	a = 5.652	42.4	$\alpha_a = 6.0 \times 10^{-6}$

Table 8 The ZnO elastic constants extracted from different methods: (a) ultrasonic measurement, (b) surface Brillouin scattering, (c) acoustic investigation technique, (d) polarized Brillouin scattering, (e) ultrasonic resonance method, (f) calculated using LDA, (g) calculated using GGA (h) atomistic calculations based on an inter-atomic pair potential within the shell-model approach and (i) calculated using ab initio periodic linear combination of the atomic orbital method [16].

Method	(a)	(b)	(c)	(d)	(e)	(f)	(g)	(h)	(i)
C_{11} (GPa)	209.7	206	157	190	207	209	230	231	246
C_{12} (GPa)	121.1	117	89	110	117.7	85	82	111	127
C_{13} (GPa)	105.1	118	83	90	106.1	95	64	104	105
C_{33} (GPa)	210.9	211	208	196	209.5	270	247	183	246
C_{44} (GPa)	42.47	44.3	38	39	44.8	46	75	72	56
C_{66} (GPa)	44.29	44.6	34	40	44.6	62	-	60	115

Table 9 Hardness and Young's modulus of GaN from different kinds of indentation methods [20, 91].

	GaN thin film	H (GPa)	E (GPa)	Indentation tip
Drovy et al.	As-grown	12 ± 2	287	Vickers
Nowak et al.	As-grown	20	295	Spherical
Kucheyev et al.	As-grown	13.4	233	Spherical
	Ion-damaged	15.1	164	
	Ion-damaged	15.1	164	
	Amorphized	2.4	65	
Jain et al.	As-grown	19.34 ± 2.13	314.93 ± 40.58	Berkovich
	Si-doped	20.12 ± 2.51	247.16 ± 14.89	
Kavouras et al.	As-grown	13.67 ± 0.13		Knoop
	O-doped	14.74 ± 0.22		
	Mg-doped	16.87 ± 0.13		
	Au-doped	12.16 ± 0.09		
	Xe-doped	11.35 ± 0.12		
	Ar-Doped	9.98 ± 0.14		
Chien et al.	As-grown	19.31 ± 1.05	286.12 ± 25.34	Berkovich

Table 10 List of main luminescence lines and bands in GaN [72].

Maximum position (eV)	Nomenclature	Doping	Comments
3.478	FE, X_A	Undoped	
3.471	DBE, D^0X_A	Undoped, Si	A few close lines
3.466	ABE, A^0X_A	Undoped, Mg	Best FWHM <0.1 meV
3.44–3.46	TES	Undoped	Plethora of lines
3.455	ABE	Zn	A weaker peak at 3.39 eV
3.45–3.46	Y_1	Undoped	Correlates with inversion domains
3.41–3.42	Y_2	Undoped	
3.397		Be	e-A type
3.387	FE-LO	Undoped	
3.38	DBE-LO	Undoped	
3.38		Be	DAP type
3.37–3.38	Y_3		Undoped
3.375	ABE-LO	Undoped	
3.364	ABE-LO	Zn	
3.35–3.36	Y_4	Undoped	
3.34	Y_5	Undoped	
3.30–3.32	Y_6	Undoped	
3.295	FE-2LO	Undoped	
3.288	DBE-2LO	Undoped	
3.283	ABE-2LO	Undoped	
3.28	UVL	Undoped	e-A type
3.272	ABE-2LO	Zn	
3.27	DBE		DBE in cubic GaN
3.26	UVL	Undoped, Si	DAP type
3.1–3.26	UVL	Mg	e-A and DAP
3.21–3.23	Y_7	Undoped	
3.16			Shallow DAP in cubic GaN
3.08	Y_8	Undoped	
3.08		C	In cubic GaN
3.0–3.05	BL	C	Broad
2.9–3.0	BL	Undoped, Fe	Broad, unstable intensity
2.9	BL	P	Broad, with fine structure
2.88	BL	Undoped	Broad, with fine structure
2.88	BL	Zn	Broad, with fine structure
2.86	Y_9	Undoped	
2.8	Y_{10}	Undoped	
2.8	BL	Cd	Broad, with fine structure
2.7–2.8	BL	Mg	Broad, large shifts
2.6–2.8	BL	Undoped	Broad, surface related
2.68	Y_{11}	Undoped	
2.6	GL	As	Broad, with fine structure
2.6	GL	Zn	Broad
2.56	AL	Undoped	Broad
2.51	GL3	Undoped	Broad
2.5		Ca	Broad
2.4–2.5		Mg-O	Broad
2.48	GL	Undoped	Broad
2.43		Hg	Broad
2.36	GL2	Undoped	Broad
2.2–2.3	YL	Undoped, C	Broad
1.9–2.1		C	Broad, in cubic GaN
1.8–2.0	RL	Undoped	Broad
1.85	RL2	Undoped	Broad
1.8		Zn	Broad
1.7–1.8		Mg	Broad
1.66		Undoped	Broad
1.64		C	Broad
1.3		(Fe)	Sharp
1.27		Mn	Broad
1.193		(Ti,Cr)?	Sharp
0.95		Undoped	Sharp, irradiation induced
0.85–0.88		Undoped	Sharp, irradiation induced

Table 11 Valance and ionic radii of candidate dopant atoms [30].

Atom	Valence	Radius (Å)
Zn	2+	0.6
Li	1+	0.59
Ag	1+	1.00
Ga	3+	0.47
Al	3+	0.39
In	3+	0.62
O	2-	1.38
N	3-	1.46
P	3-	2.12
As	3-	2.22
F	1-	1.31

Table 12 Migration barriers for native defects in Wurtzite GaN [74].

Defect	Charge state	Barrier (eV)
Ga _f	3+	0.9
	2+	≤ 0.9
	1+	≤ 0.9
N _f	3+	1.4
	2+	2.5
	1+	2.1
	0	2.4
	1-	1.6
V _N	3+	2.6
	1+	4.3
V _{Ga}	3-	1.9

Table 13 Comparison of the theoretical and experimental mechanical properties of ZnO.

ZnO	c-plane		a-plane	
	Theoretical	Experimental	Theoretical	Experimental
Poisson's ratio	0.33	0.33	0.25	-
Young's modulus (GPa)	144	140	148	150
Shear modulus (GPa)	40	-	-	-
Yield stress (GPa)	10	12	-	13
Shear stress (GPa)	4	3.6	-	-

Table 14 The elastic constants and estimated mechanical properties of GaN by different group [108].

C_{11} (GPa)	296	315	353	390	370	373
C_{12} (GPa)	120	118	135	145	145	141
C_{13} (GPa)	158	96	104	106	110	80.4
C_{33} (GPa)	267	324	367	398	390	387
$E_{c\text{-plane}}$ (GPa)	147	281	323	123	343	362
$E_{a\text{-plane}}$ (GPa)	242	341	381	105	395	422
$V_{c\text{-plane}}$	0.38	0.22	0.21	0.20	0.21	0.16
$V_{a\text{-plane}}$	0.49	0.40	0.38	0.38	0.36	0.31
S (GPa)	2×10^{-5}	8×10^{-6}	6×10^{-6}	5×10^{-6}	6×10^{-6}	5×10^{-6}
G (GPa)	88	99	109	123	113	109
τ_{theo} (GPa)	9	10	11	12	11	11
Ref.	Savastenko et al.	Davydov et al.	Ayer et al.	Polian et al.	Deger et al.	Deguchi et al.

Table 15 Comparison of the theoretical and experimental mechanical properties of GaN.

GaN	c-plane		a-plane
	Theoretical	Experimental	Theoretical
Poisson's ratio	0.22	0.35	0.4
Young's modulus (GPa)	281	272	341
Shear modulus (GPa)	99	-	-
Yield stress (GPa)	-	29.8	-
Shear stress (GPa)	10	12.2	-

Table 16 The Raman spectra peak position and FWHM of bulk ZnO.

	Film	Pillar	Preset 40 nm	Preset 300 nm
Lorentzian multipeak fitting (cm ⁻¹)				
A _{1(TO)}	331.6	332.0	329.2	331.4
FWHM	13.9	19.8	17.1	12.5
E ₂	438.6	438.0	438.2	438.2
FWHM	4.9	6.0	6.0	6.4
A _{1(LO)}		549.0	551.1	538.9
FWHM		77.3	70.5	88.9
E _{1(LO)}		576.8	578.9	576.7
FWHM		18.2	19.2	21.7

Table 17 The fundamental optical modes of the Wurtzite crystal (frequency expressed in cm^{-1}) [82].

Mode (cm^{-1})	BeO	ZnO	CdS (25 K)	ZnS (298 K)	ZnS (25 K)
E_2	338	101	43	55	-
E_2	684	444	256	724	280
$A_{1(\text{TO})}$	678	380	234	274	280
Quasi- $A_{1(\text{TO})}$	700	395	240	274	280
Quasi- $E_{1(\text{TO})}$	702	398	239	274	280
$E_{1(\text{TO})}$	722	413	243	274	280
$A_{1(\text{LO})}$	1081	579	205	352	356
Quasi- $A_{1(\text{LO})}$	1088	585	306	352	356
Quasi- $E_{1(\text{LO})}$	1089	585	306	352	356
$E_{1(\text{LO})}$	1097	591	307	352	356

Table 18 The measurement of Raman E_2 peak position and FWHM of GaN films and micropillars [54].

	E_2 peak (cm^{-1})	E_2 FWHM (cm^{-1})	Residual stress (MPa)
Free standing GaN	567.0	-	0
As-deposited film	570.6	2.1	-1508
As-FIB-milled pillar	567.7	2.6	-280
Pillar compressed to preset 100 nm	567.5	5.7	-198
Pillar compressed to preset 200 nm	567.0	6.2	24

Table 19 Young's modulus measured from different kinds of indentation methods [56, 60, 70].

	Sung et al. [60]	Basu et al. [56]	Coleman et al. [70]	Coleman et al. [70]
Specimen type	Wafer	Wafer	Wafer	Thin film
Indenter tip	Berkovich	Spherical	Spherical	Spherical
c-plane modulus (GPa)	140	135 ± 3	163 ± 6	318 ± 50
a-plane modulus (GPa)	150	144 ± 4	143 ± 6	310 ± 40

Table 20 Comparison of the crystal structure, mechanical data, and dominant deformation modes in the four optoelectronic materials [54, 60, 110].

	InP	GaAs	ZnO	GaN
Crystal structure	Cubic	Cubic	Hexagonal	Hexagonal
Horizontal plane	(100)	(100)	(0001)	(0001)
E (GPa)	74	123	123	226
Hardness (GPa)	5	8	7	15
Yield stress (GPa)	2.5	1.8	3	10
$\tau_{\text{microcompression}}$ (GPa)	1	0.7	1.2	4.1
$\tau_{\text{nanoindentation}}$ (GPa)	2.8–3.5	4.1–5.2	3.2–4.4	7.6–9.4
Deformation mode	Twinning	Twinning	Dislocation	Dislocation
Shear plane	(111)	(111)	(10 $\bar{1}$ 1)	(10 $\bar{1}$ 1)

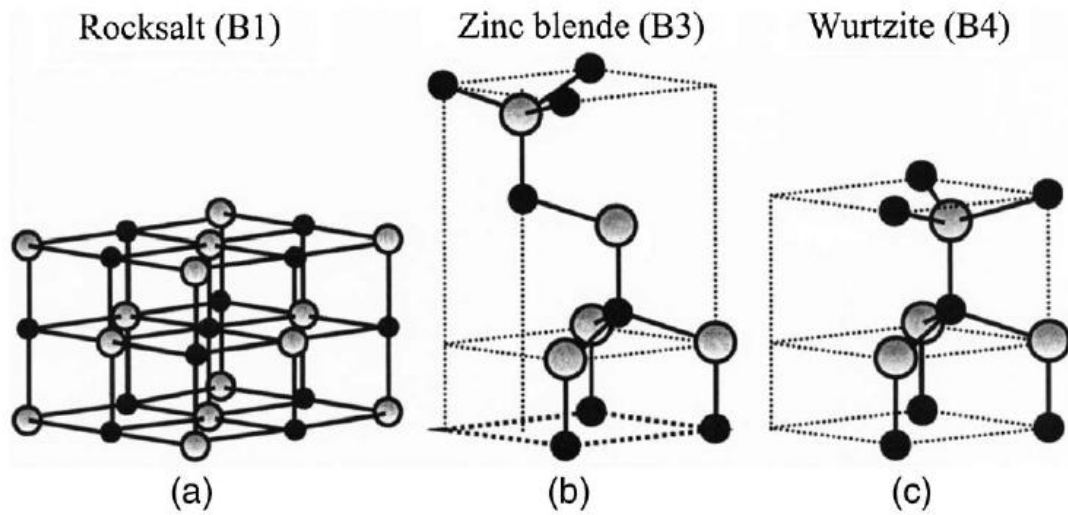


Figure 1 Three structure types of II-IV group binary compound (a) Rocksalt (b) Zincblende (c) Wurtzite [16].

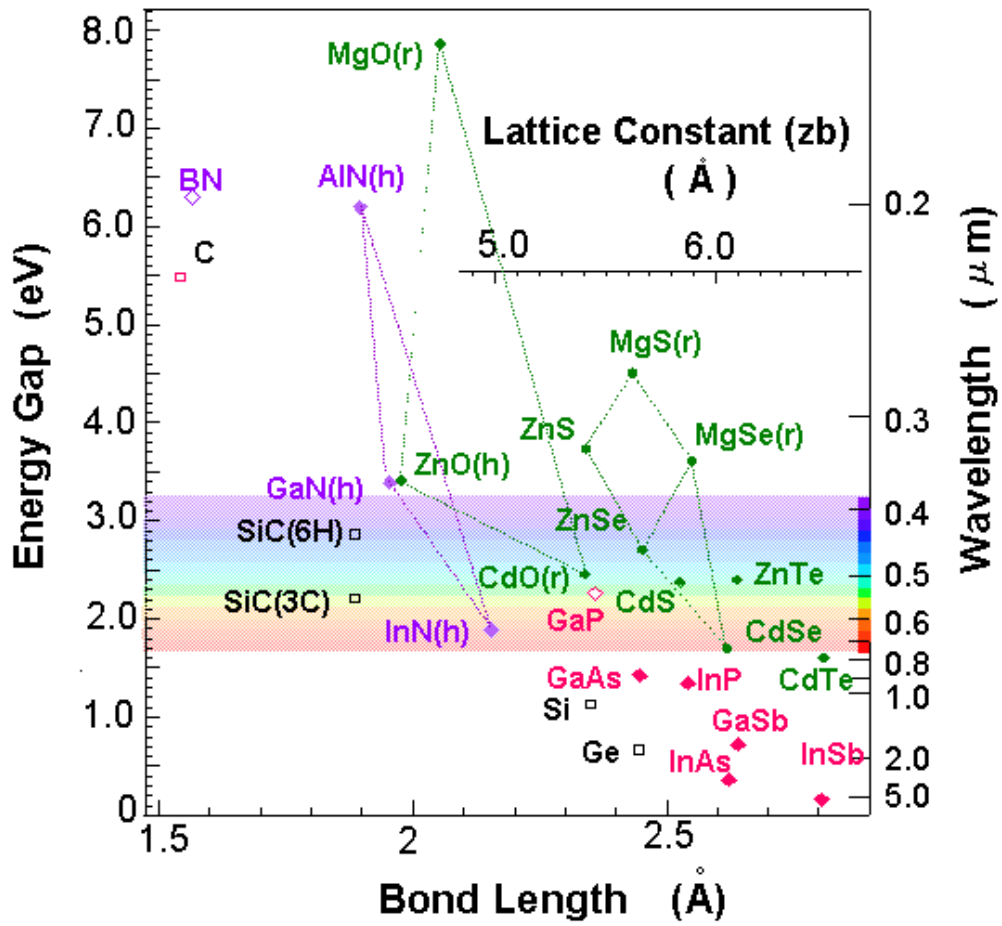


Figure 2 The corresponding band gap range of luminescence semiconductors [13, 18].

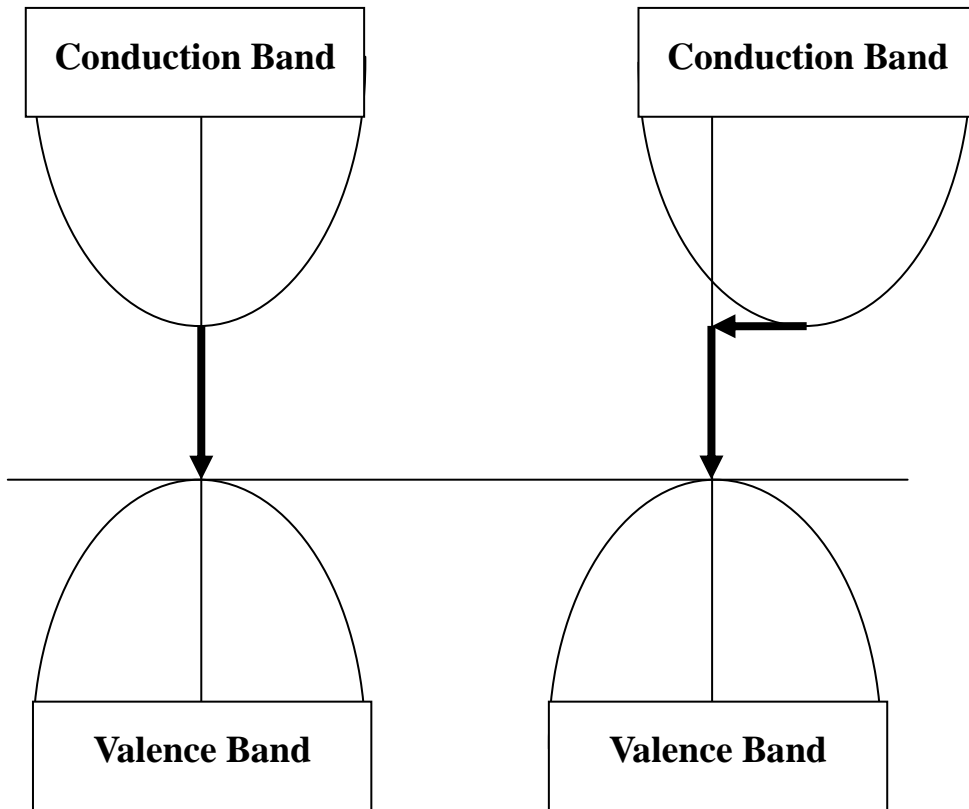


Figure 3 Schematic diagrams showing the transitions across (a) a direct band gap and (b) an indirect band gap.

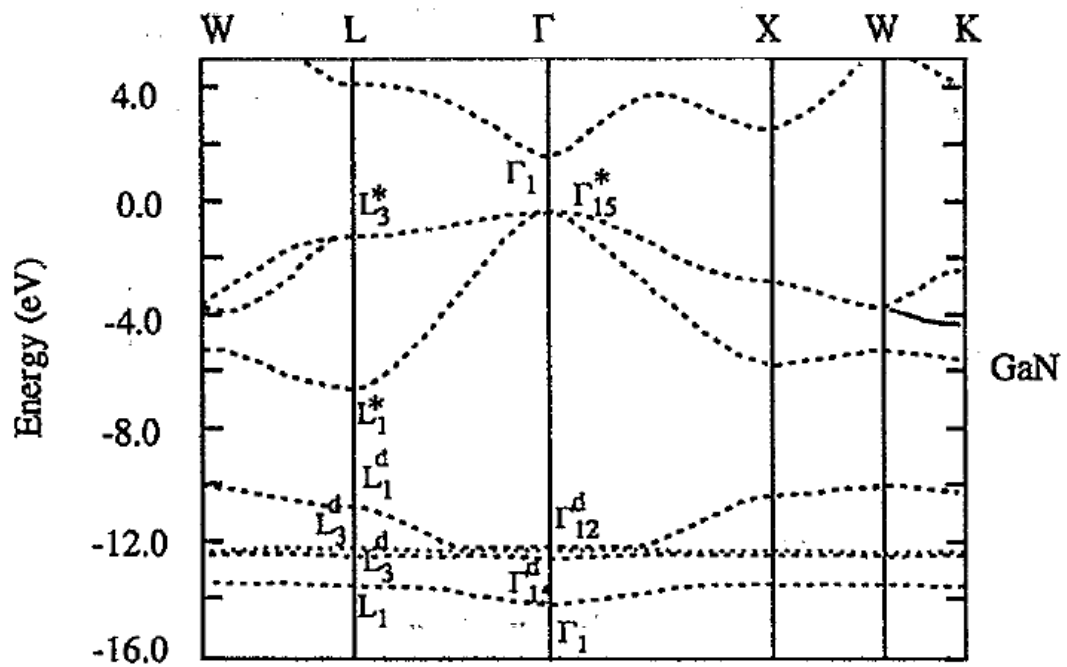


Figure 4 Direct band gap of GaN [11].

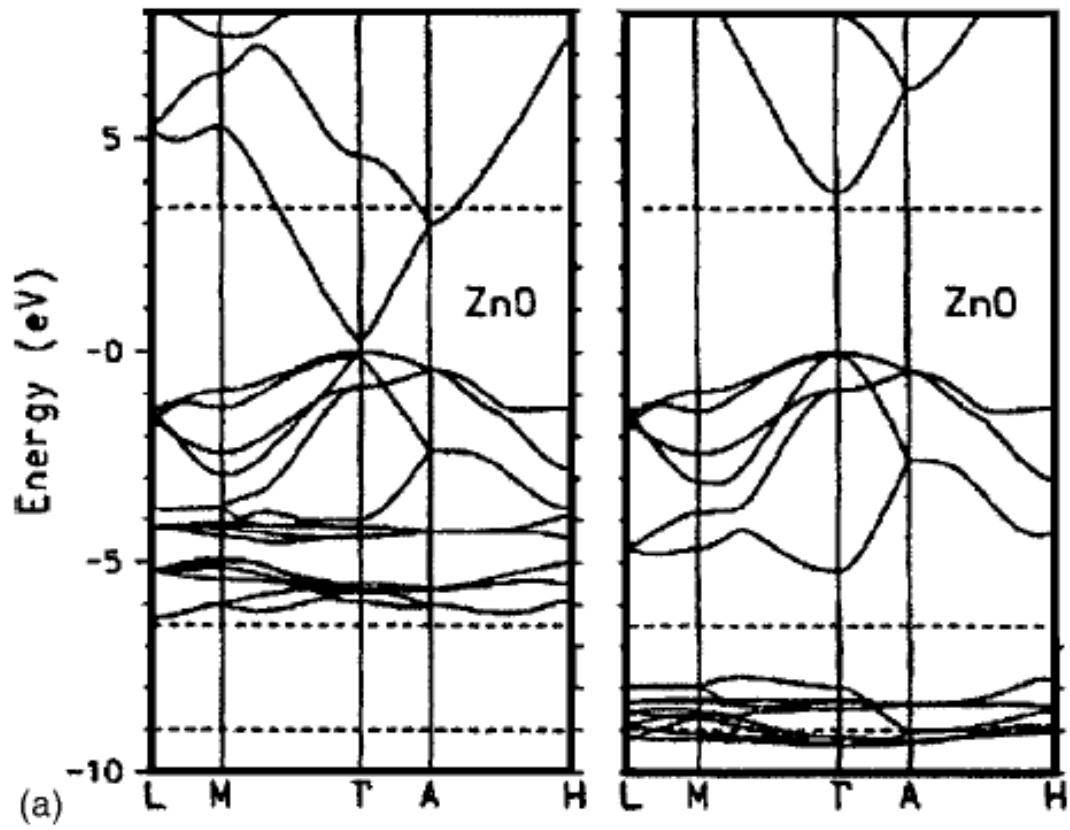


Figure 5 Direct band gap of ZnO [16].

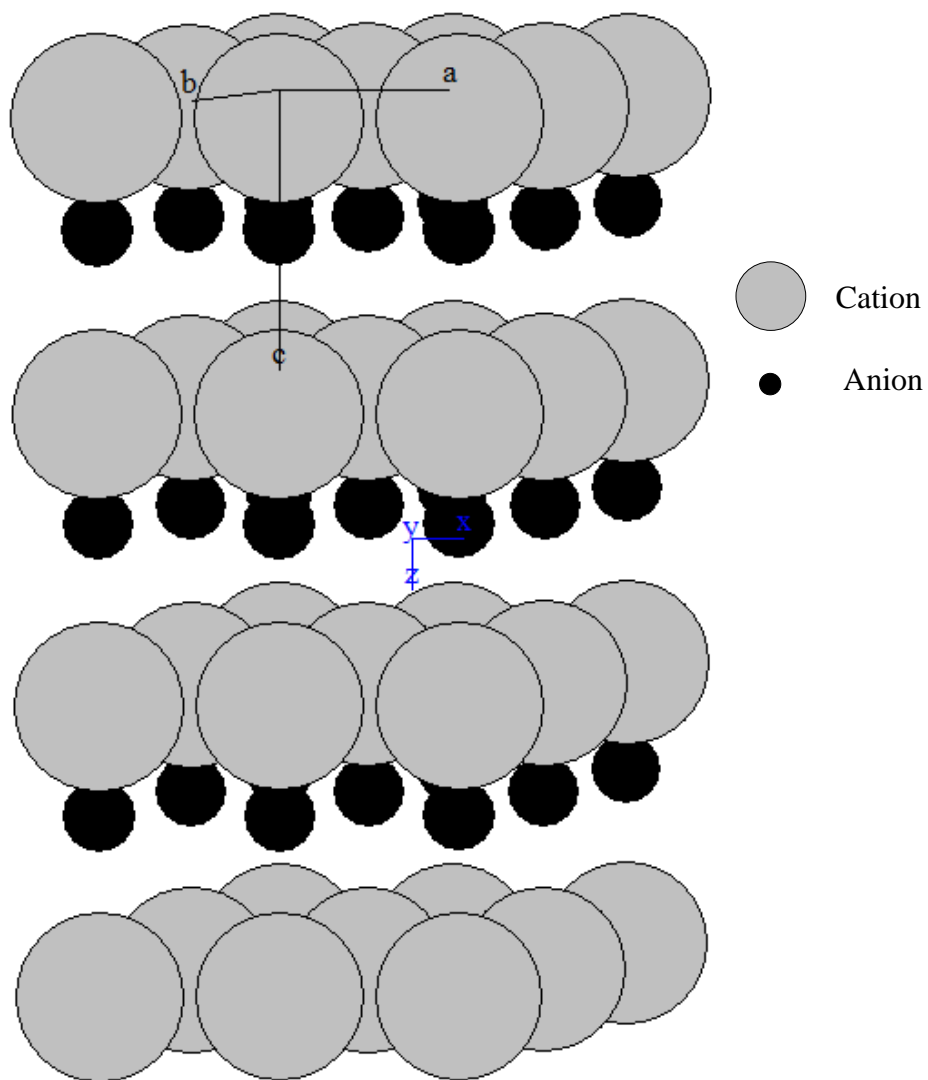


Figure 6 The Wurtzite hexagonal structure.

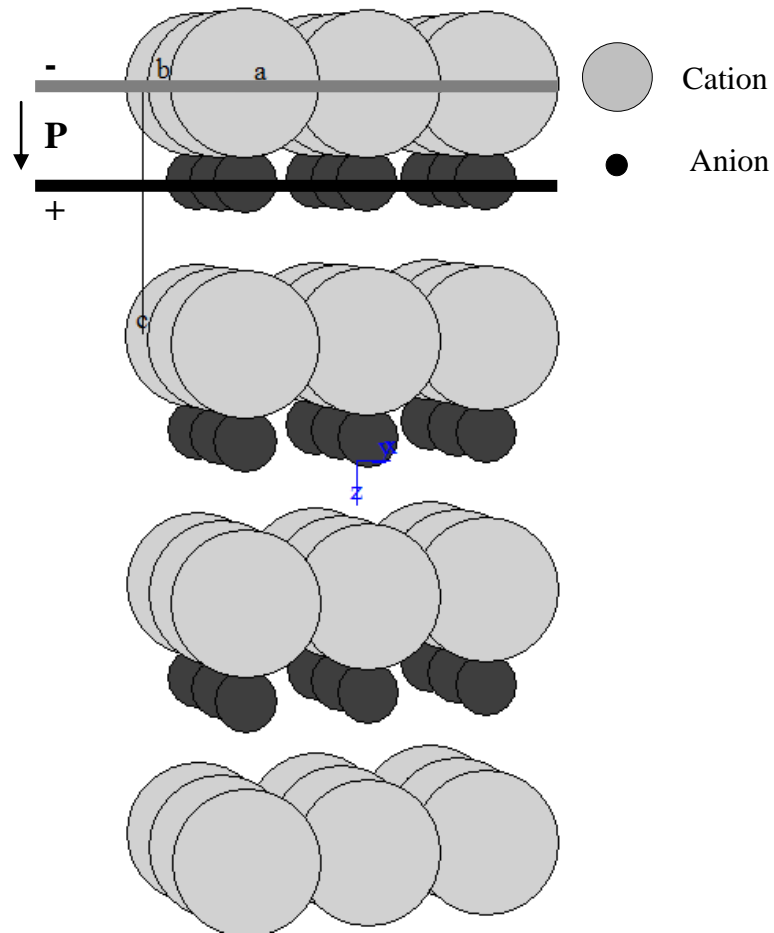


Figure 7 The Wurtzite structure along $[0001]$ c-axis.

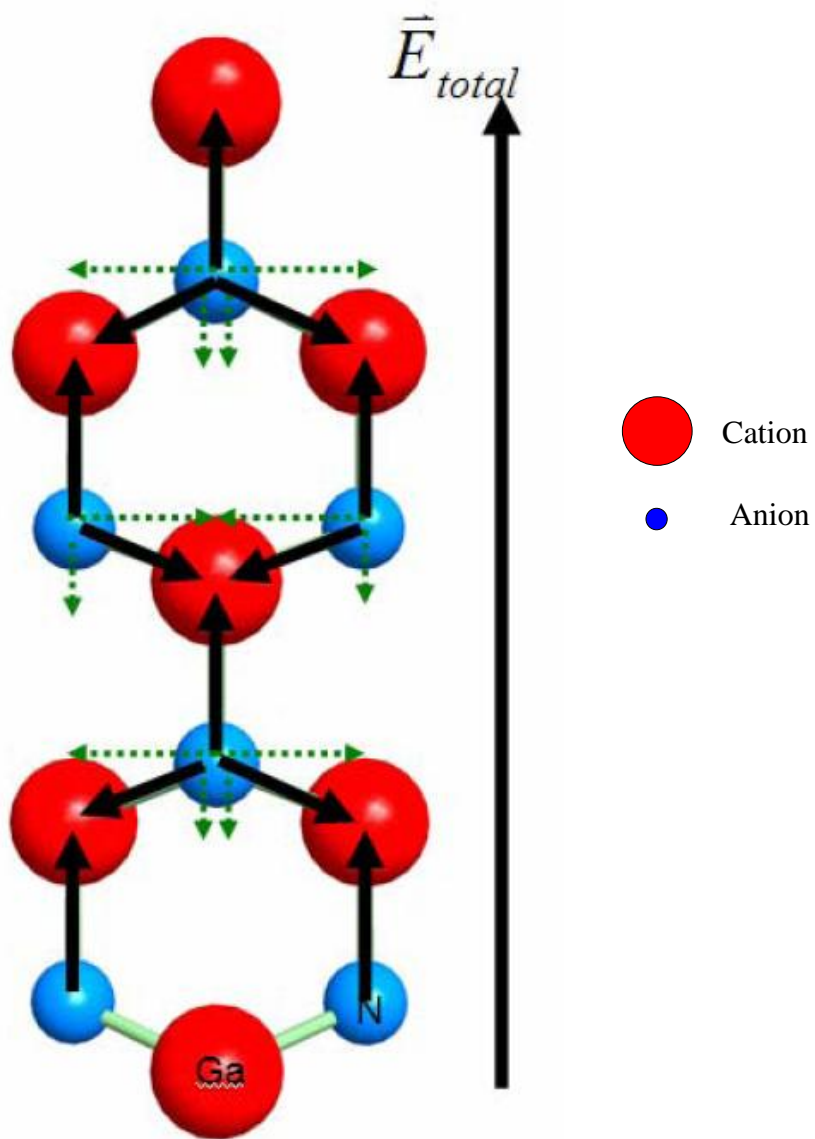


Figure 8 A sketch of induce the intrinsic electric field [37, 51].

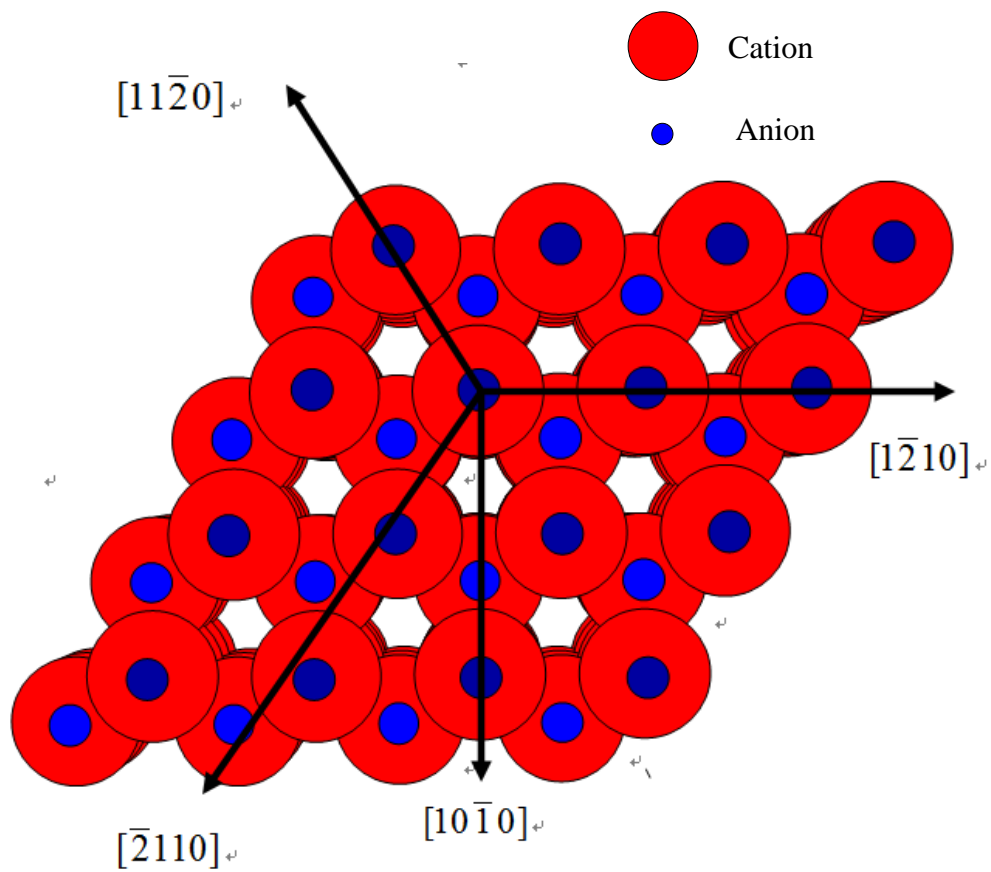


Figure 9 Non-polarity directions of GaN.

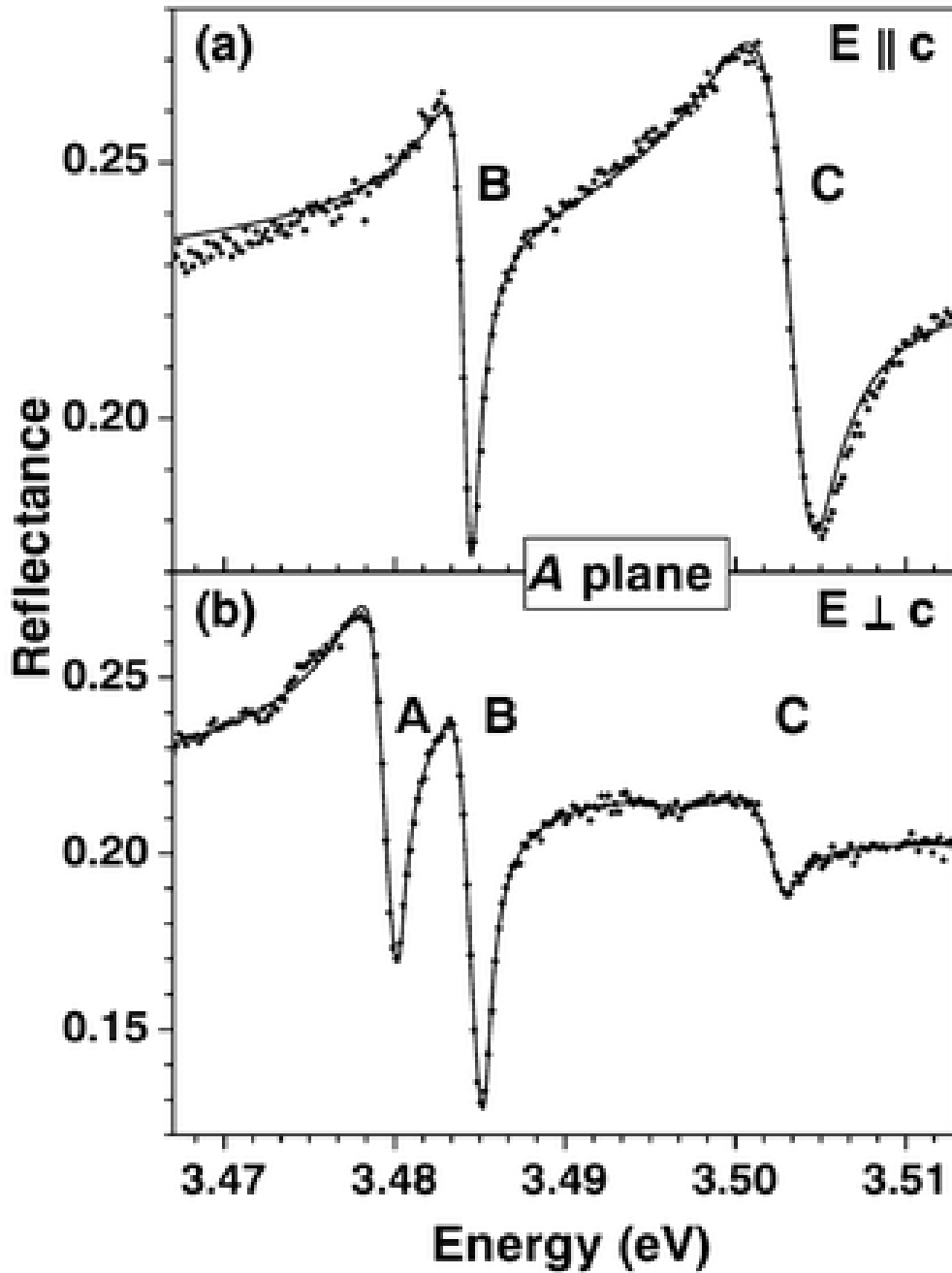
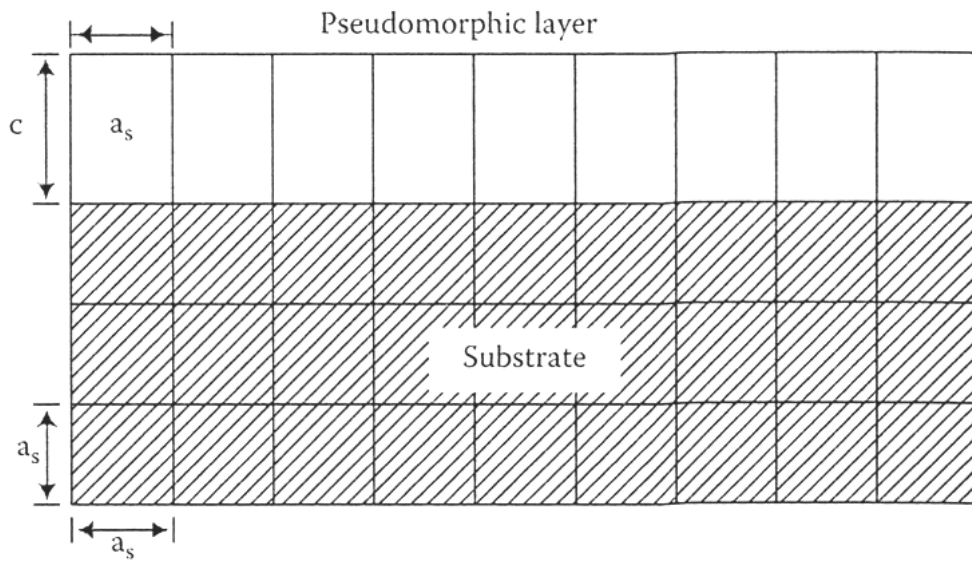
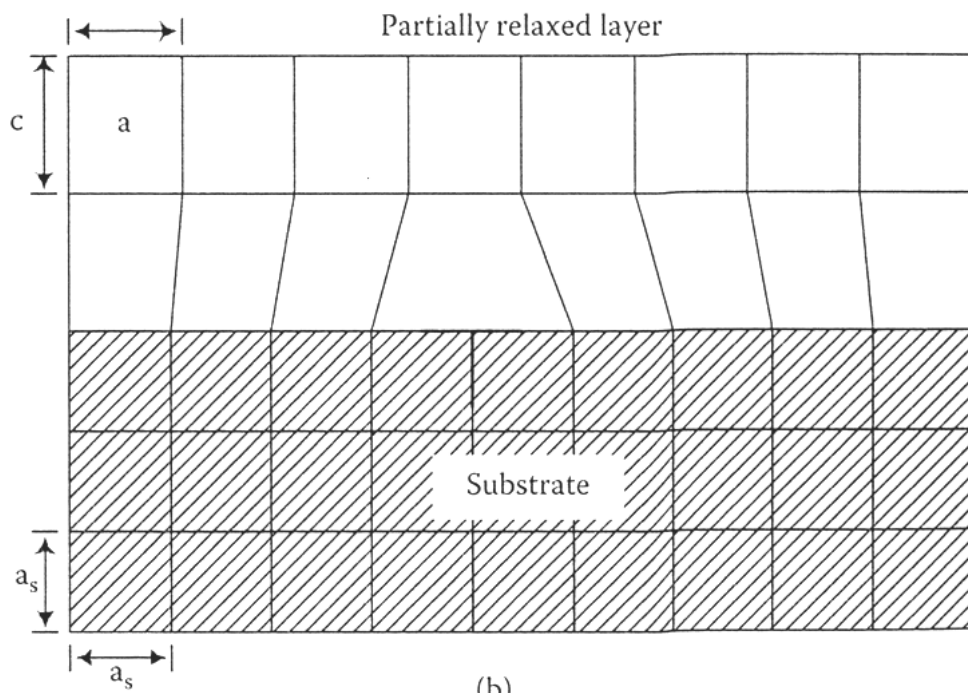


Figure 10 The figures show the reflectance spectra of unstrained A-plane GaN with the light polarized parallel (a) and perpendicular (b) to the c-axis. Clearly, the A exciton is visible only in (b), demonstrating a polarization anisotropy of 100% in this spectral range [22-25].



(a)



(b)

Figure 11 Growth of hetero-epilayer (a) pseudomorphic (b) strain free layer [92, 108].

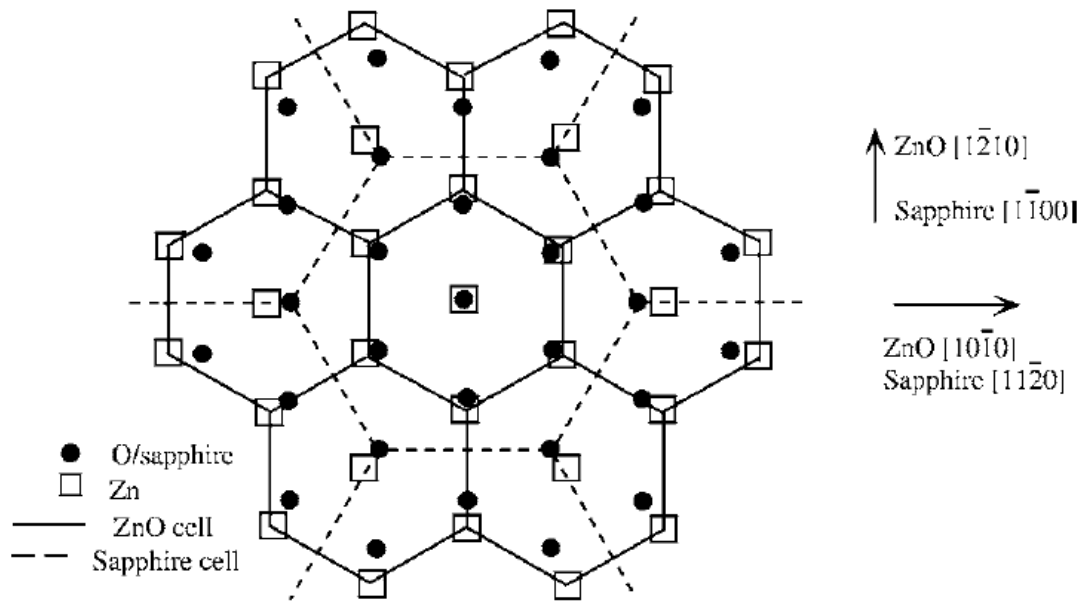
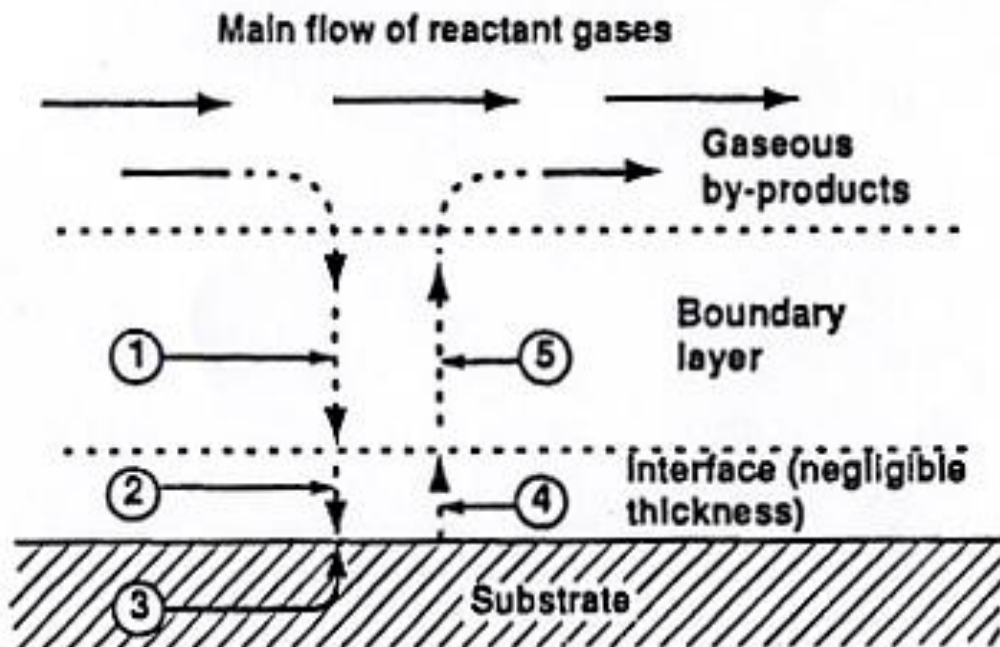
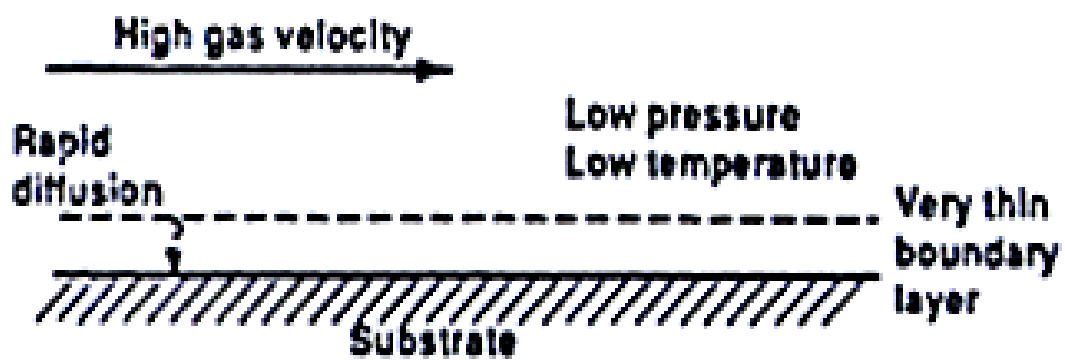


Figure 12 Schematic diagram showing the epitaxial relationships of c-plane ZnO grown on sapphire (0001) [16].



1. Diffusion in of reactants through boundary layer
2. Adsorption of reactants on substrate
3. Chemical reaction takes place
4. Desorption of adsorbed species
5. Diffusion out of by-products

Figure 13 Chemical vapor deposition (CVD) process [93, 109].



(a)

Figure 14 Low temperature, pressure and high gas velocity conditions of CVD [93, 109].

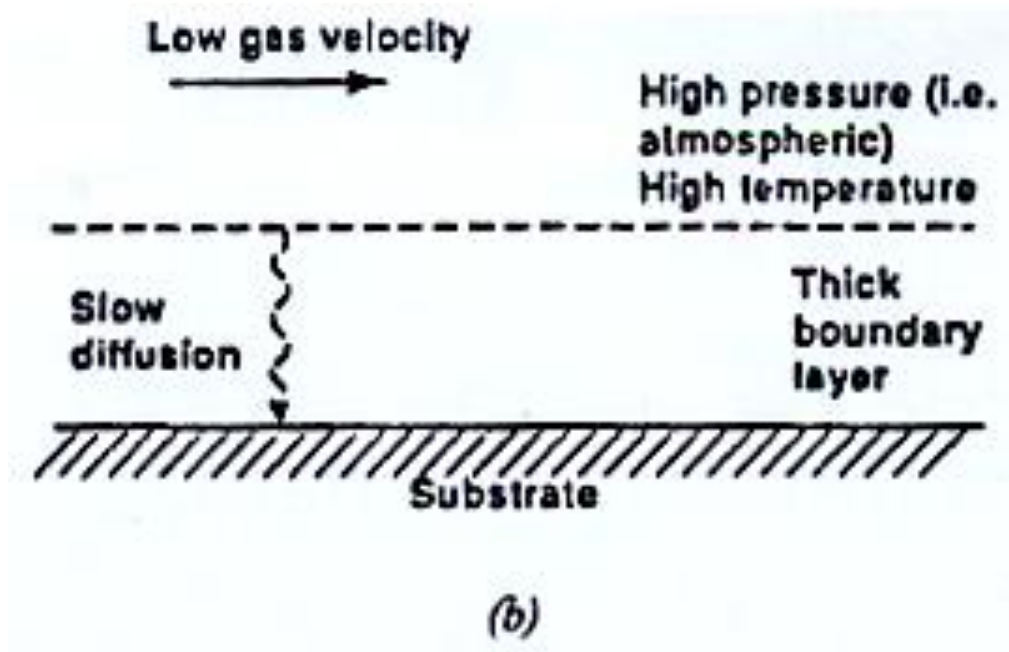


Figure 15 High temperature, pressure and low gas velocity conditions of CVD [93, 109].

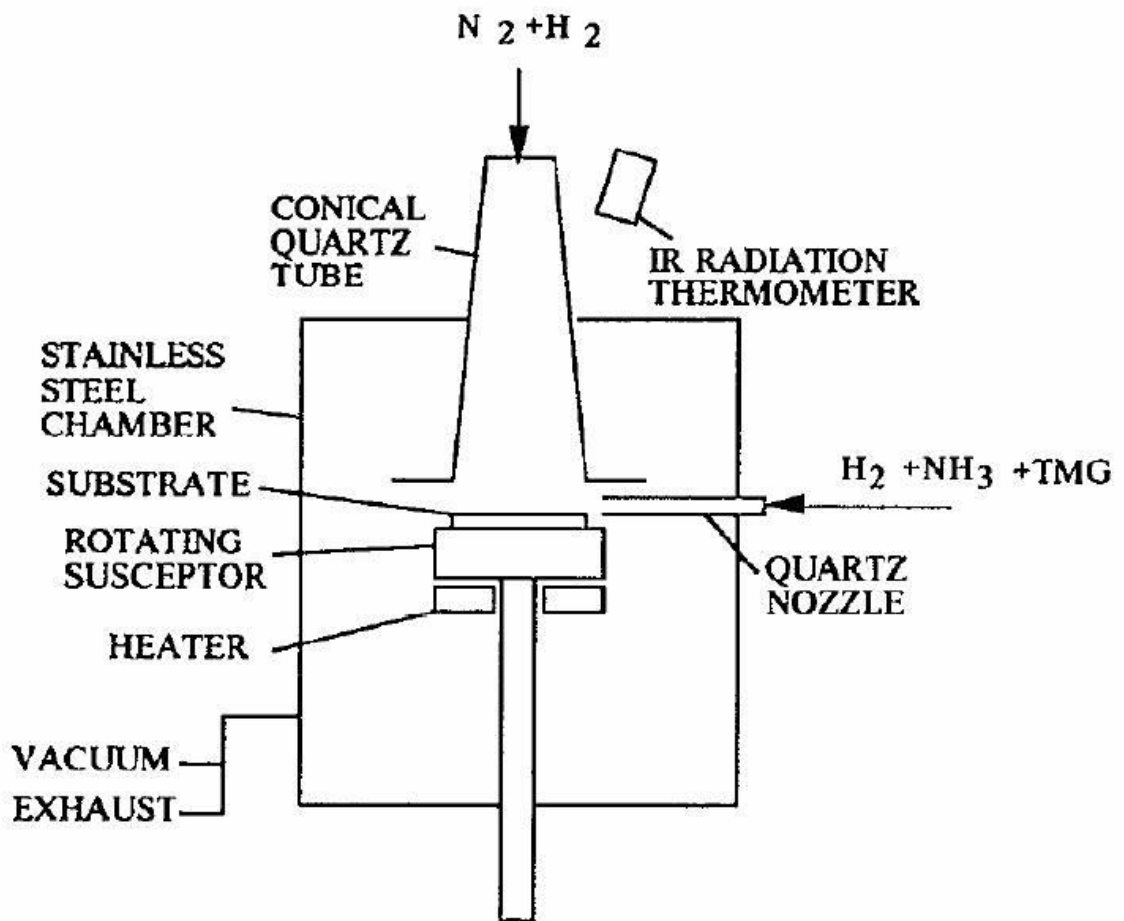


Figure 16 Two-Flow MOCVD (TF-MOCVD) [48].

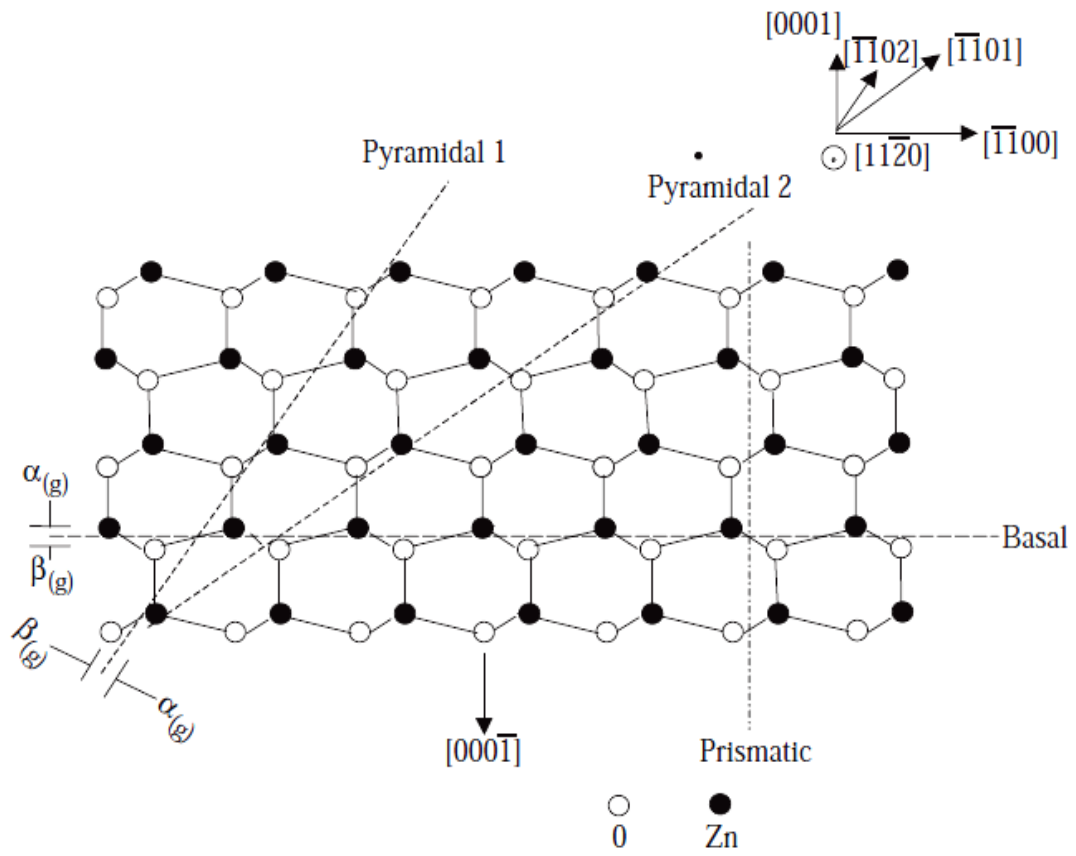


Figure 17 Projection of wurzite hexagonal structure [55].

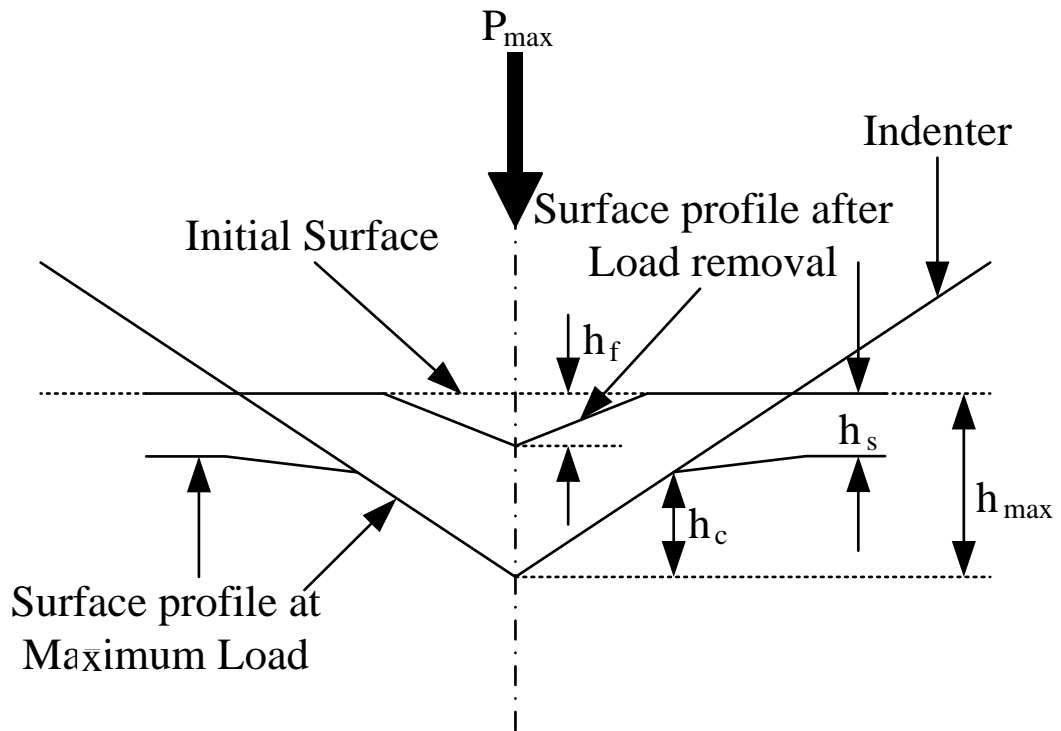


Figure 18 The sketch of the nanoindentation testing [52].

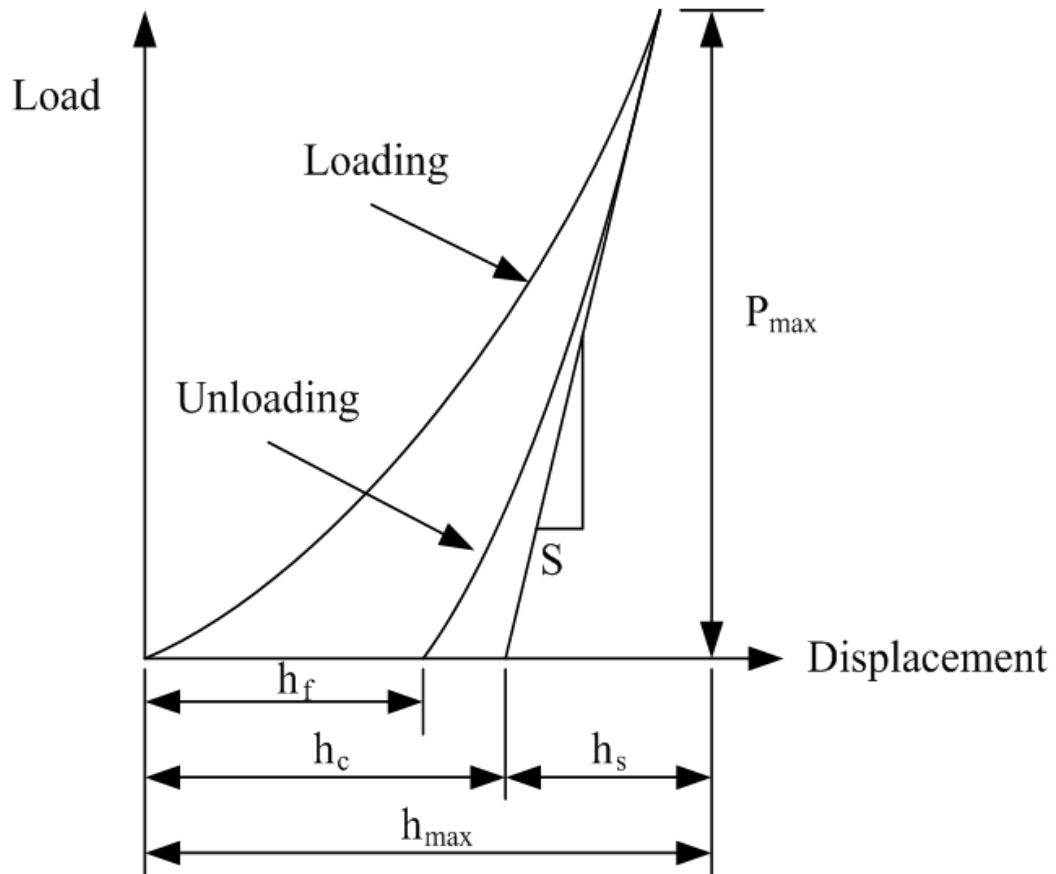


Figure 19 The sketch of the nanoindentation load-displacement (p-h) curve [52].

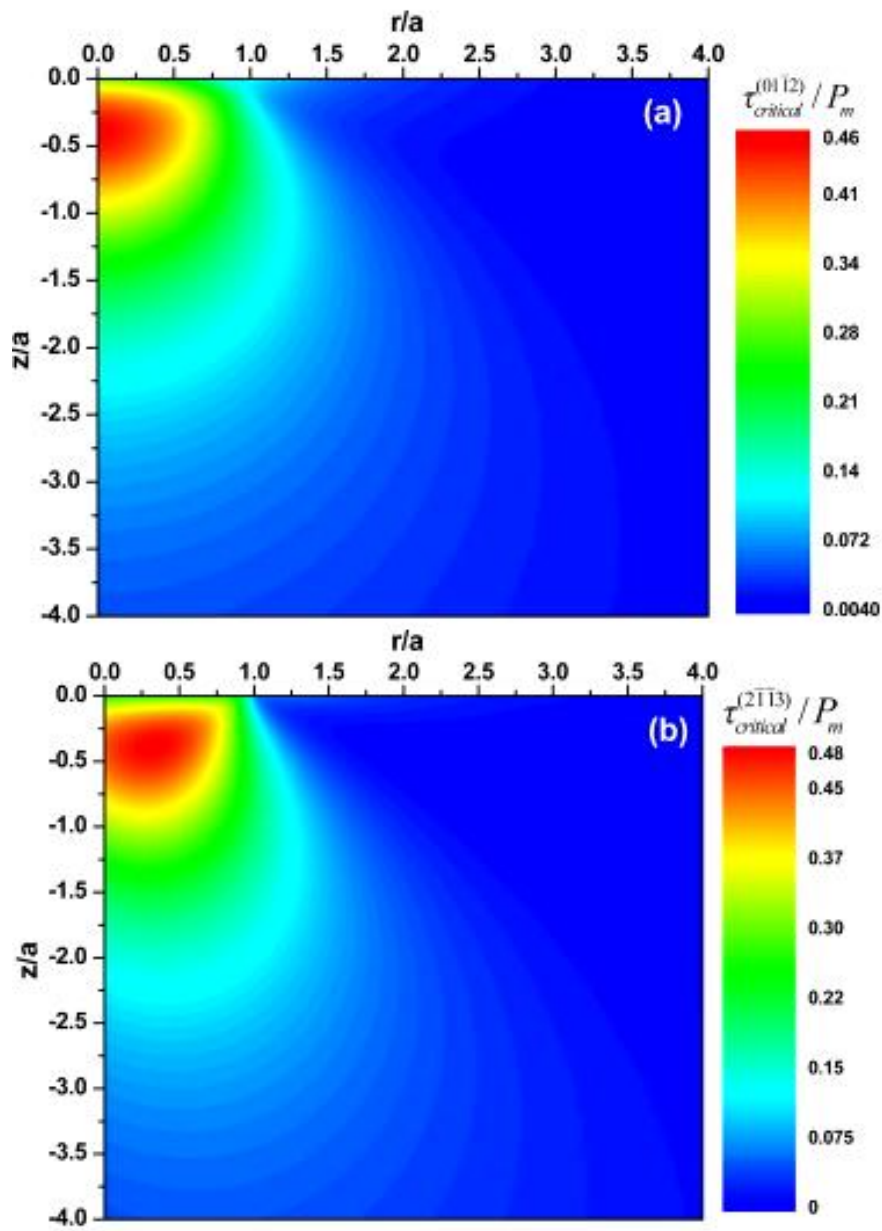


Figure 20 Contour plot of the CRSS of Berkovich tip at $(01\bar{1}2)$ slip plane (a) and $(2\bar{1}\bar{1}3)$ slip plane (b), where distances r and z are normalized by the contact radius a [53].

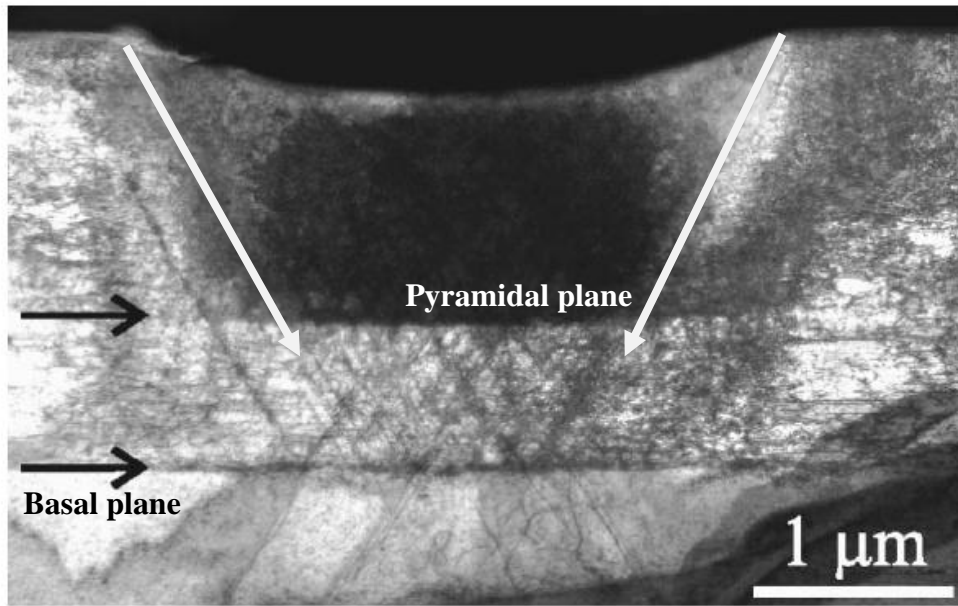


Figure 21 The bright field cross section TEM image of spherical indent in ZnO at maximum load of 50 mN, the black arrow point out the basal plane (0001) and the white arrow point out the pyramidal plane $\{10\bar{1}1\}$ [57].

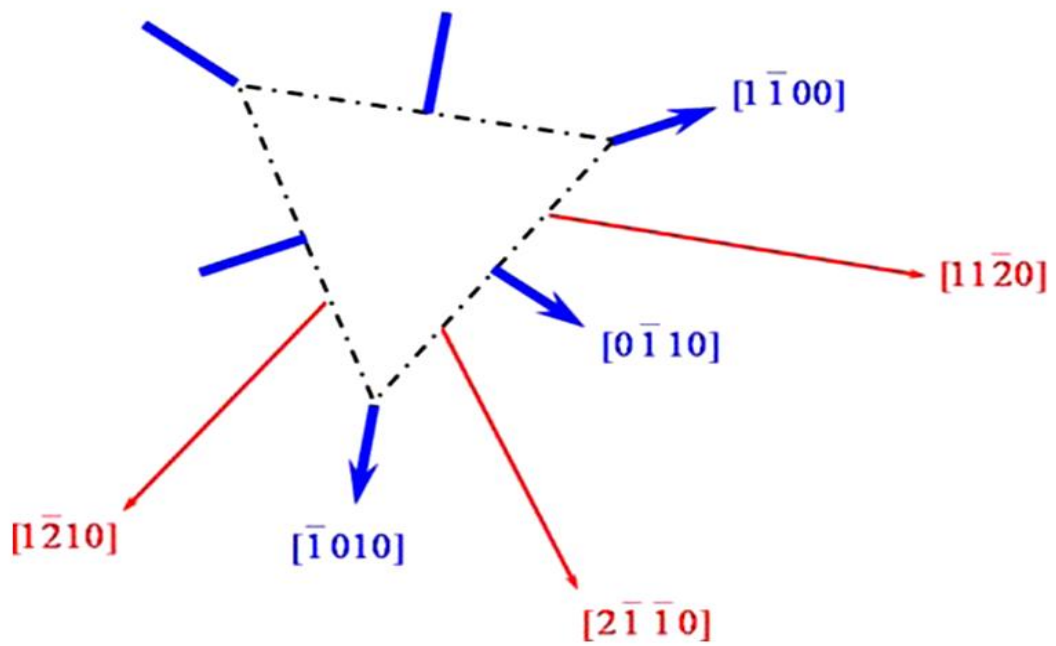


Figure 22 The sketch of slip directions. Thin lines represent the first slip system. Thick lines represent the secondary slip system [53].

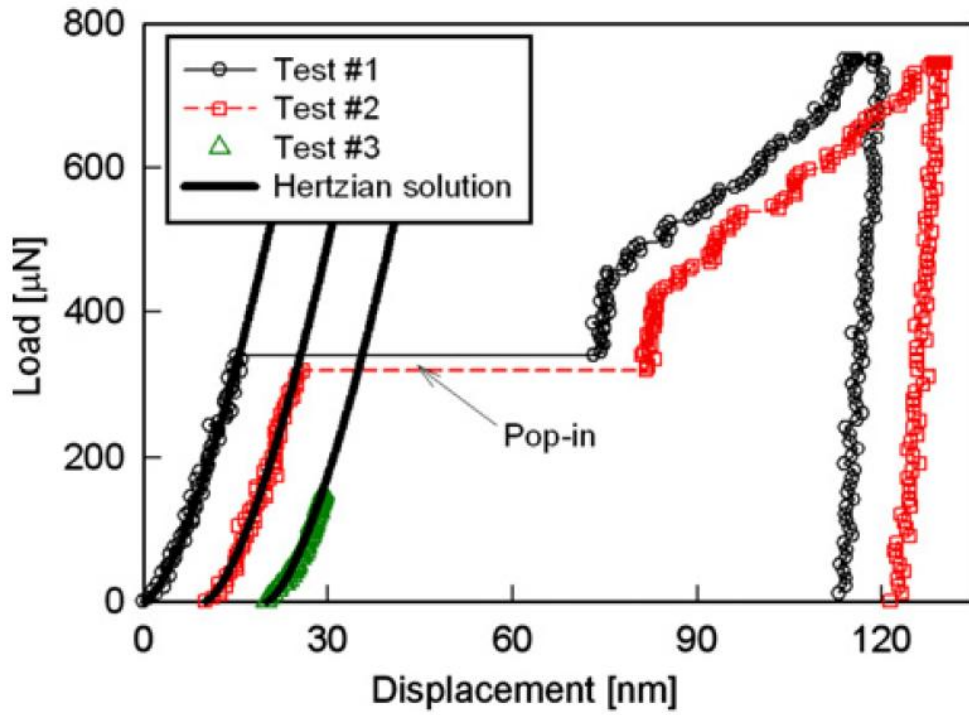


Figure 23 Typical nanoindentation load–displacement data for annealed (100) Ni obtained using a 0.58 μm radius spherical indenter. Elastic contact (Hertzian) solutions are shown for the data below the pop-in loads [69].

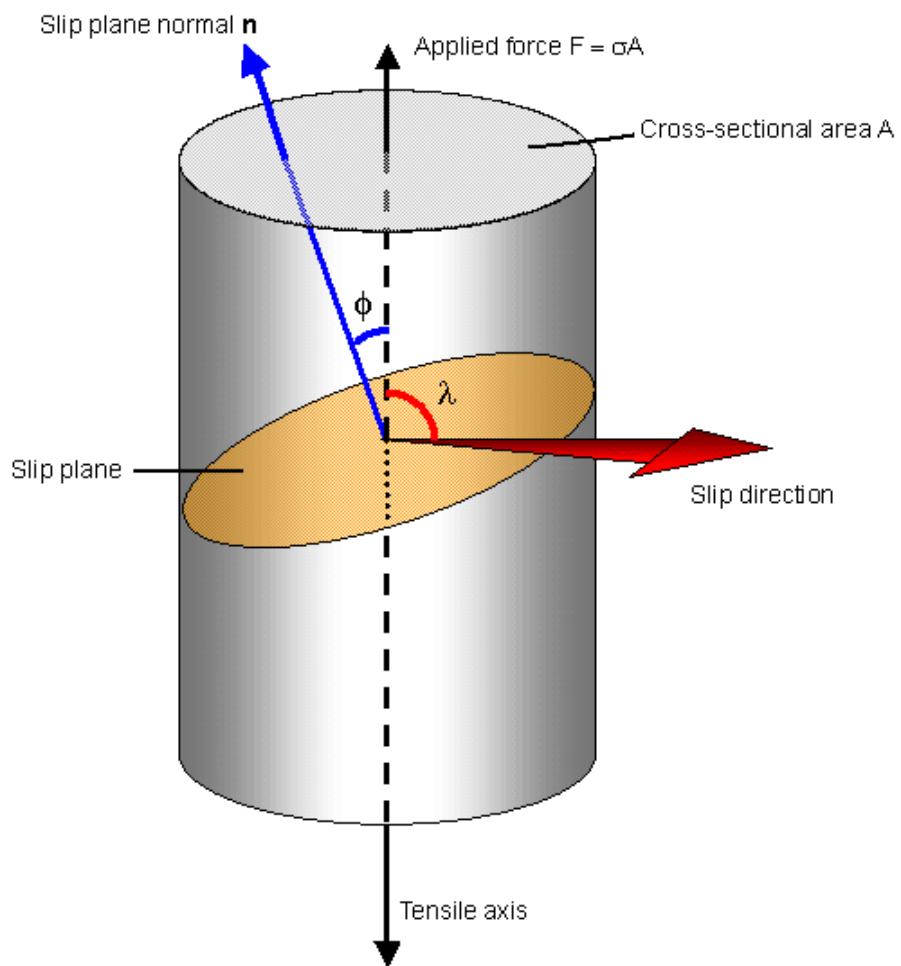


Figure 24 The sketch of resolve shear stress.

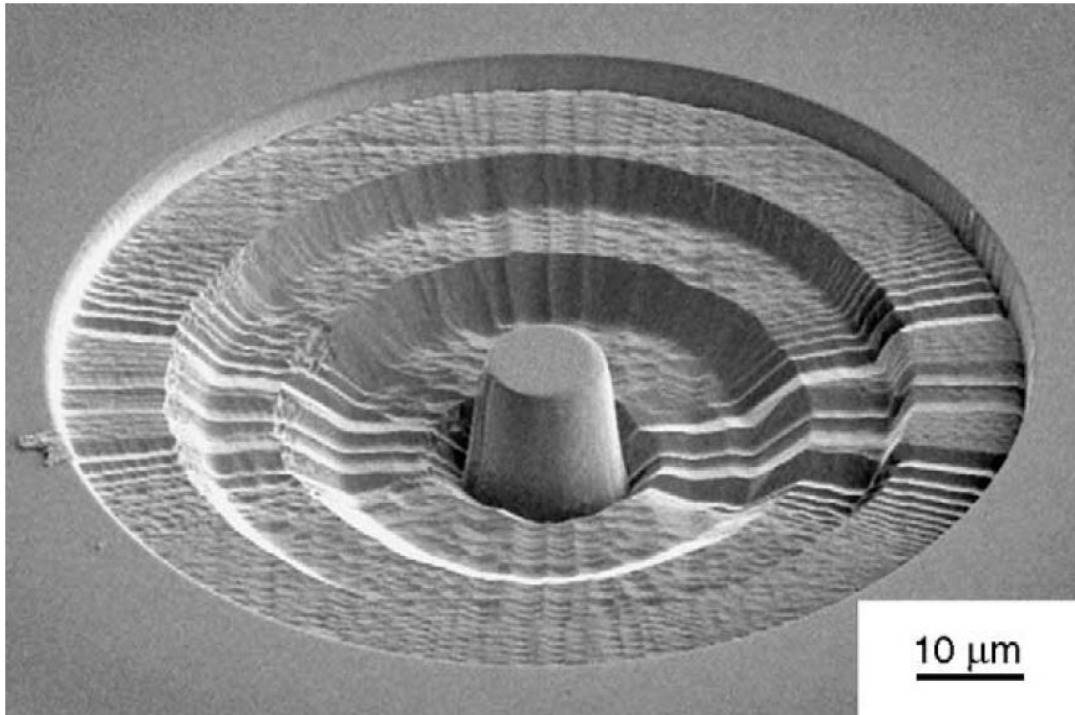


Figure 25 Annular milling patterns have been used to mill a roughly defined micropillar sample of Ni single crystal [48, 62].

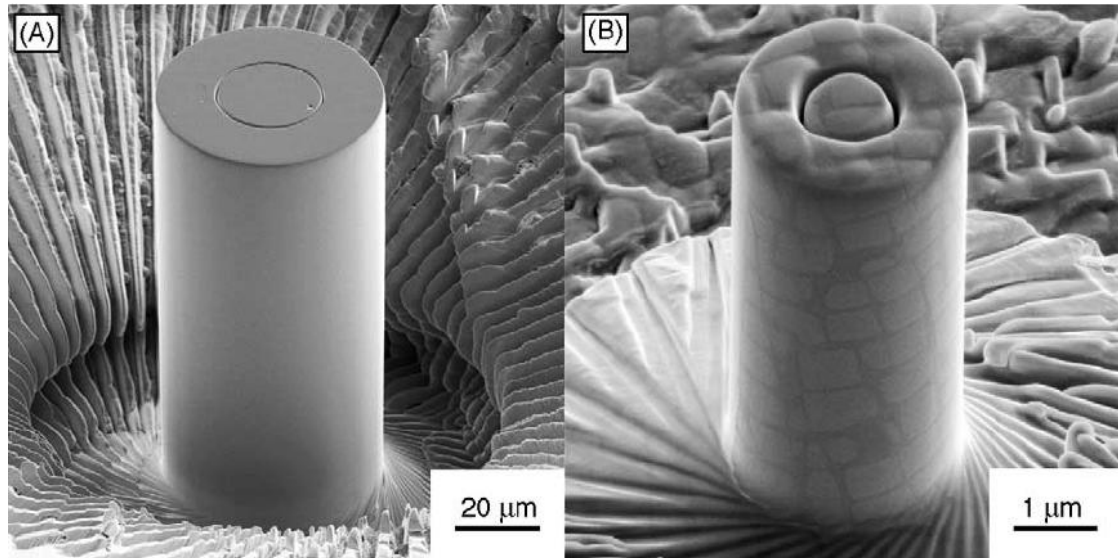


Figure 26 The microcompression samples were fabricated into (A) a Ni₃Al alloy and (B) Ni-based superalloy by using lathe milling program. The diameter of microcompression samples are 43 μm and 2.3 μm, respectively [48, 62].

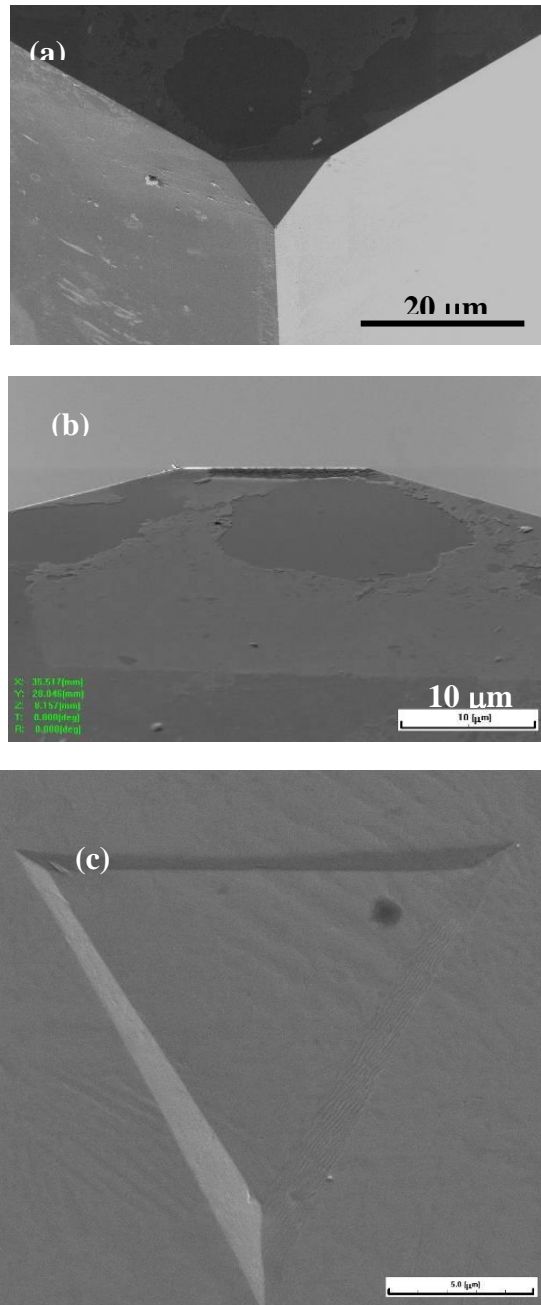


Figure 27 SEM micrographs of the flat-punch tip: (a) top view and (b) side view and (c) projected area of the punch tip.

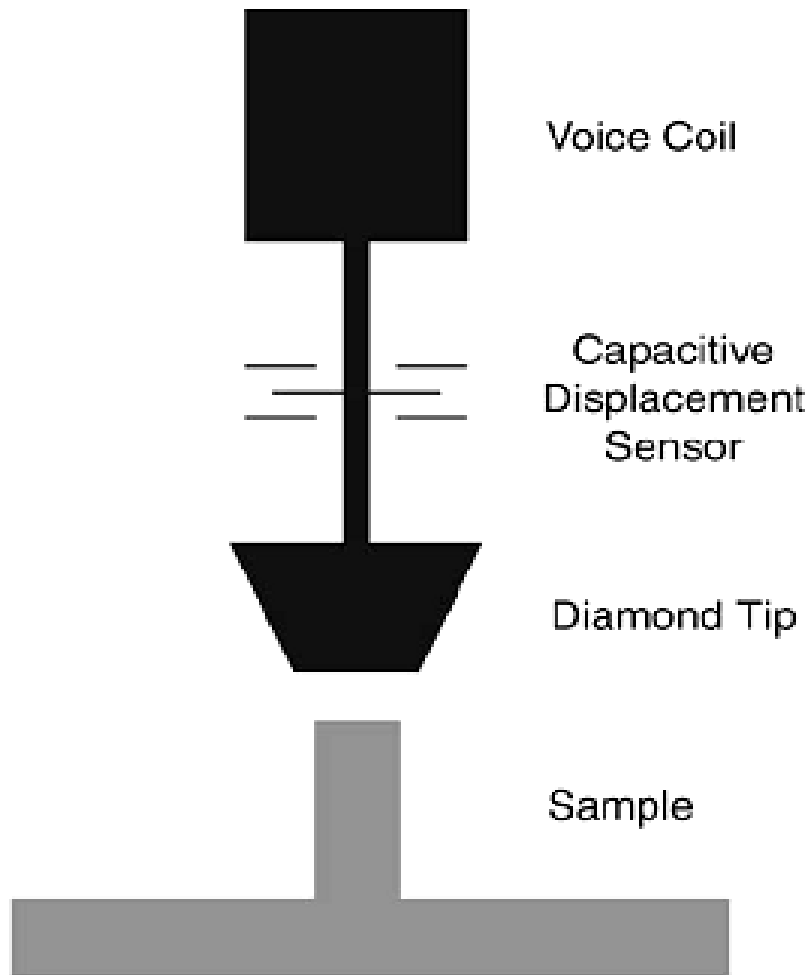


Figure 28 Schematic drawing of the microcompression test setup [64].

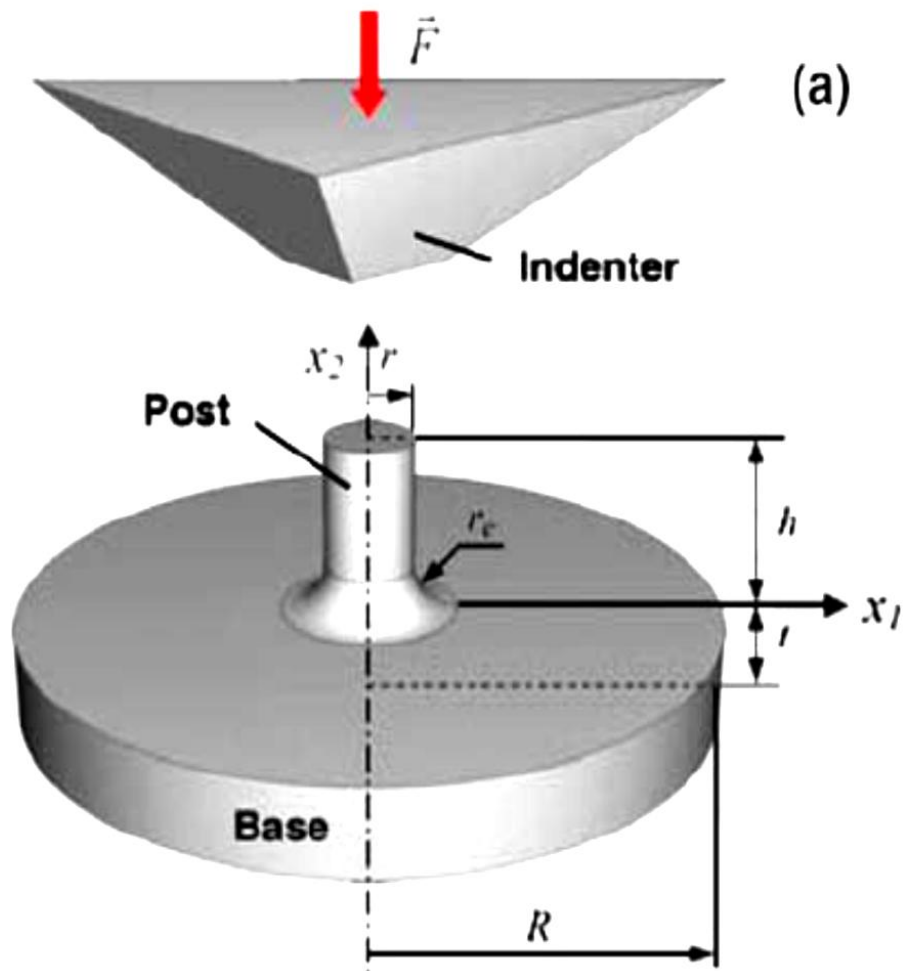


Figure 29 Schematic of a cylindrical pillar and its base [64].

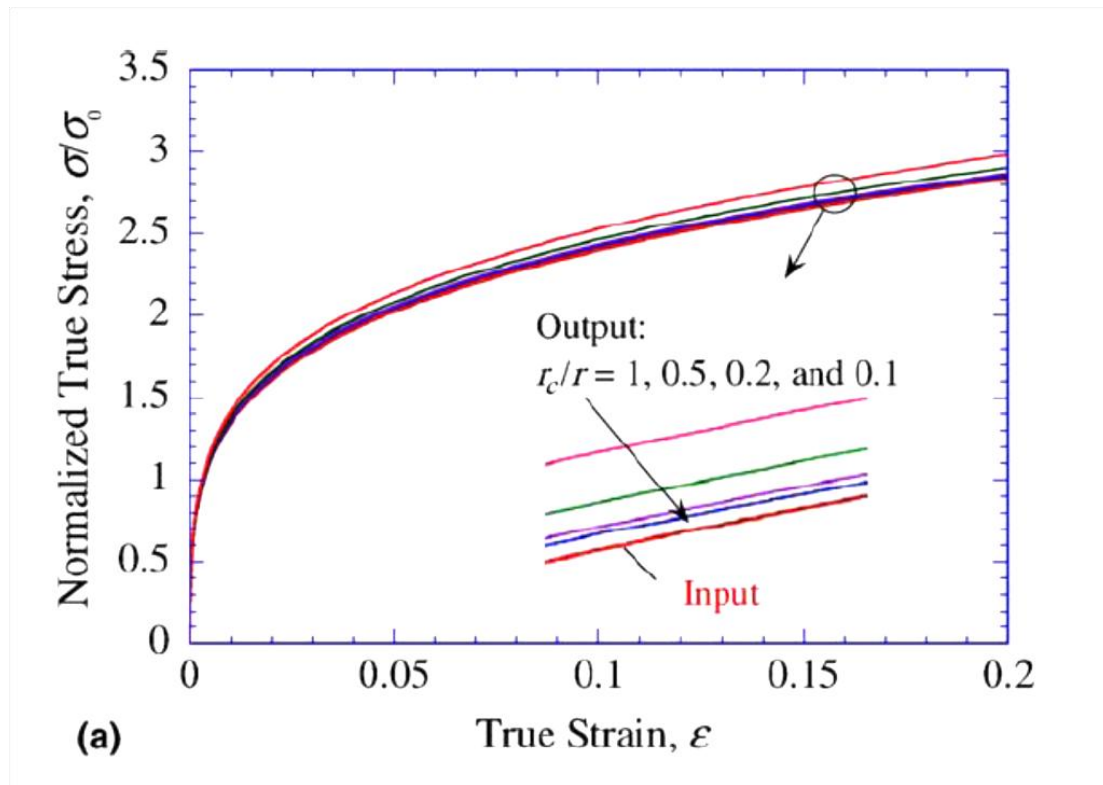


Figure 30 Effect of fillet radius/pillar radius ratio on numerical simulation output. The inset shows an enlargement of the circled region to facilitate comparison [21].

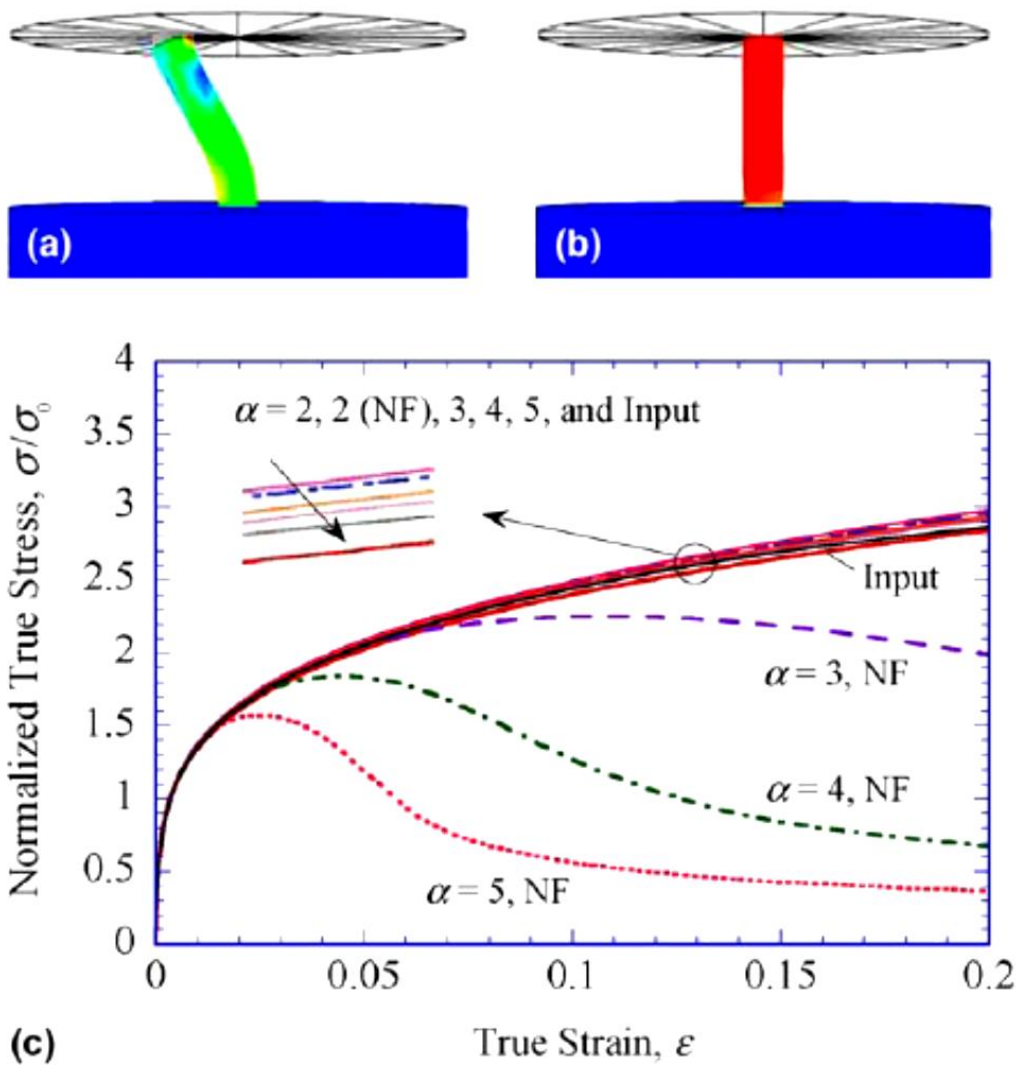


Figure 31 (a) Deformed configuration of a circular cylindrical pillar with an aspect ratio $\alpha = 5$ at a strain of 0.1. (b) Deformed configuration of the pillar at the same strain of 0.1, but now considering friction. (c) Input and output stress-strain curves for a pillar with an aspect ratios $\alpha=2\sim 5$, both with friction and without friction (NF) [21].

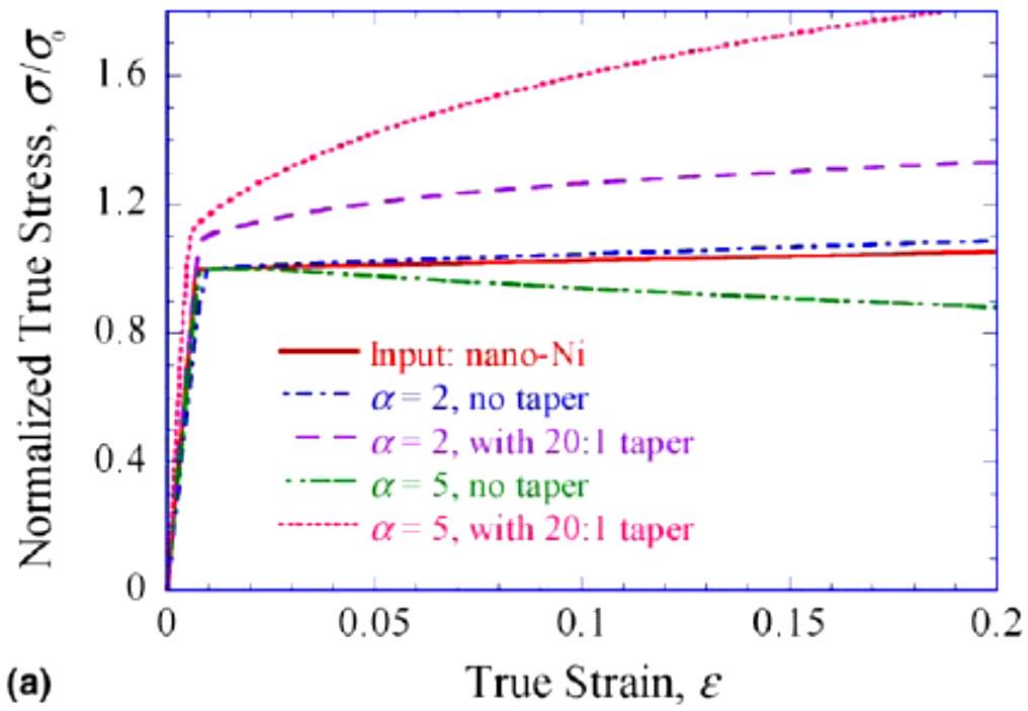


Figure 32 Effect of taper on numerical simulation output [21].

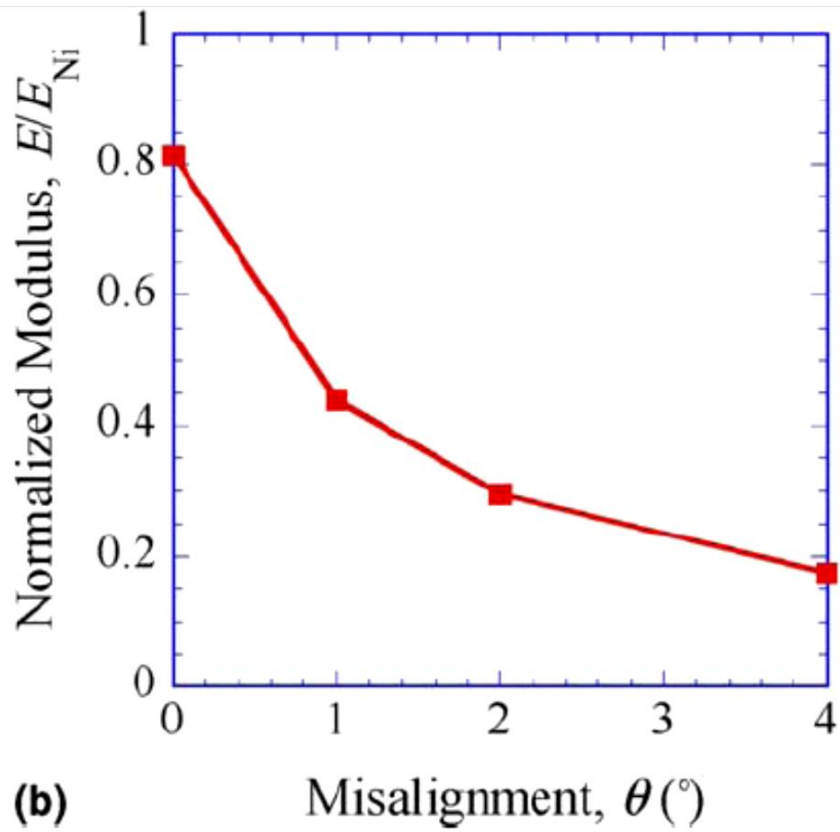


Figure 33 Effect of misalignment of the system on the error in elastic modulus [21].

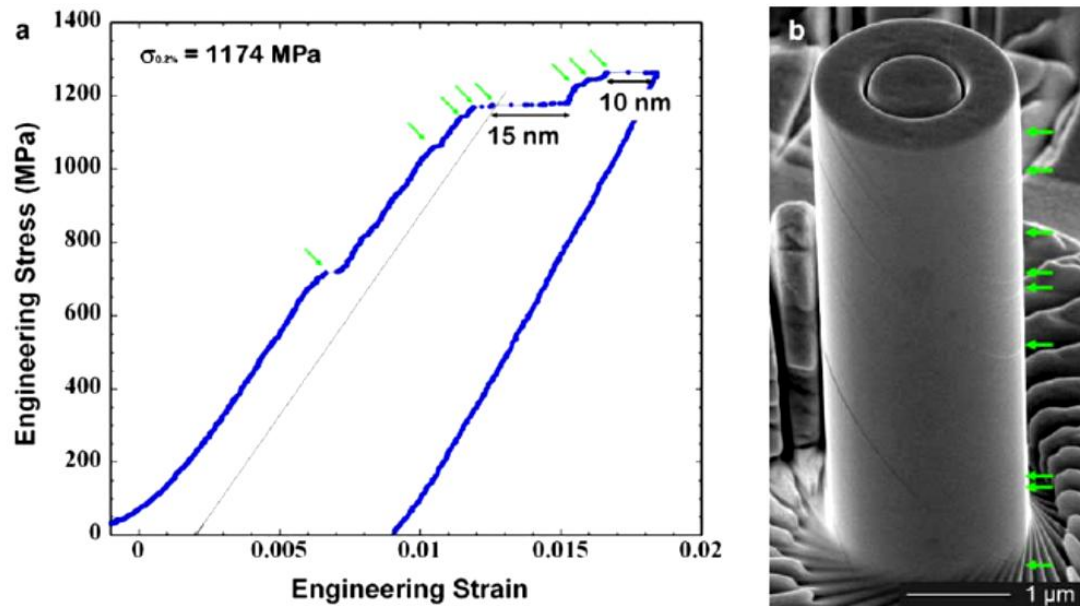


Figure 34 (a) The microcompressive engineering stress-strain curve of the $\text{Ni}_{76}\text{Al}_{24}$ alloy with 2 μm diameter. (b) SEM micrograph of a micropillar after microcompression test. Strain bursts are indicated by arrows in figure (a), and appearance of slip lines are also observed on the micropillar surface, as also indicated by arrows [67].

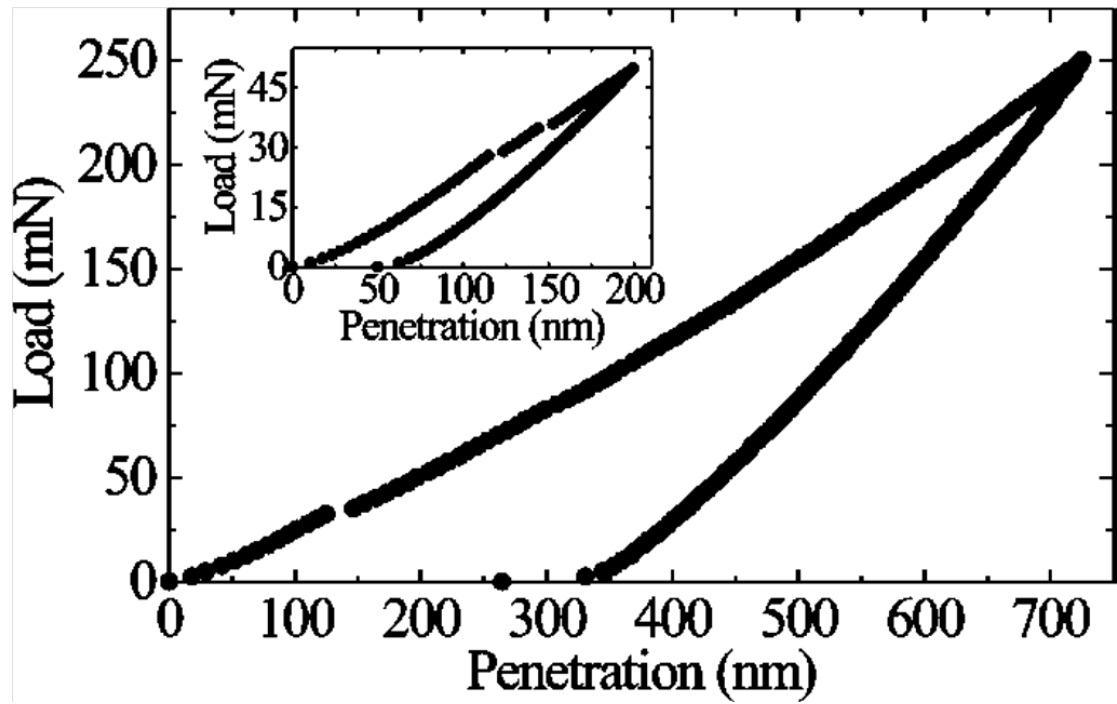


Figure 35 Typical load–penetration curve for a maximum load of 250 mN showing a pop-in event. Inset: Load–penetration curve for a maximum load of 50 mN showing multiple pop-in events at 28 and 34 mN [57].

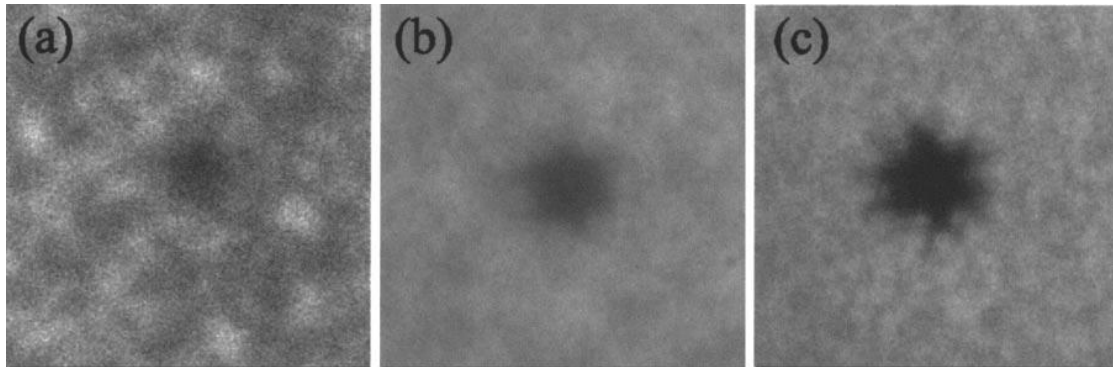


Figure 36 Room-temperature monochromatic CL images of spherical indents in GaN. The maximum loads and horizontal field widths are (a) 25 mN and 15 mm, (b) 50 mN and 15 mm, and (c) 200 mN and 30 mm. CL imaging conditions: electron beam energy 520 keV, CL wavelength =366 nm, and CL bandpass 52.5 nm [57].

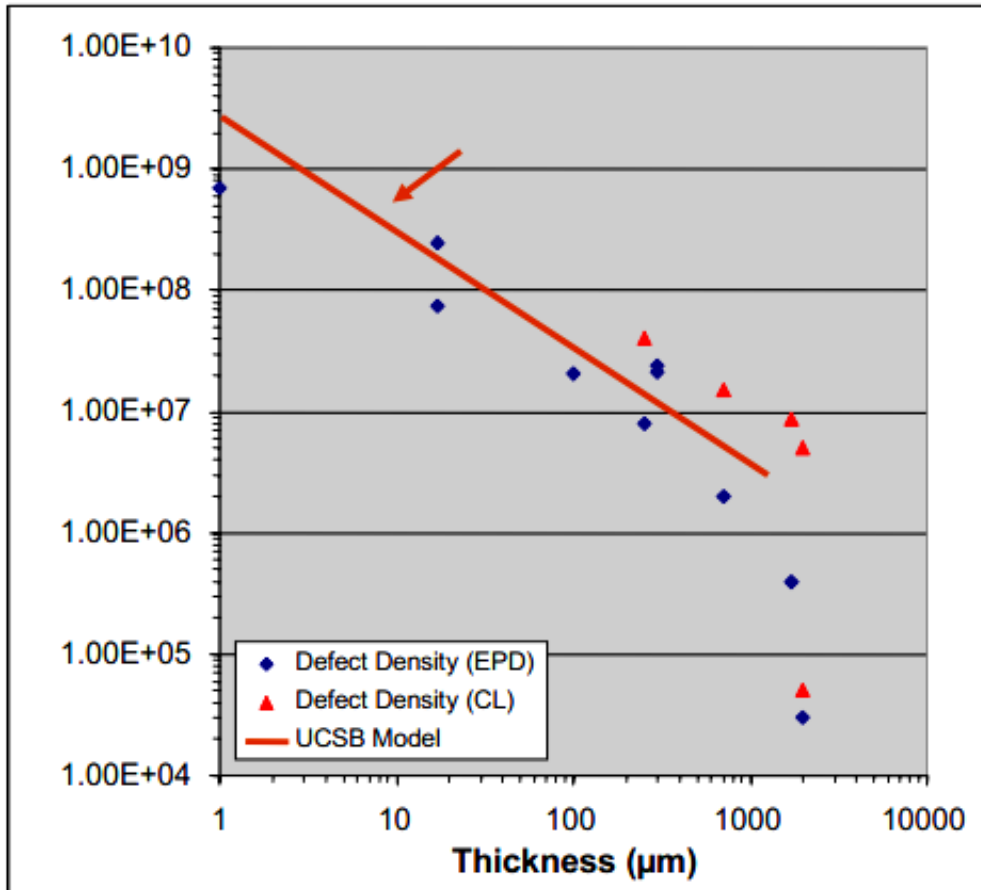


Figure 37 The threading dislocation density decreases with increasing thickness for thin film GaN/sapphire [80, 96].

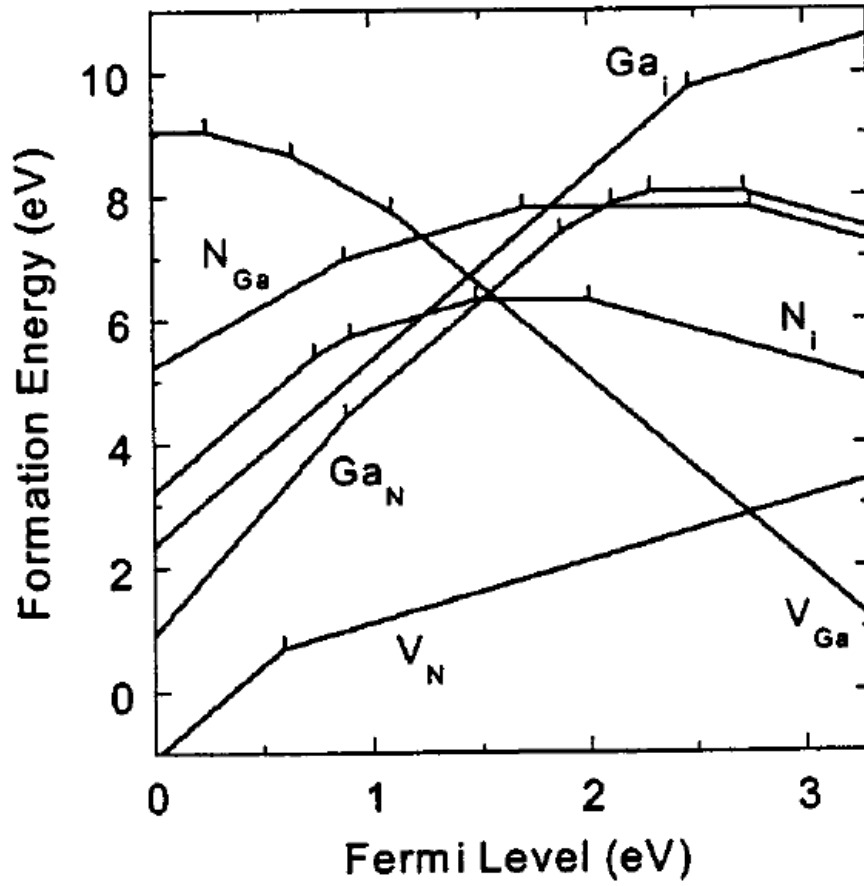


Figure 38 Formation energies as a function of Fermi level for native point defects in GaN [74]

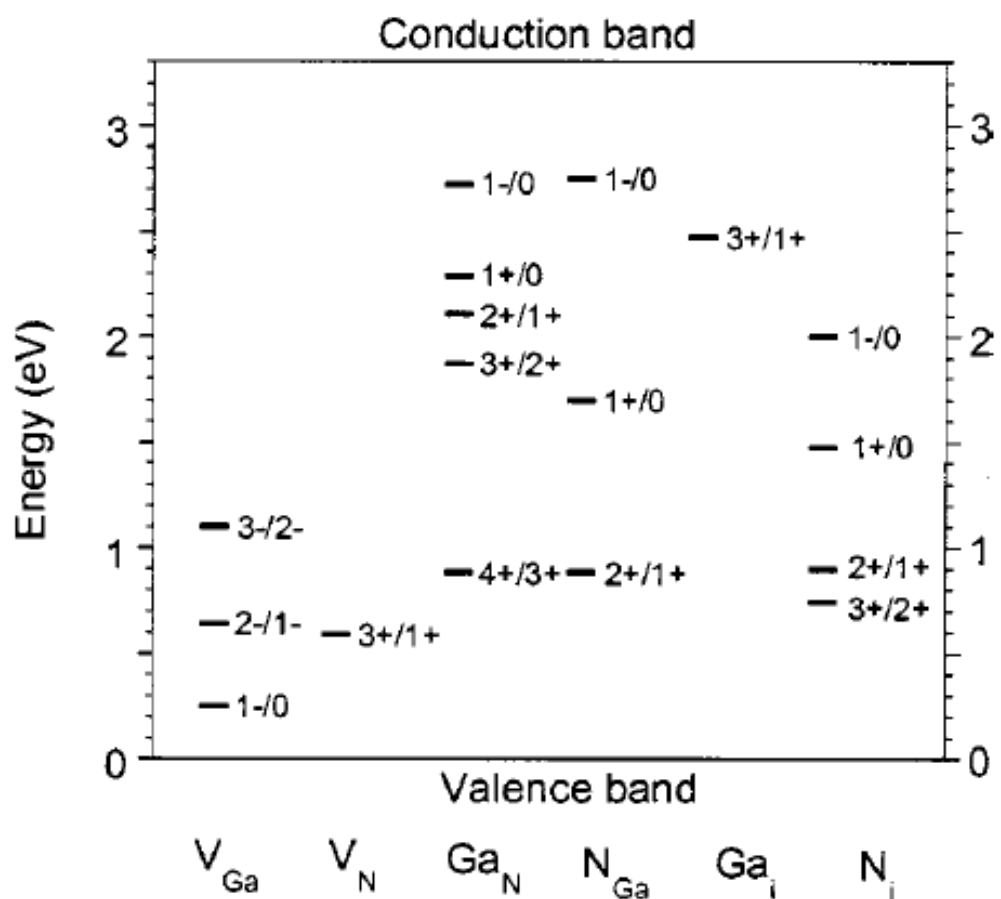


Figure 39 Transition levels and formation energy of native defects in GaN [74].

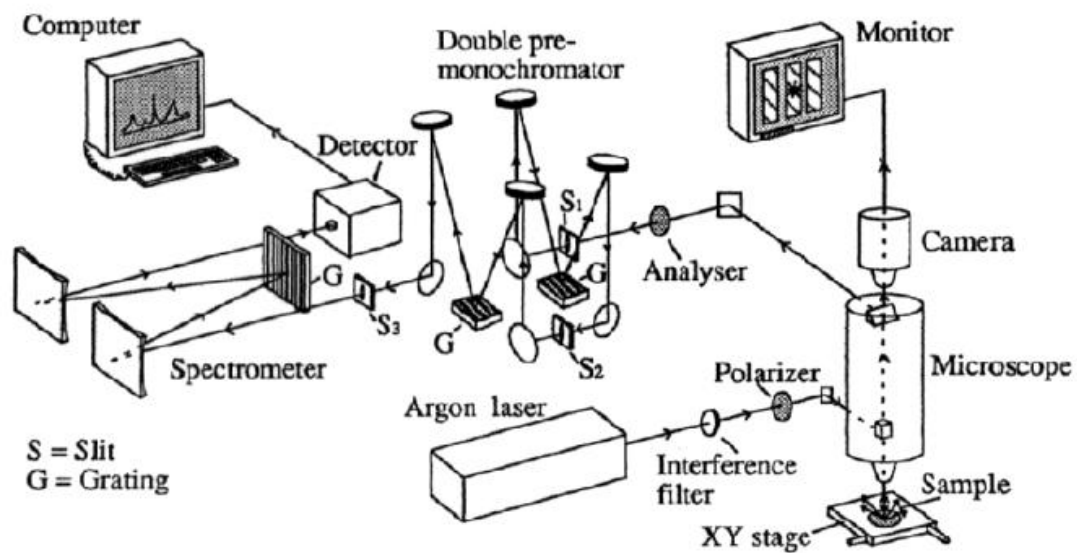


Figure 40 Experimental set up of a micro-Raman spectrometer [82].

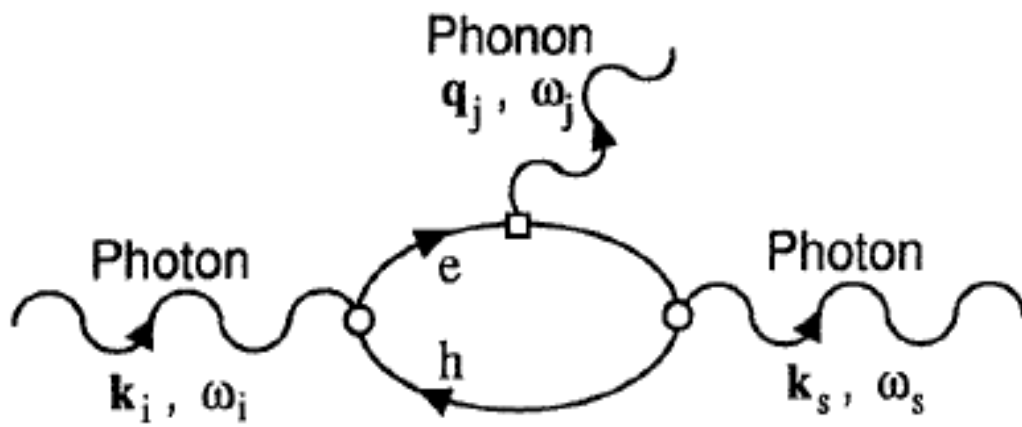


Figure 41 The diagram of anti-Stokes scattering [82].

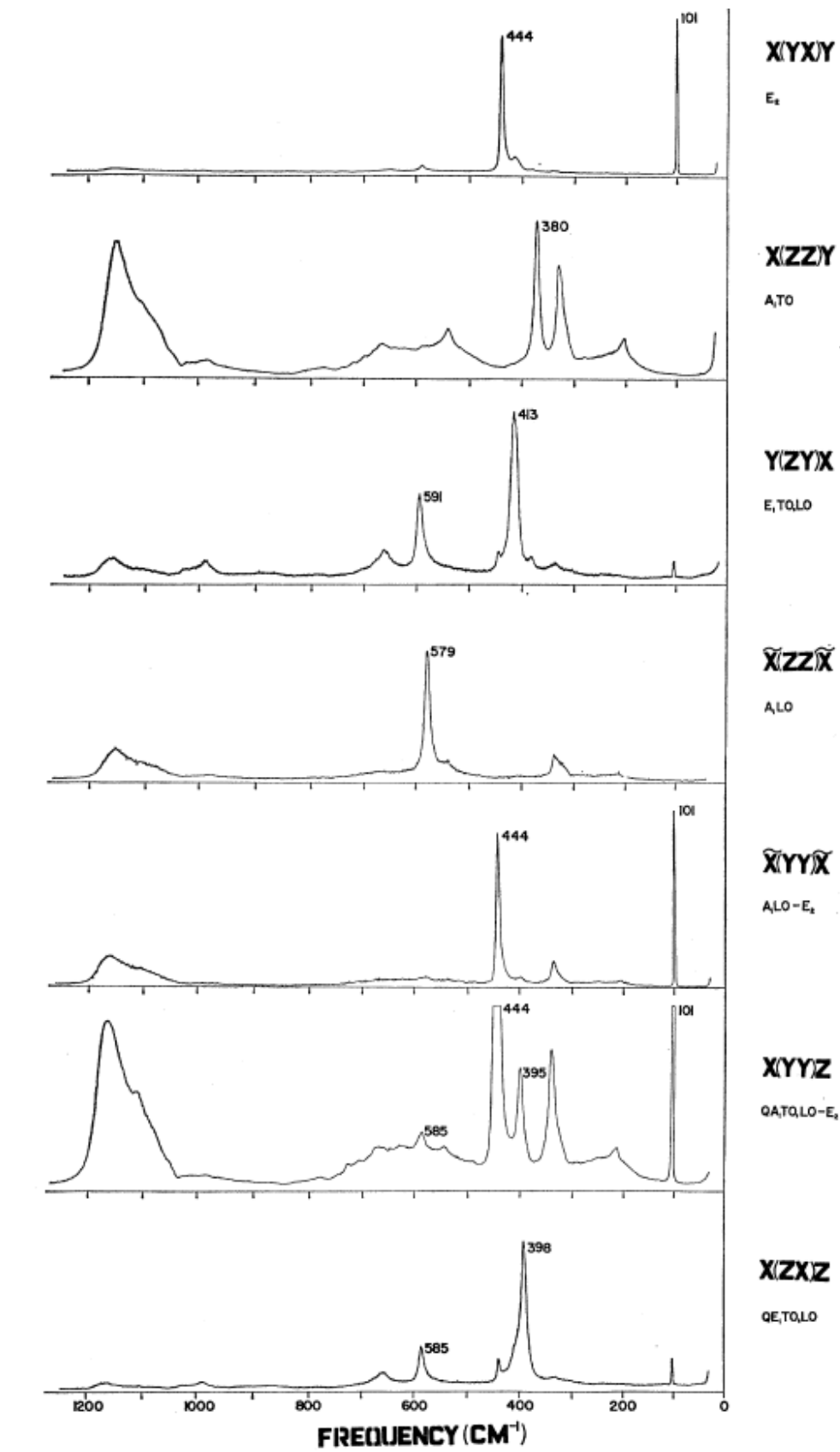


Figure 42 The Raman spectra of back scattering, near forward scattering and right angle scattering modes [82].

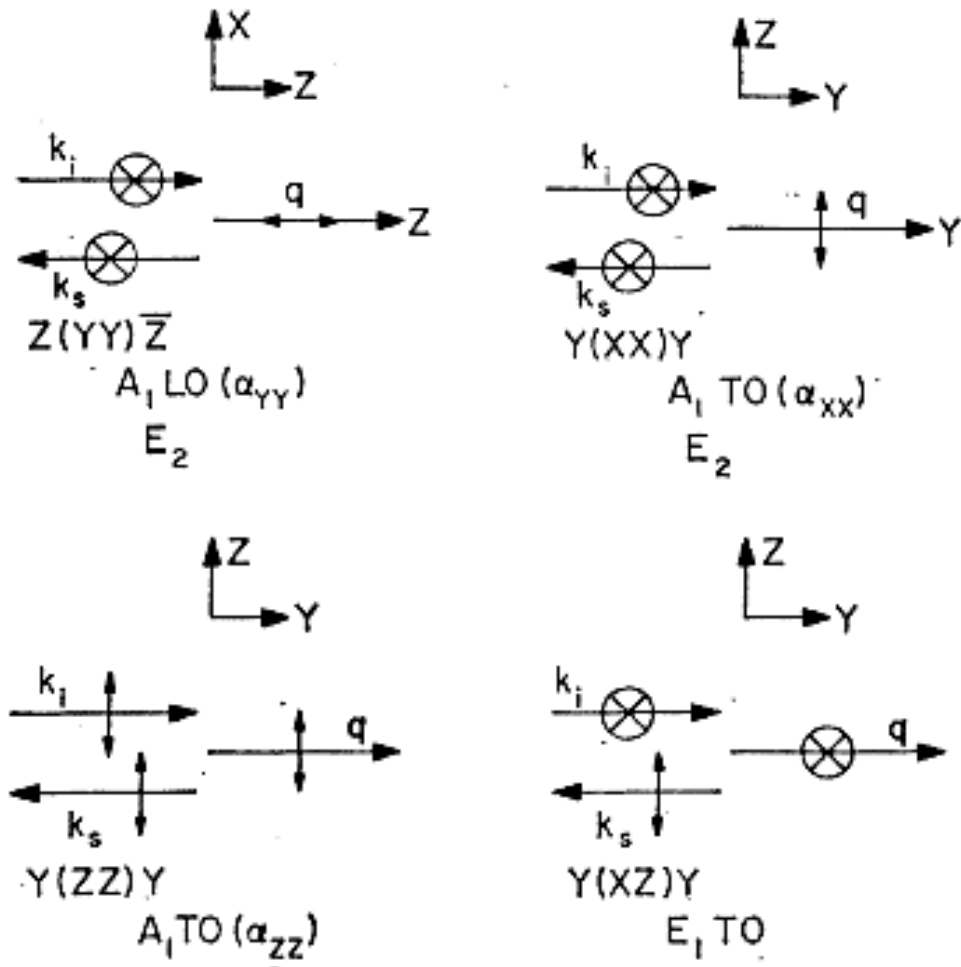


Figure 43 The backscattering diagram of wurtzite micro-Raman spectrum: (a) input-output z axis $[0001]$, (b, c and d) input-output a-axis $[10\bar{1}0]$ [82].

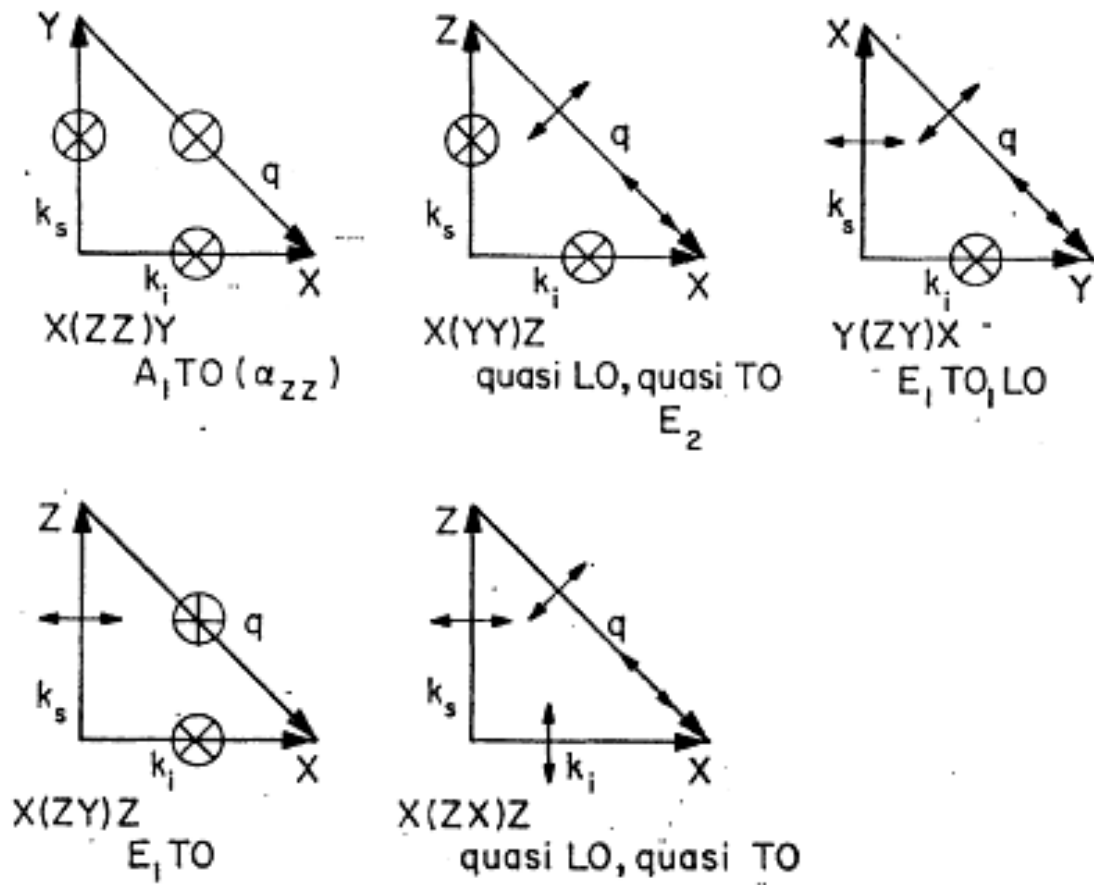


Figure 44 The right angle scattering diagram of wurtzite micro-Raman spectrum [82].

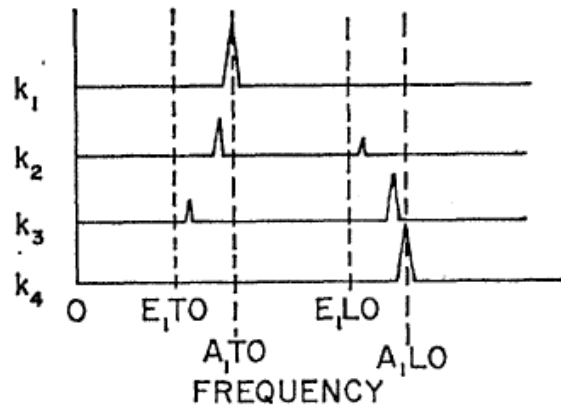
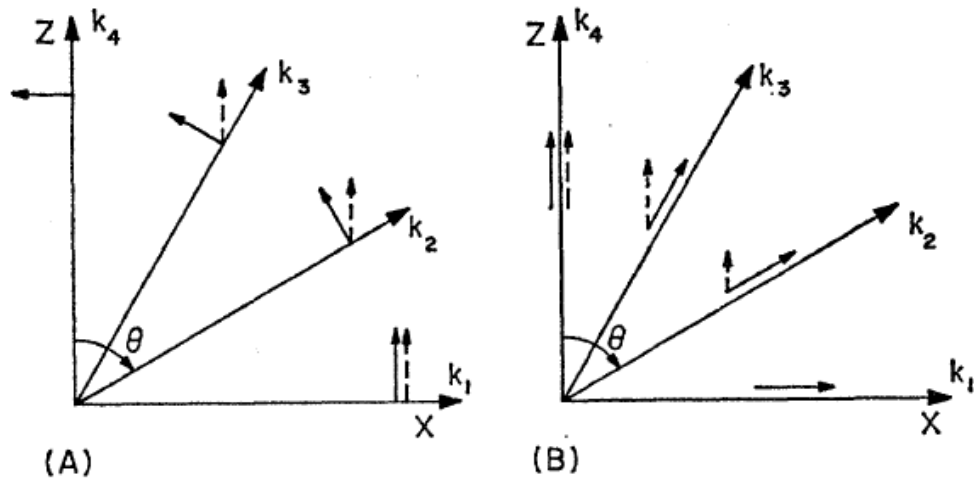


Figure 45 The E_1 phonon propagation in the (0001) plane. The transverse phonon is illustrated by the solid-line polarization vector, and the dashed line corresponds to the $(11\bar{2}0)$ polarization component of Raman spectrum. The k_2 and k_3 lines represent the quasi QA peak between the $E_{1(TO)}$ and $A_{1(TO)}$ peaks [82].

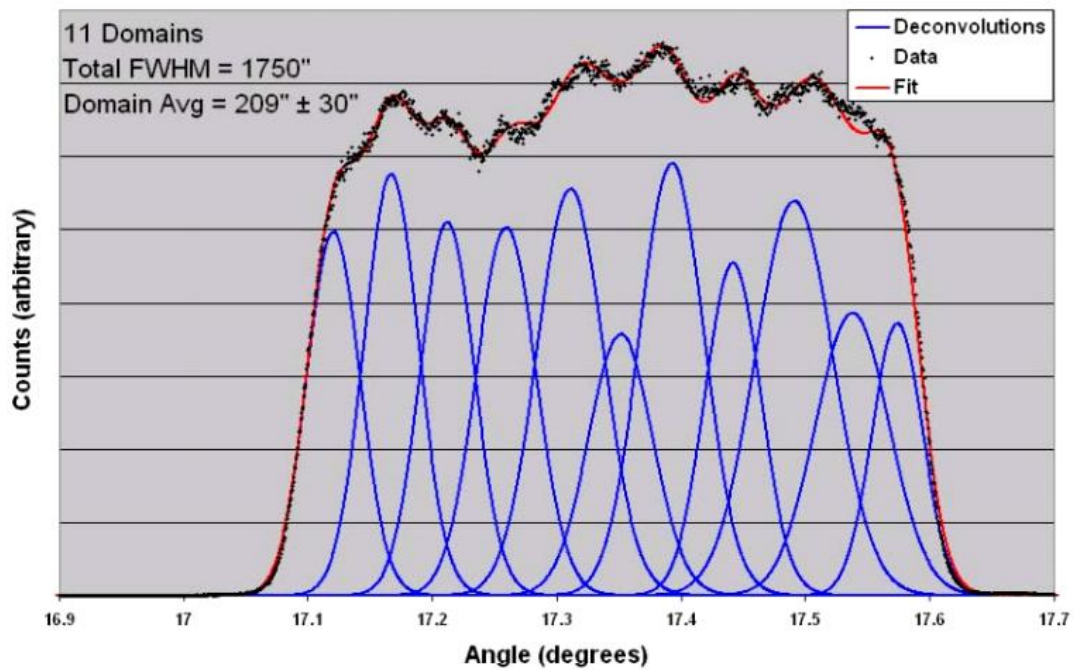


Figure 46 Deconvolution of c-plane GaN XRD rocking curve (0002) Peaks [80, 96].

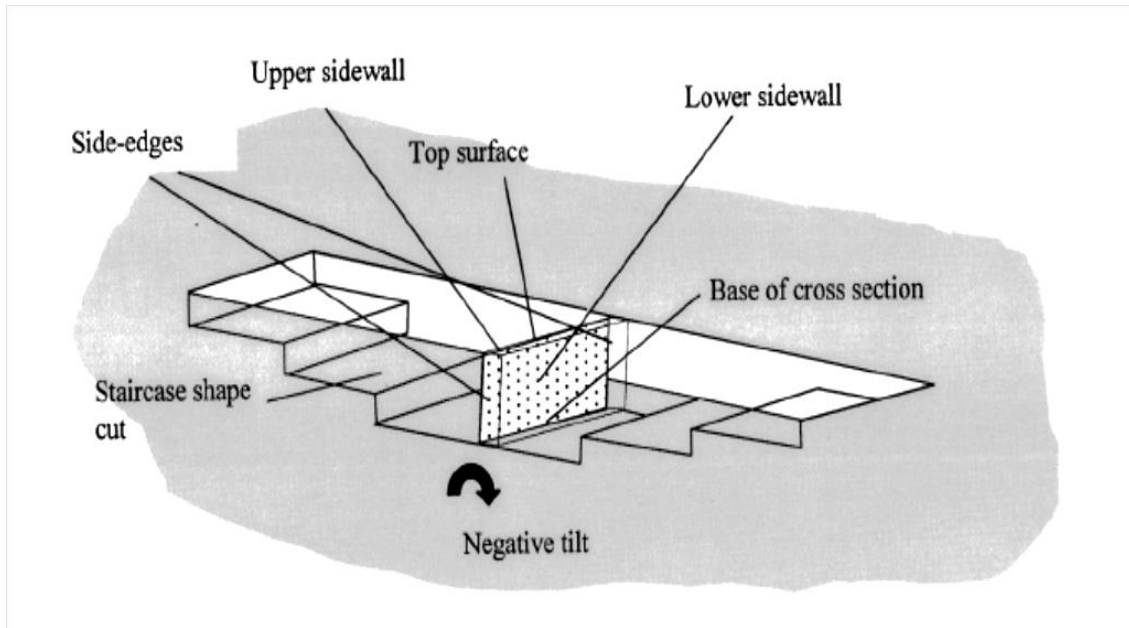
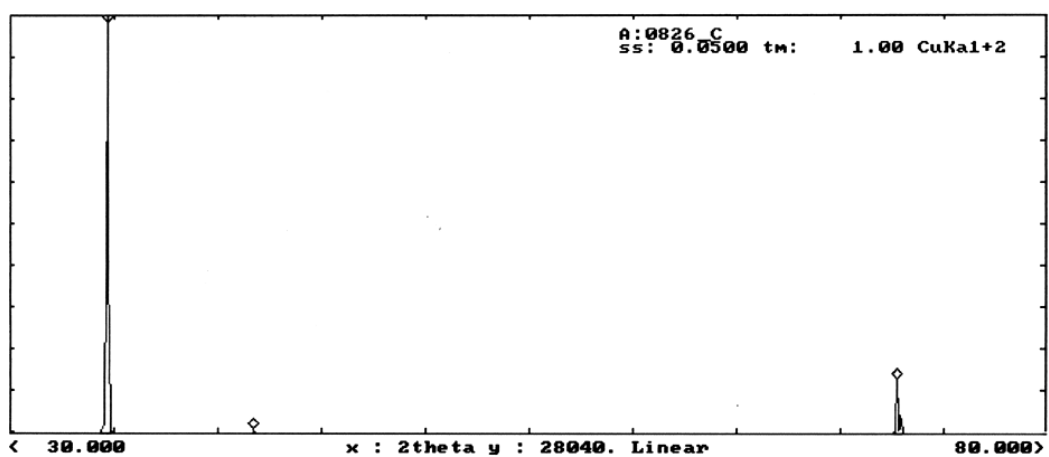


Figure 47 Schematic illustration of TEM sample procedure using FIB [97].

Sample: A:0826_C
Data file: A:GAN-1.RAW

26-Aug-2008 12:34:35

Seq	2theta	d	rel. I	Seq	2theta	d	rel. I
1	34.620	2.5894	100.00	1	34.620	2.5894	100.00
2	41.700	2.1647	0.68 ?	3	72.860	1.2974	12.71
3	72.860	1.2974	12.71	2	41.700	2.1647	0.68 ?



?help Zoom Match File Clear Back. Null K a2 Peaks Smoo. Comp. Wfile -> P

Figure 48 The XRD pattern shows GaN has a shark peak located at $2\theta=34.62^\circ$.

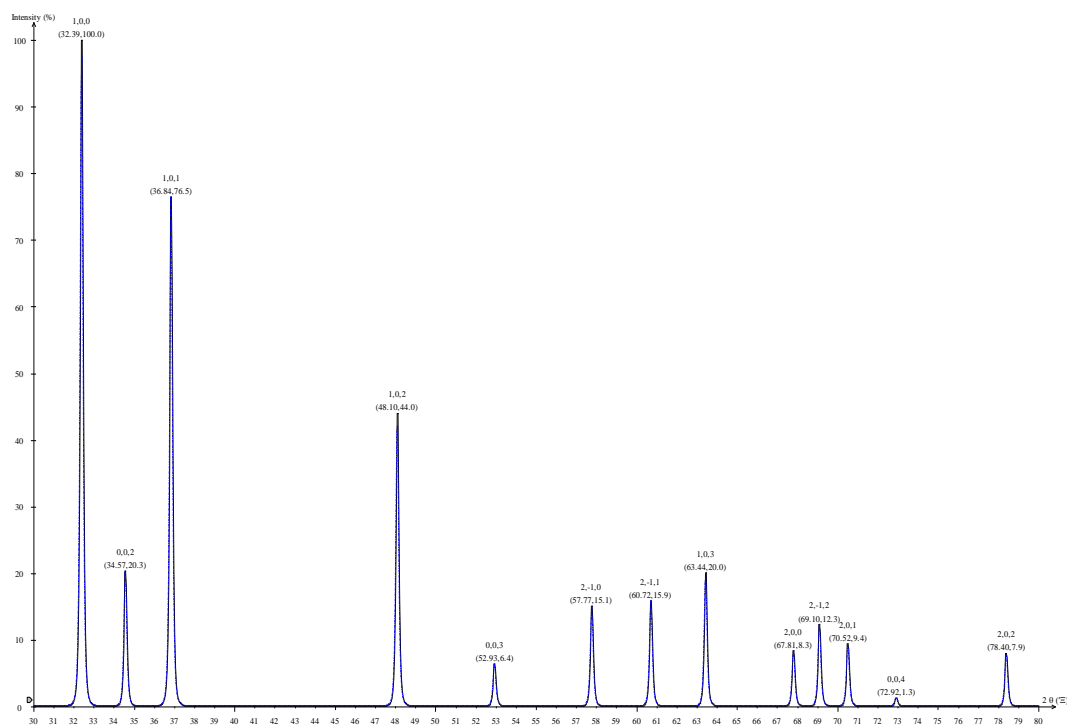
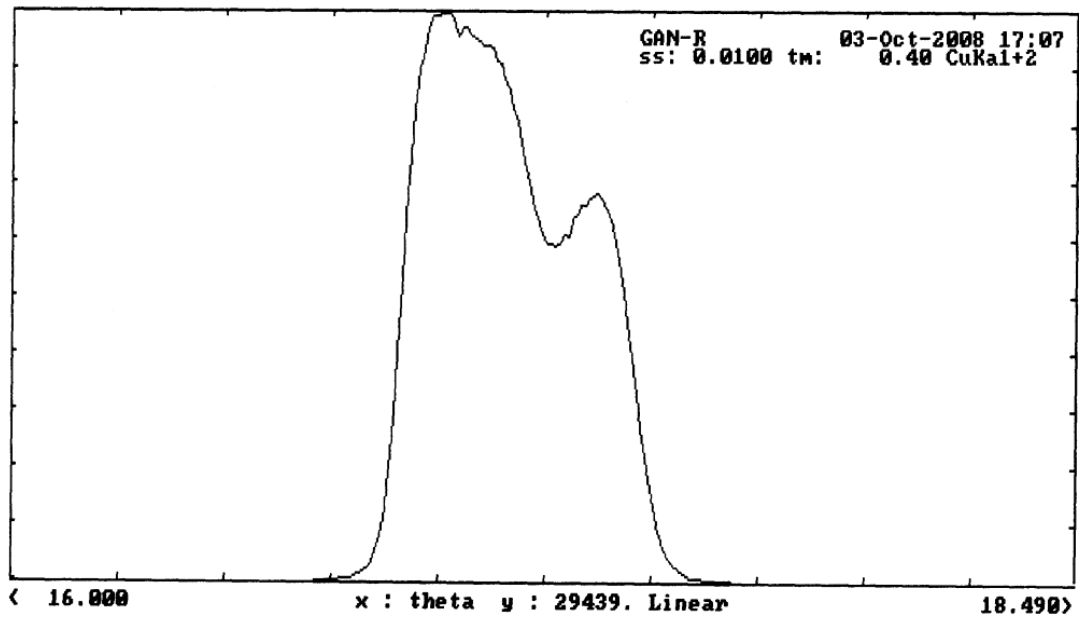


Figure 49 The XRD pattern of GaN estimate by CaRine software.



?help Zoom Match File Clear Back. Null K a2 Peaks Smoo. Comp. Wfile -> ?

Figure 50 The XRD Rocking curve pattern shows a broad peak ranging from 16.45° to 17° with full width of middle height (FWMH) = 0.341° .

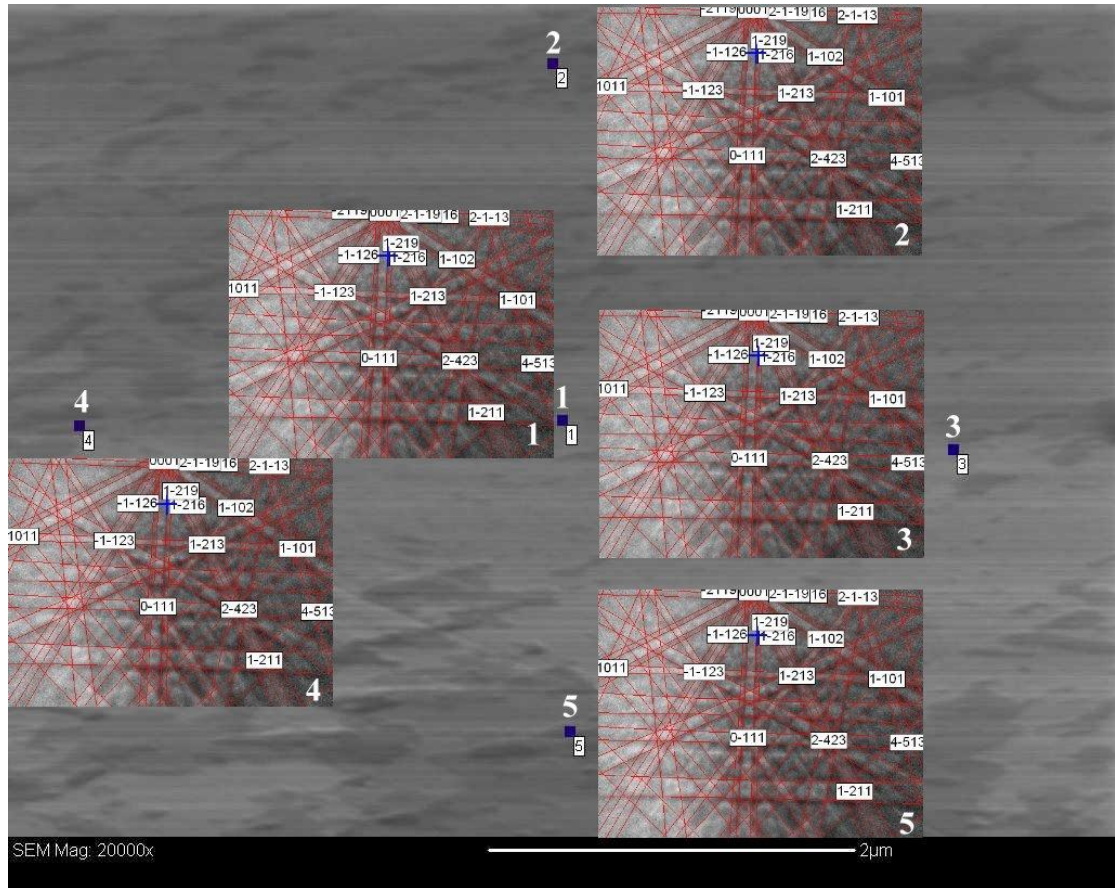


Figure 51 The EBSD patterns and SEM SEI image of c-plane ZnO.

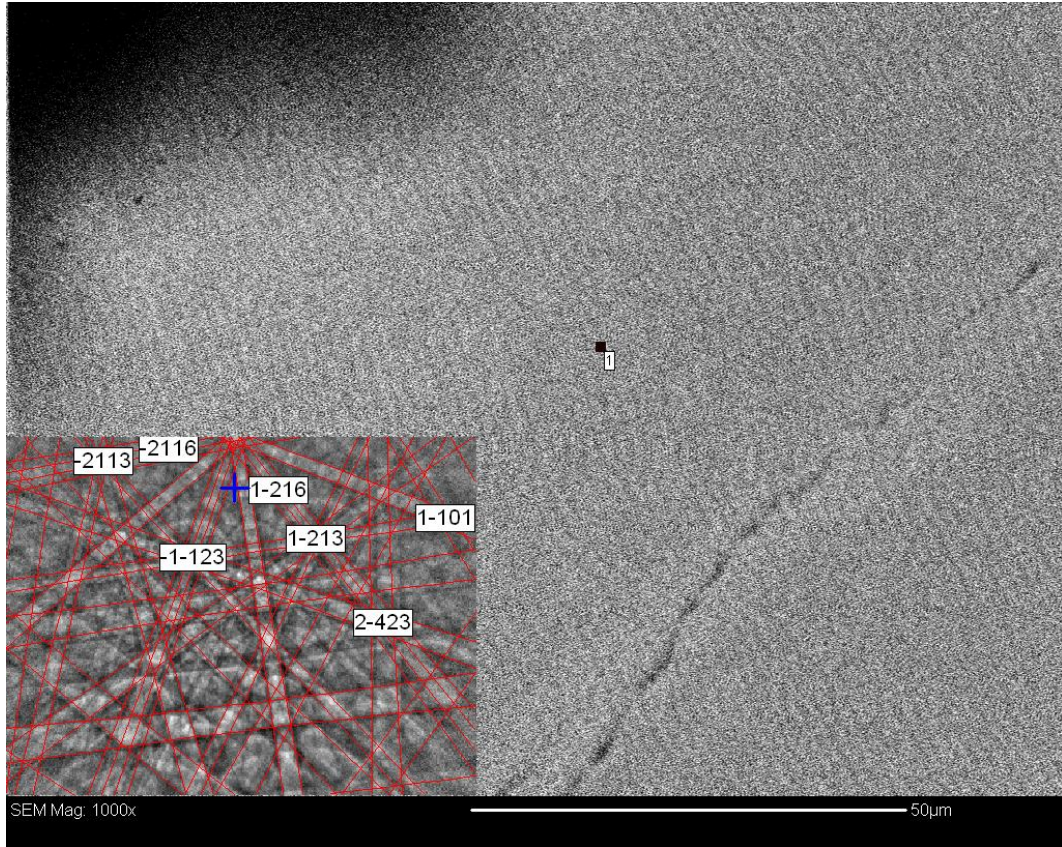


Figure 52 The EBSD pattern and SEM SEI image of c-plane GaN.

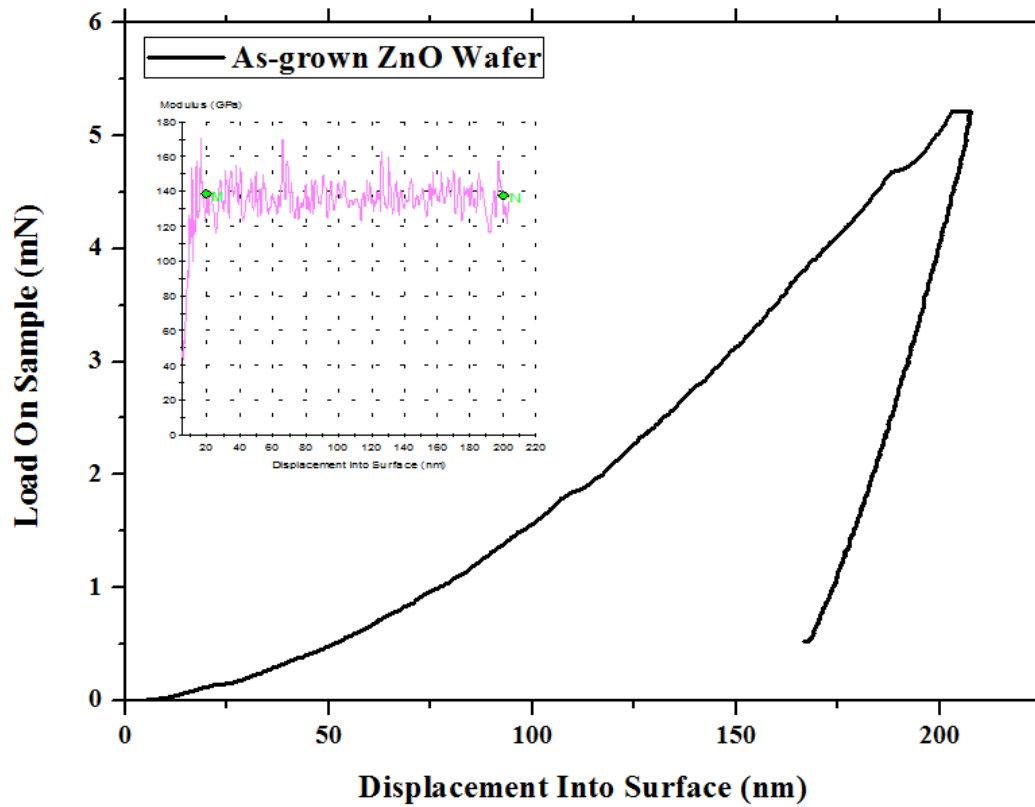


Figure 53 Showing the load-displacement and modulus-depth curves of c-plane ZnO at CSM constant displacement rate mode.

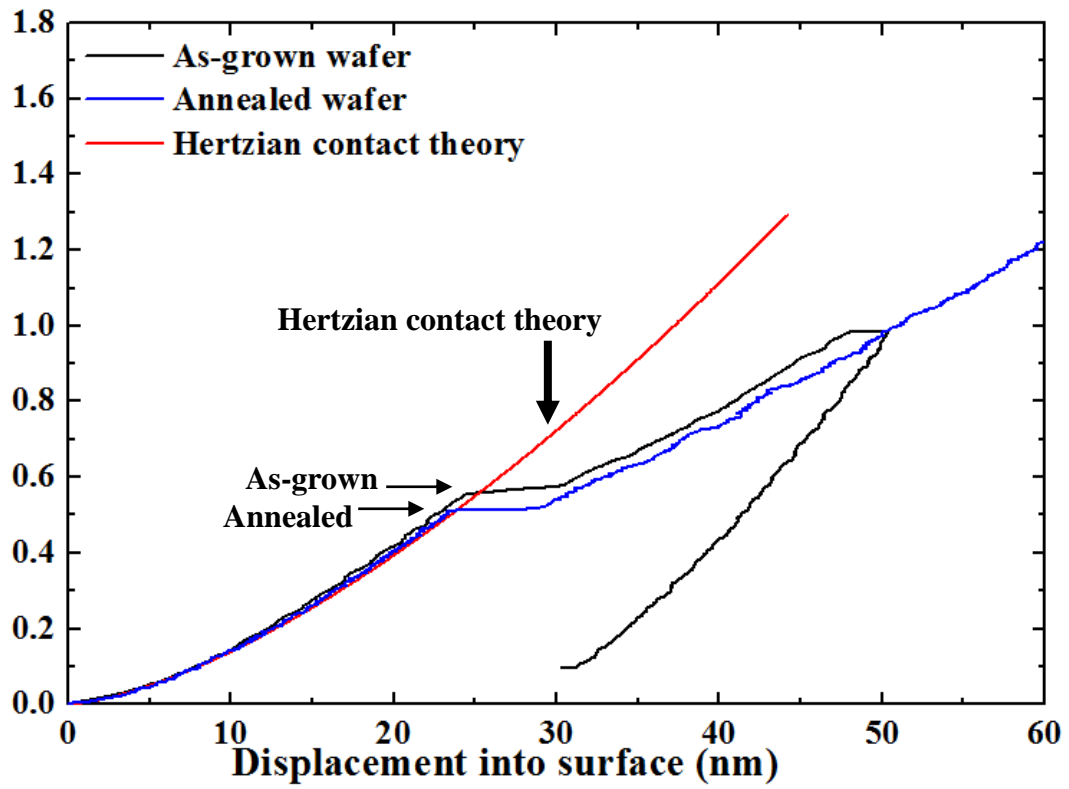


Figure 54 Representative nanoindentation load-displacement curves of the as-grown, annealed wafer and the curve predicted by the Hertzain contact theory.

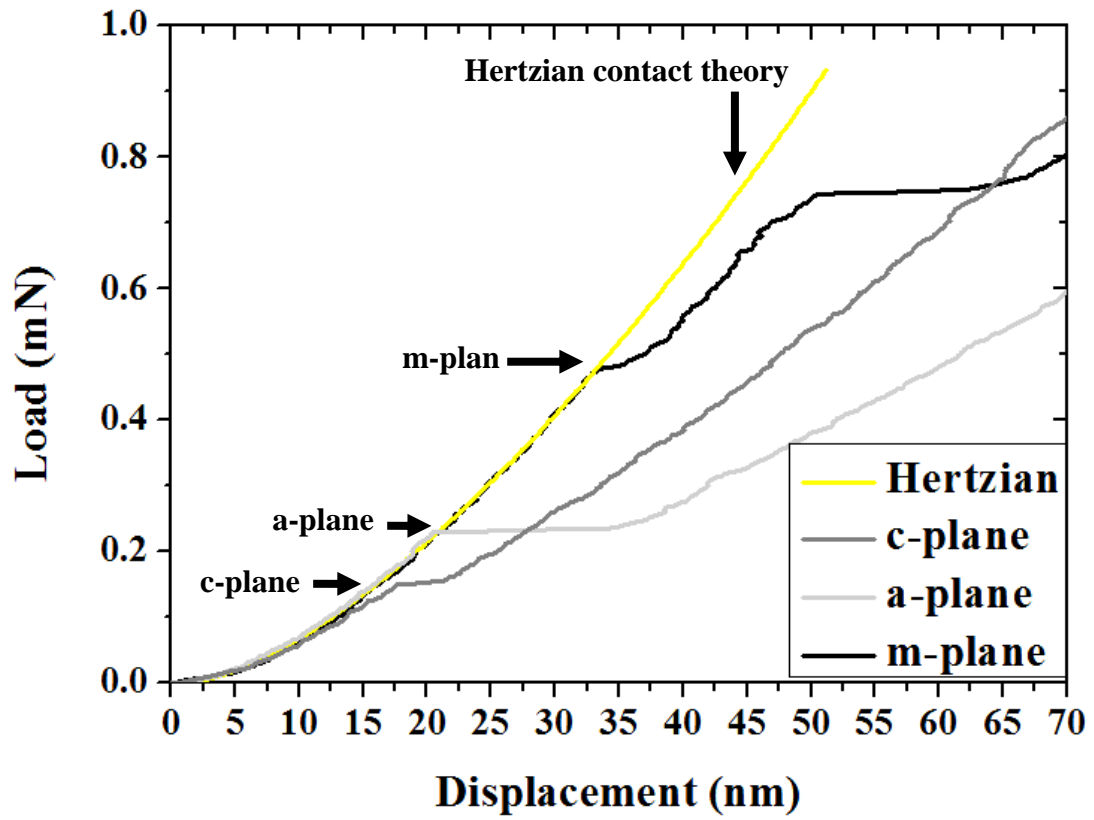


Figure 55 Representative nanoindentation load-displacement curves of the c-plane, a-plane, m-plane ZnO wafer and the curve predicted by the Hertzain contact theory.

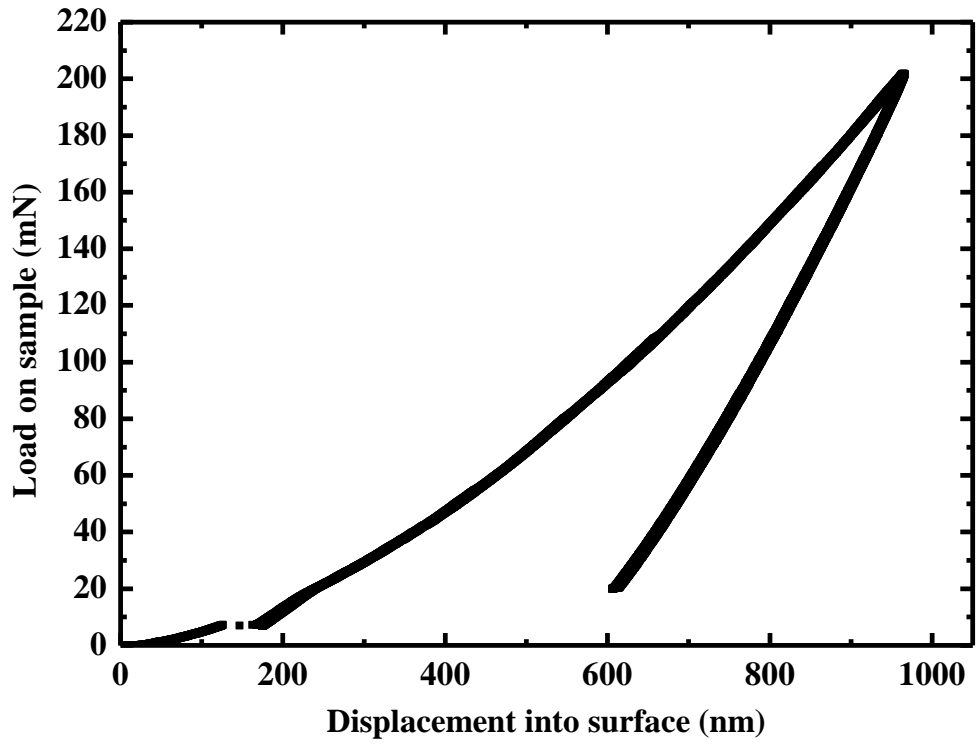


Figure 56 Showing the data of c-plane GaN CSM mode depth 1000 nm nanoindentation testing.

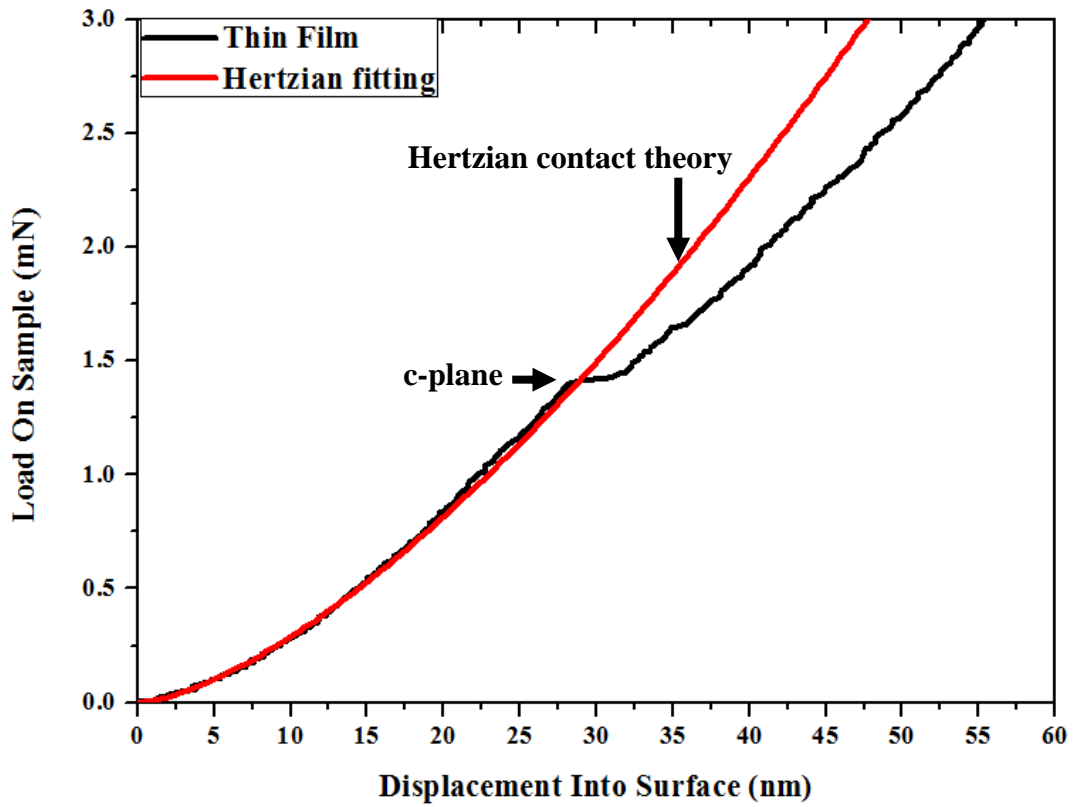


Figure 57 Showing the first pop-in data of CSM mode depth 500 nm (~10% to total thickness) indentation testing.

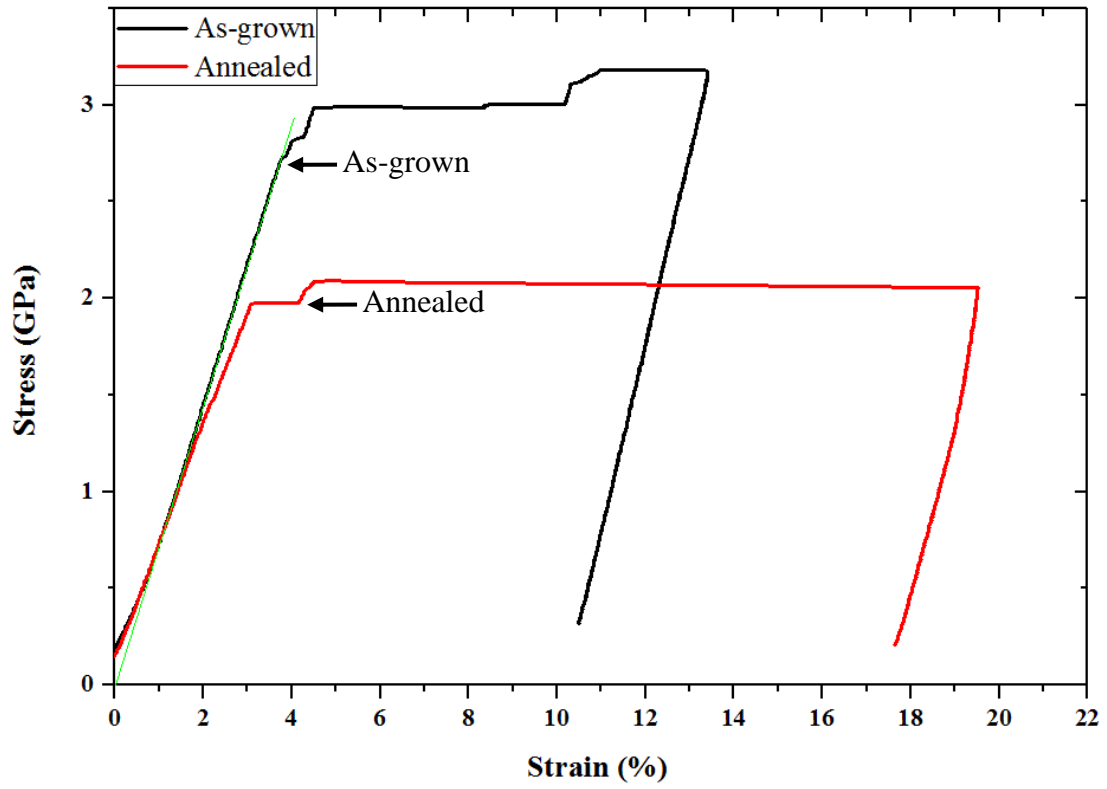


Figure 58 The representative as-grown preset 300 nm pillar and the annealed preset 300 nm pillar stress-strain curves of microcompression testing.

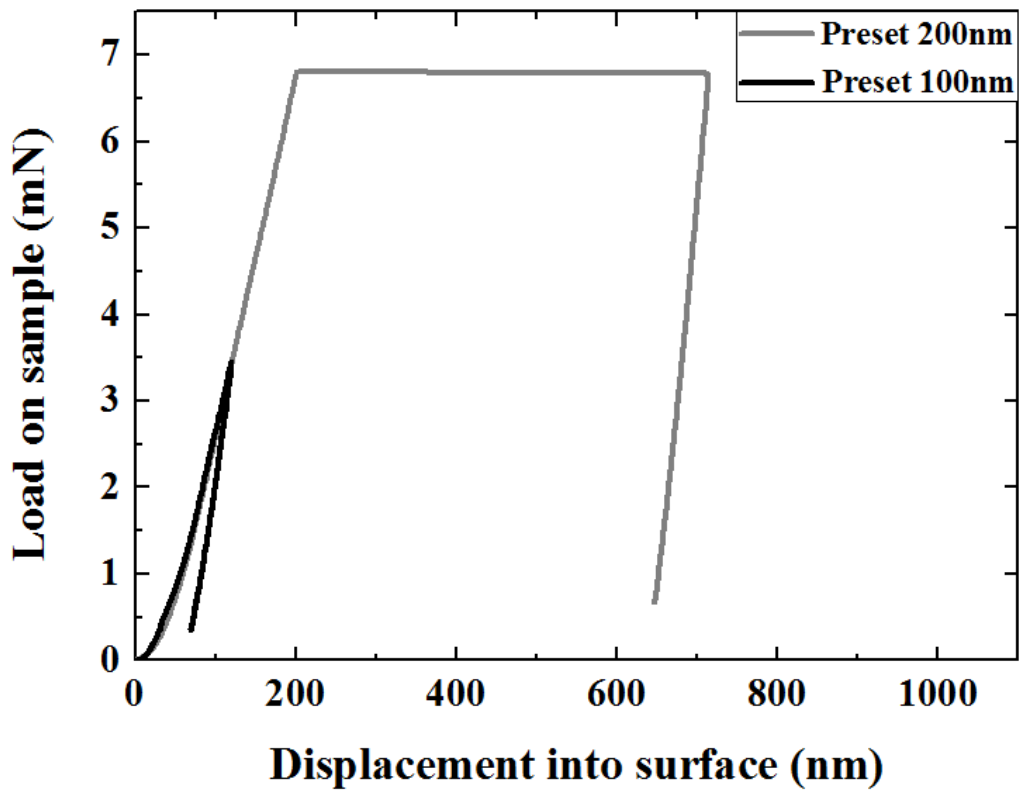


Figure 59 Representative load-displacement curves for microcompression of c-plane GaN micropillars.

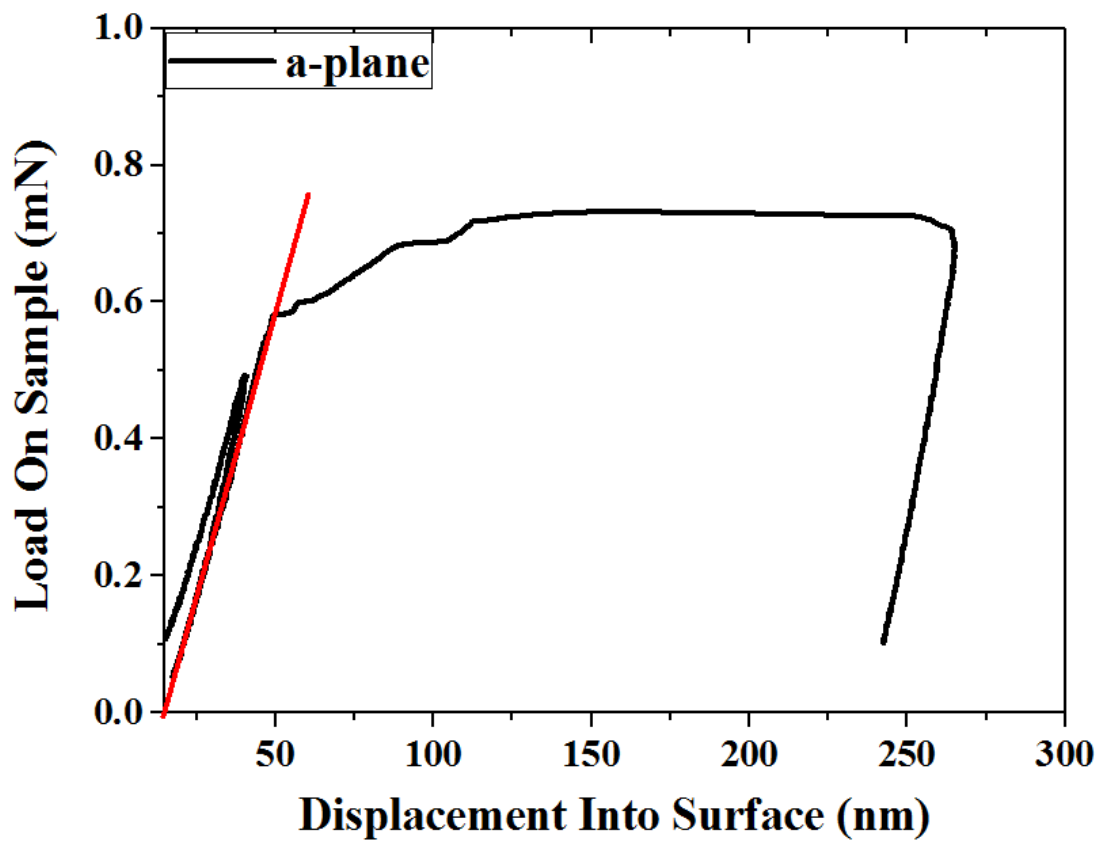


Figure 60 Representative load-displacement curve for microcompression of a-plane ZnO micropillars.

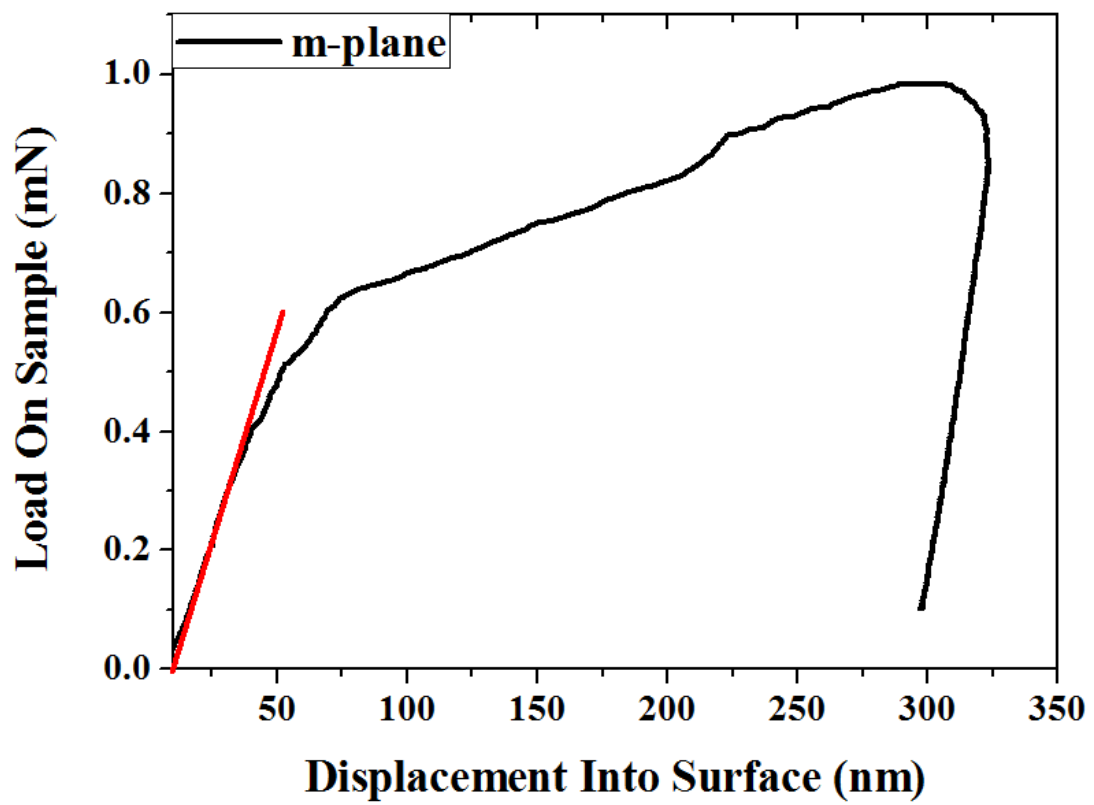


Figure 61 Representative load-displacement curve for microcompression of m-plane ZnO micropillars.

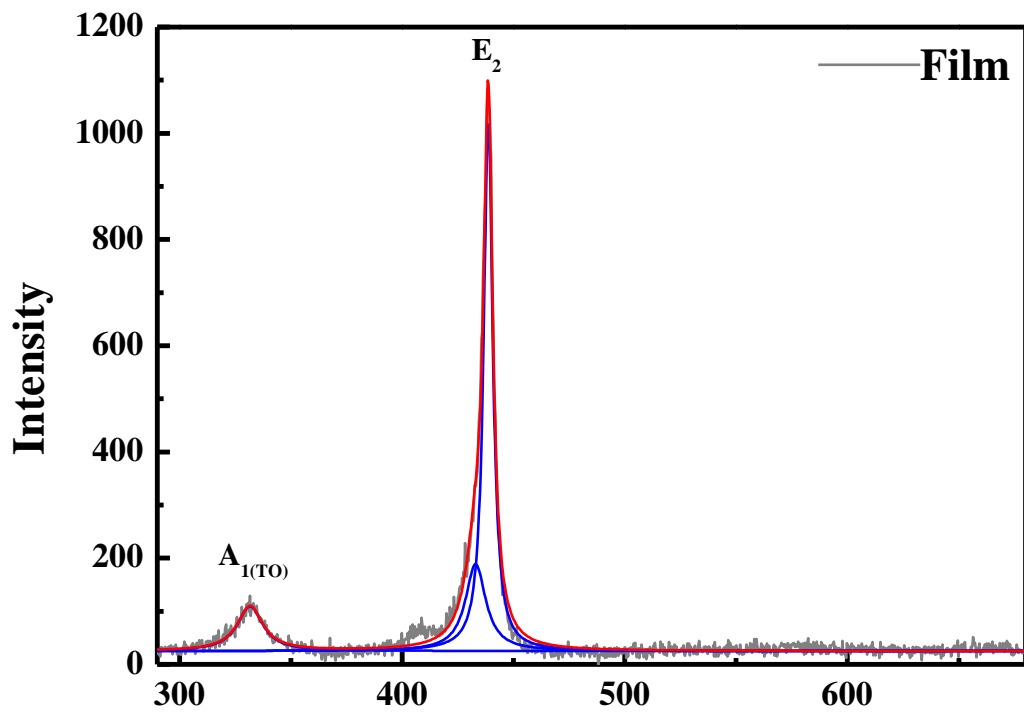


Figure 62 The recorded data and Gaussian fitting Raman spectra of film ZnO.

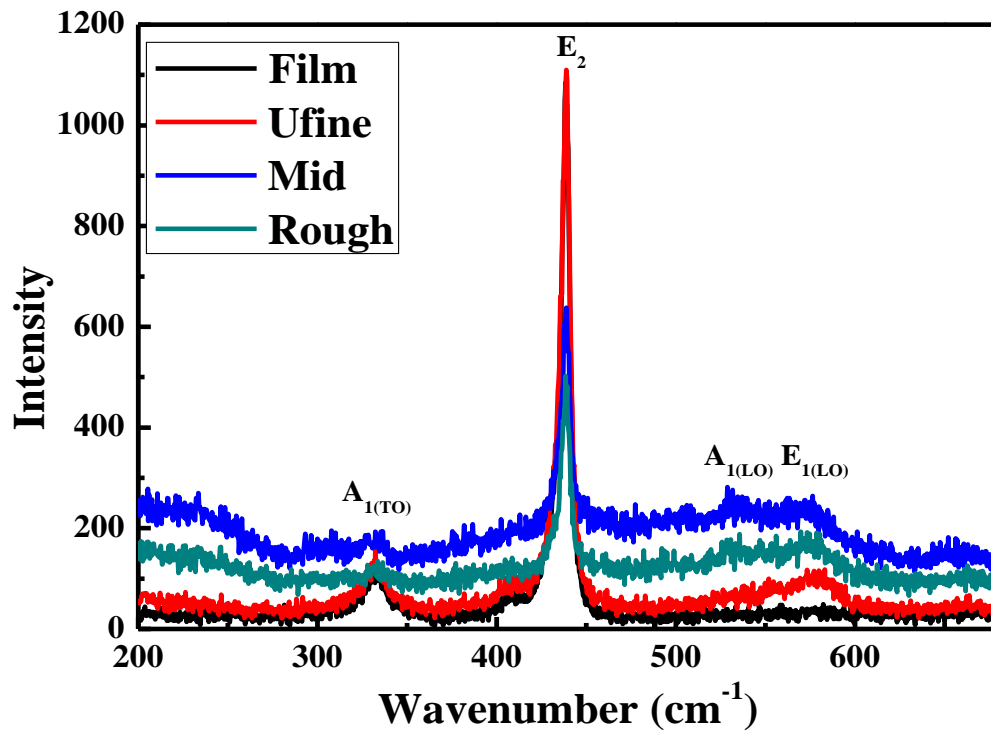


Figure 63 The Raman spectra of ZnO after Ufine, middle and rough beam FIB Ga implanted conditions.

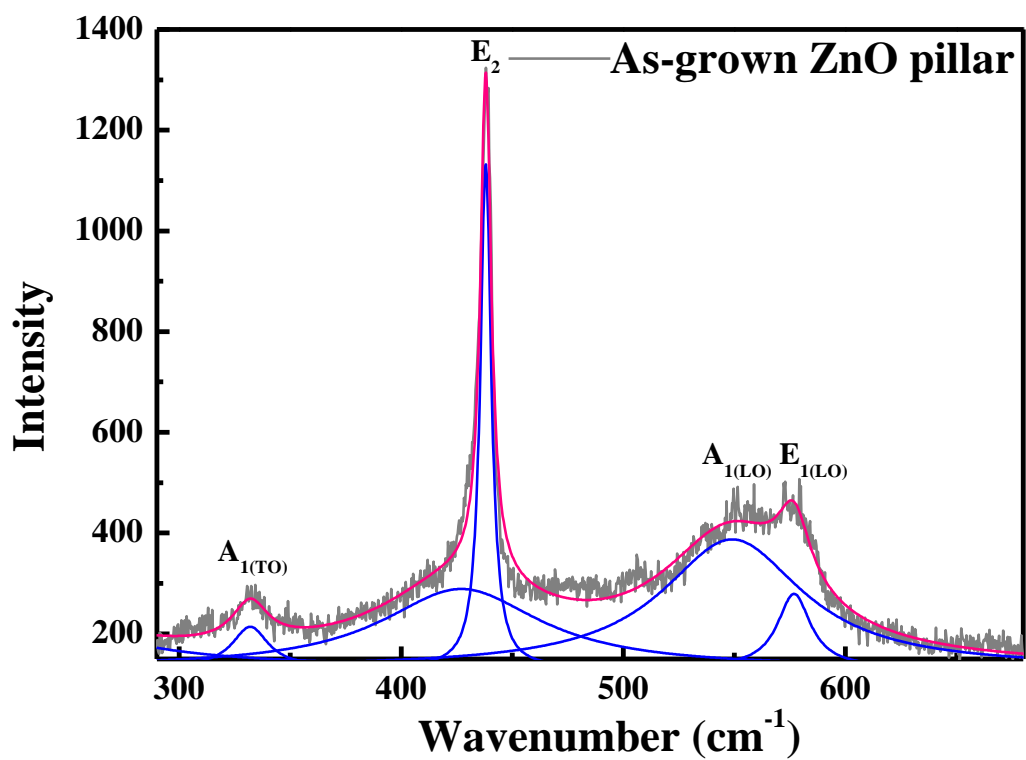


Figure 65 The recorded data and Gaussian fitting Raman spectra of As-grown ZnO pillar.

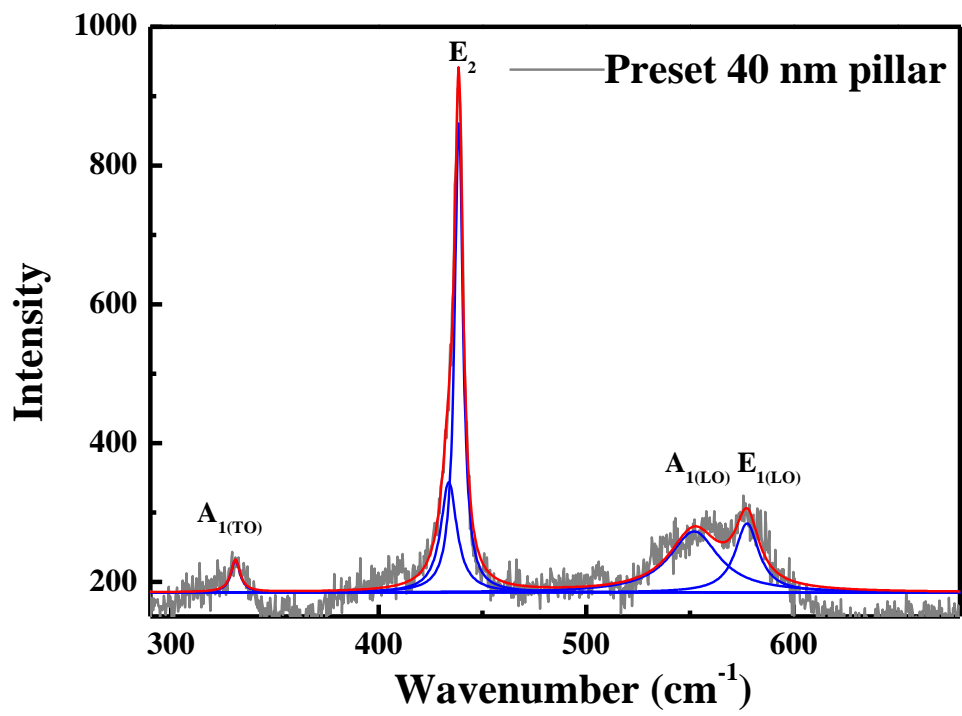


Figure 66 The recorded data and Gaussian fitting Raman spectra of preset 40 nm ZnO pillar.

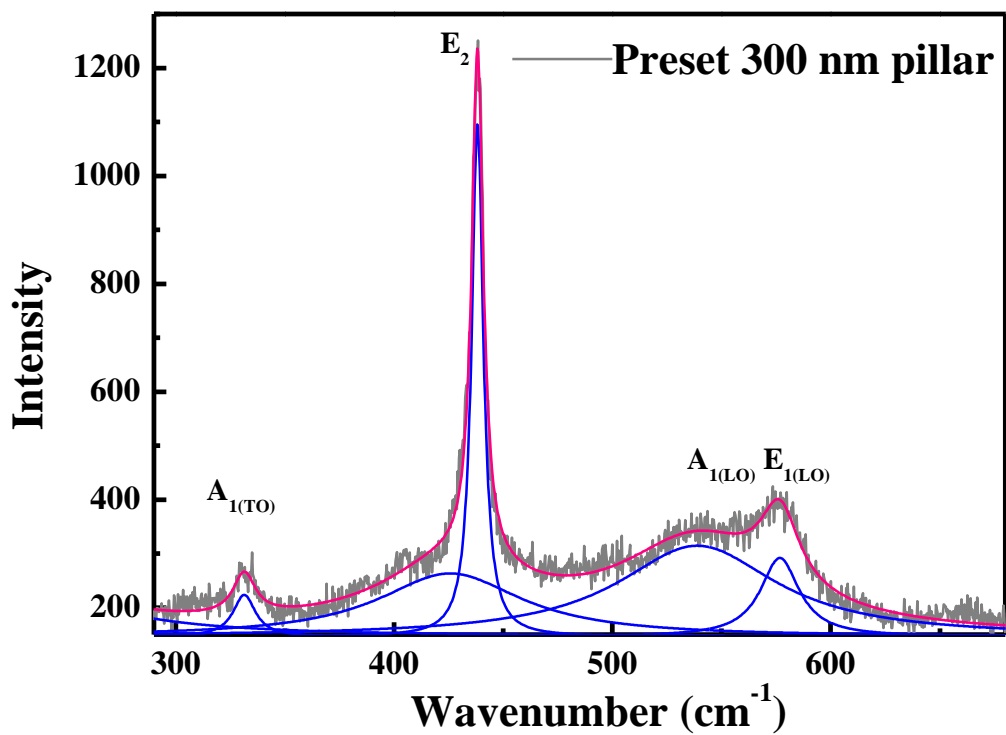


Figure 66 The recorded data and Gaussian fitting Raman spectra of preset 300 nm ZnO.

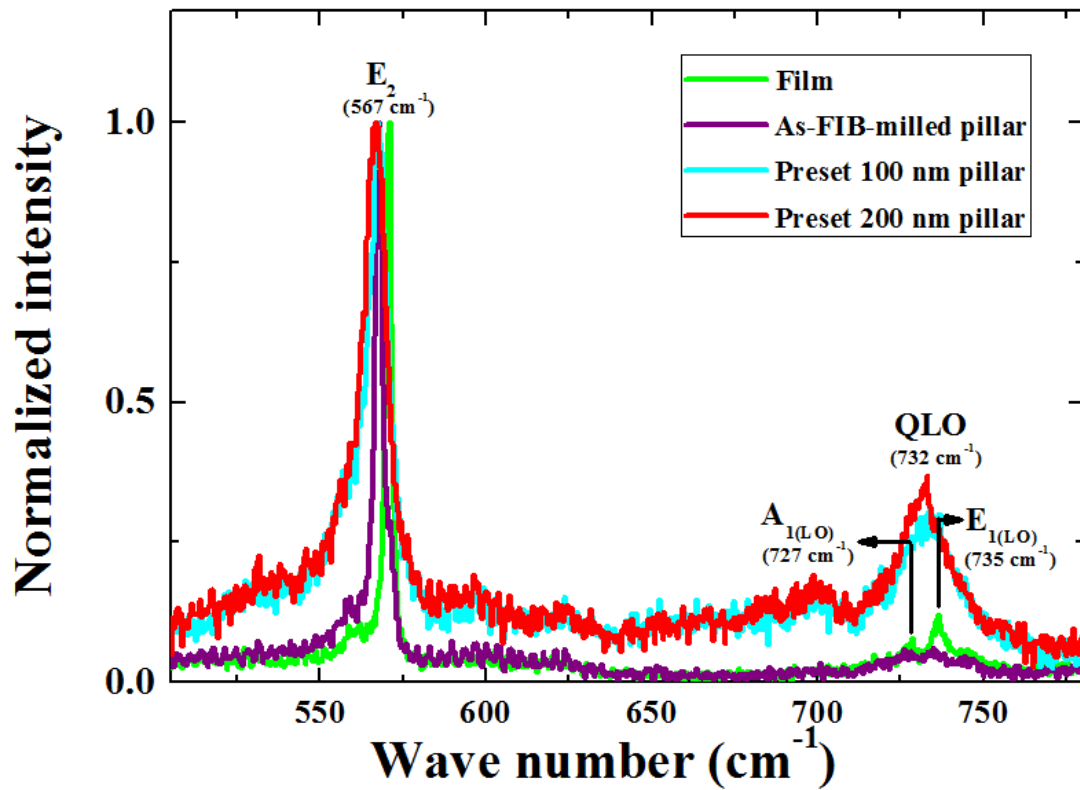


Figure 67 The recorded Raman spectra of GaN film, as-milled pillar, preset 100 nm pillar and preset 200 nm pillar.

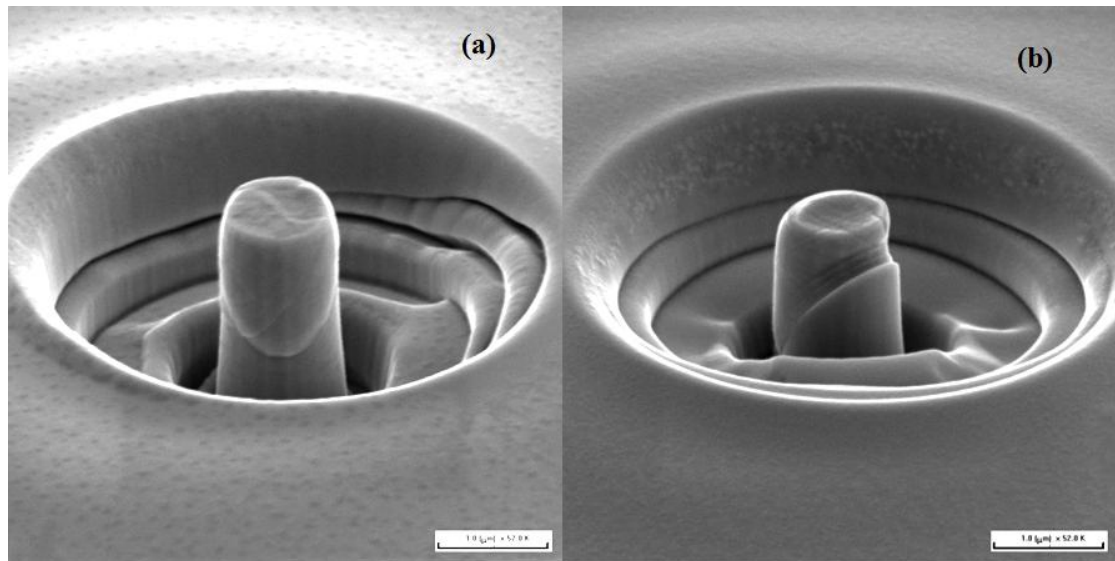


Figure 68 Showing the SEM image of (a) as-grown c-plane ZnO pillar and (b) annealed c- plane ZnO pillar after microcompression.

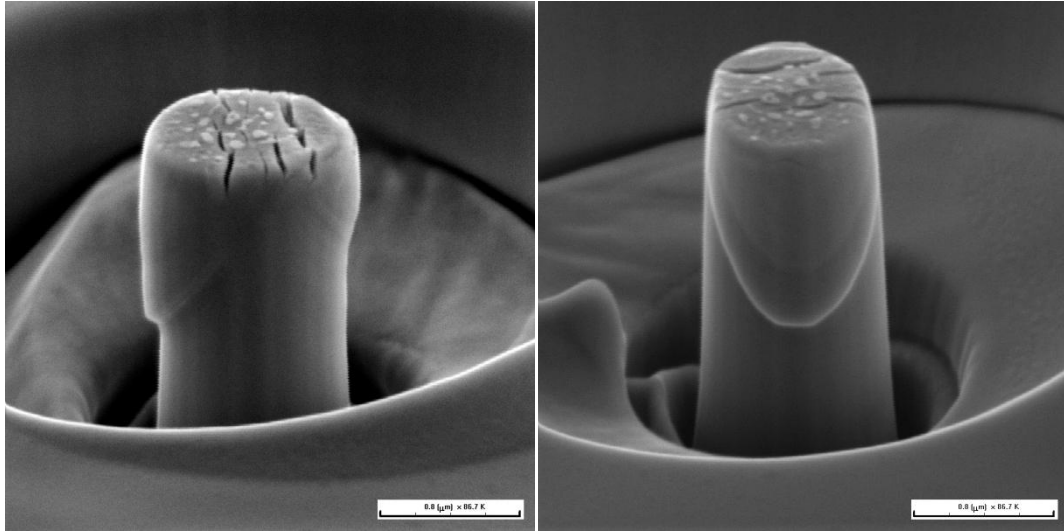


Figure 69 Showing the SEM image of m-ZnO pillar after microcompression.

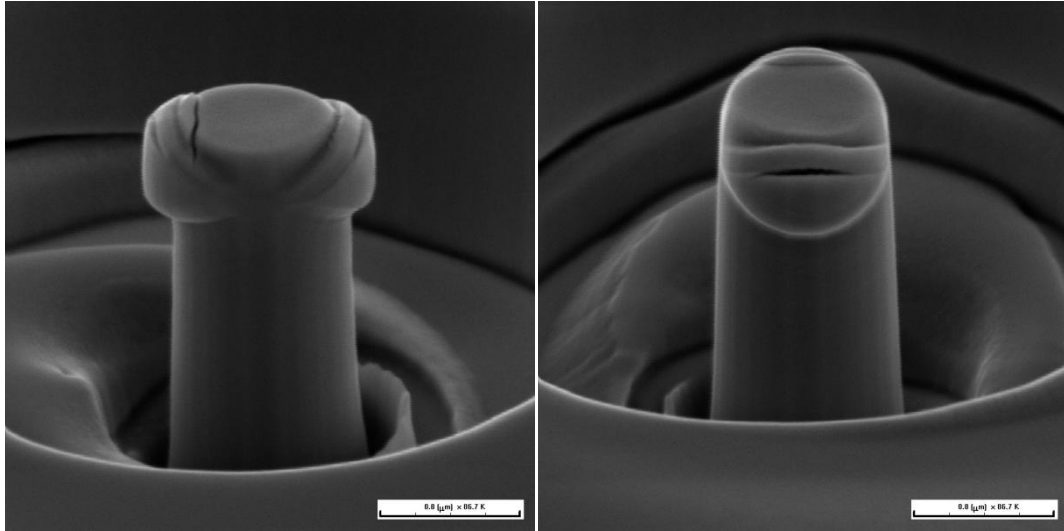


Figure 70 Showing the SEM image of a-ZnO pillar after microcompression.

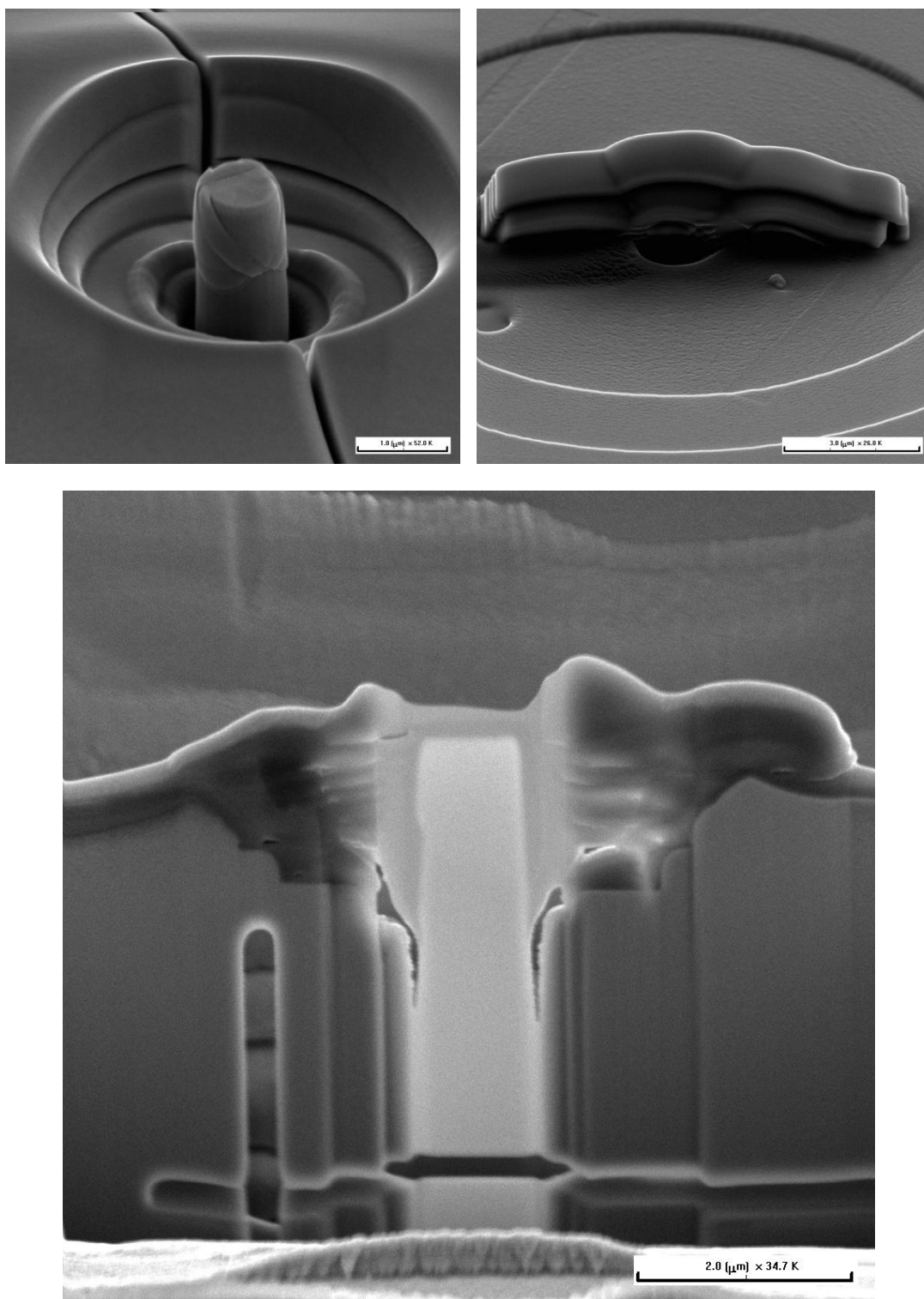


Figure 71 SEM images of (a) mark, (b) carbon protection layer and (c) side view of c-plane ZnO HR-XTEM sample.

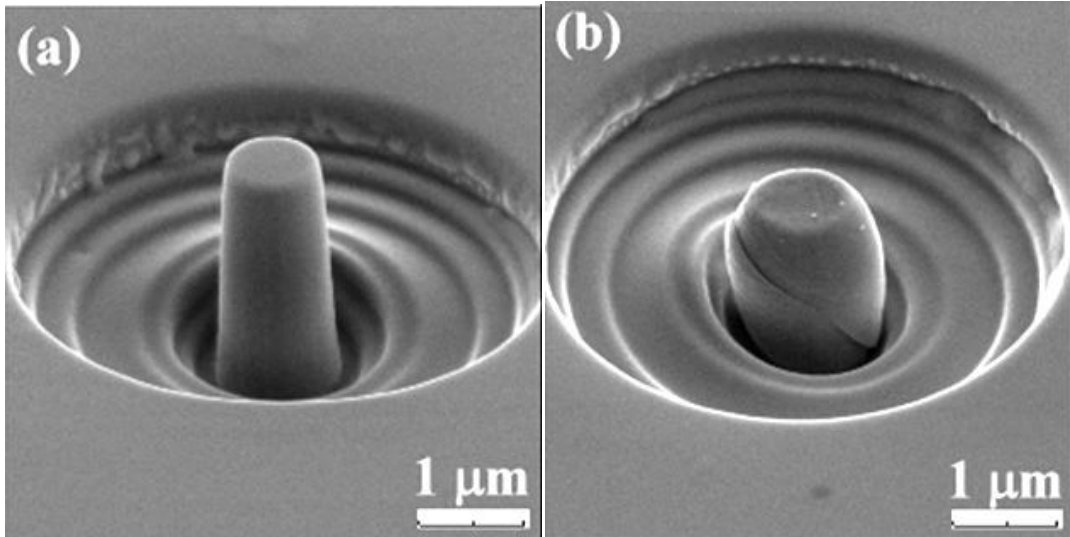


Figure 72 Representative c-plane GaN (a) 1 μm as-FIB-milled pillar SEM images and (b) first strain burst micropillar SEM image.

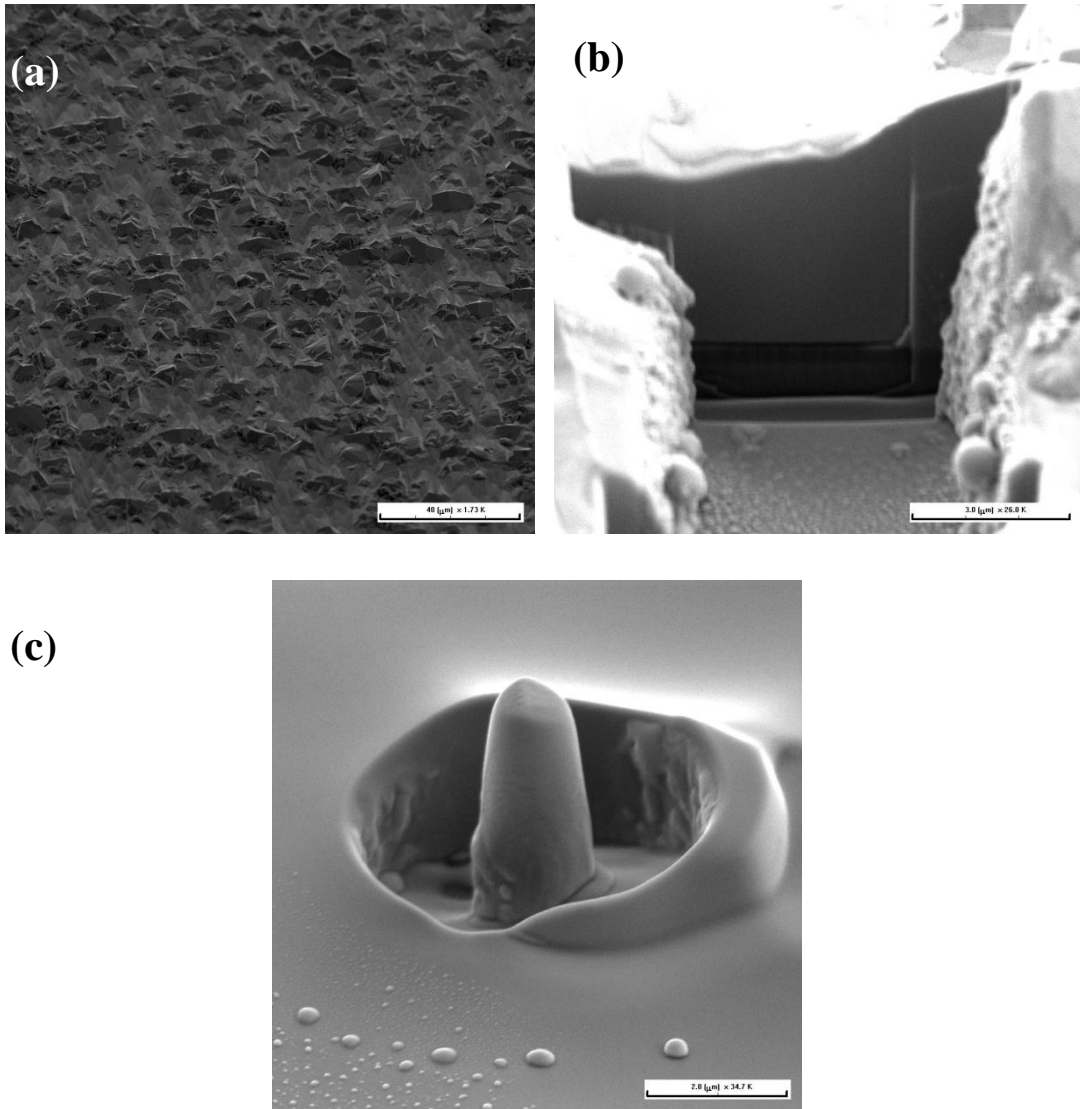


Figure 73 Showing the SEM image of (a) r-GaN thin film morphology, (b) cross section and (c) as-milled micropillar.

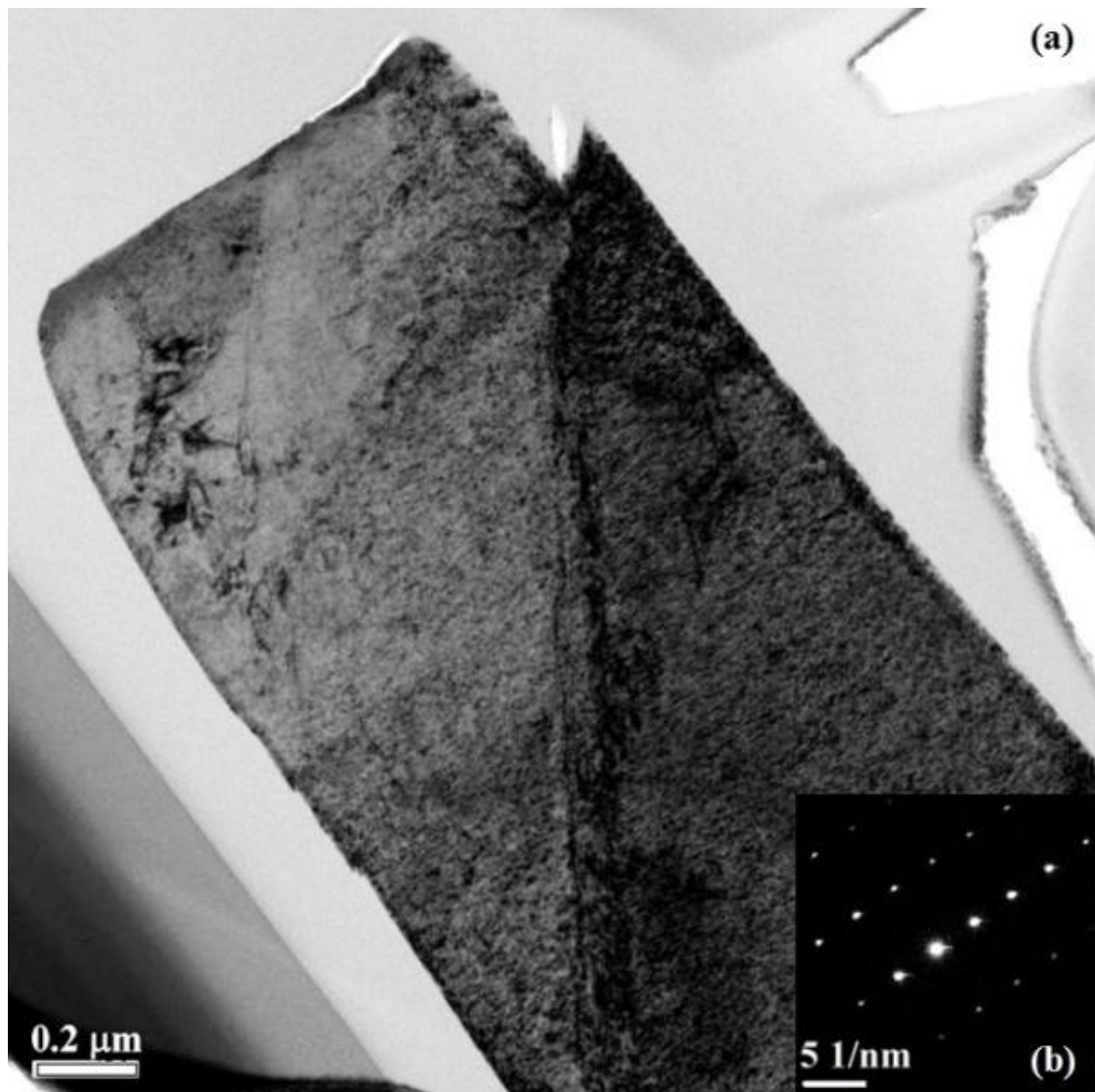


Figure 74 (a) XTEM bright field image of the ZnO micropillar compressed to a preset displacement of 300 nm, and (b) the associated selected area diffraction pattern, with an indexed zone axis of $[10\bar{1}0]$.

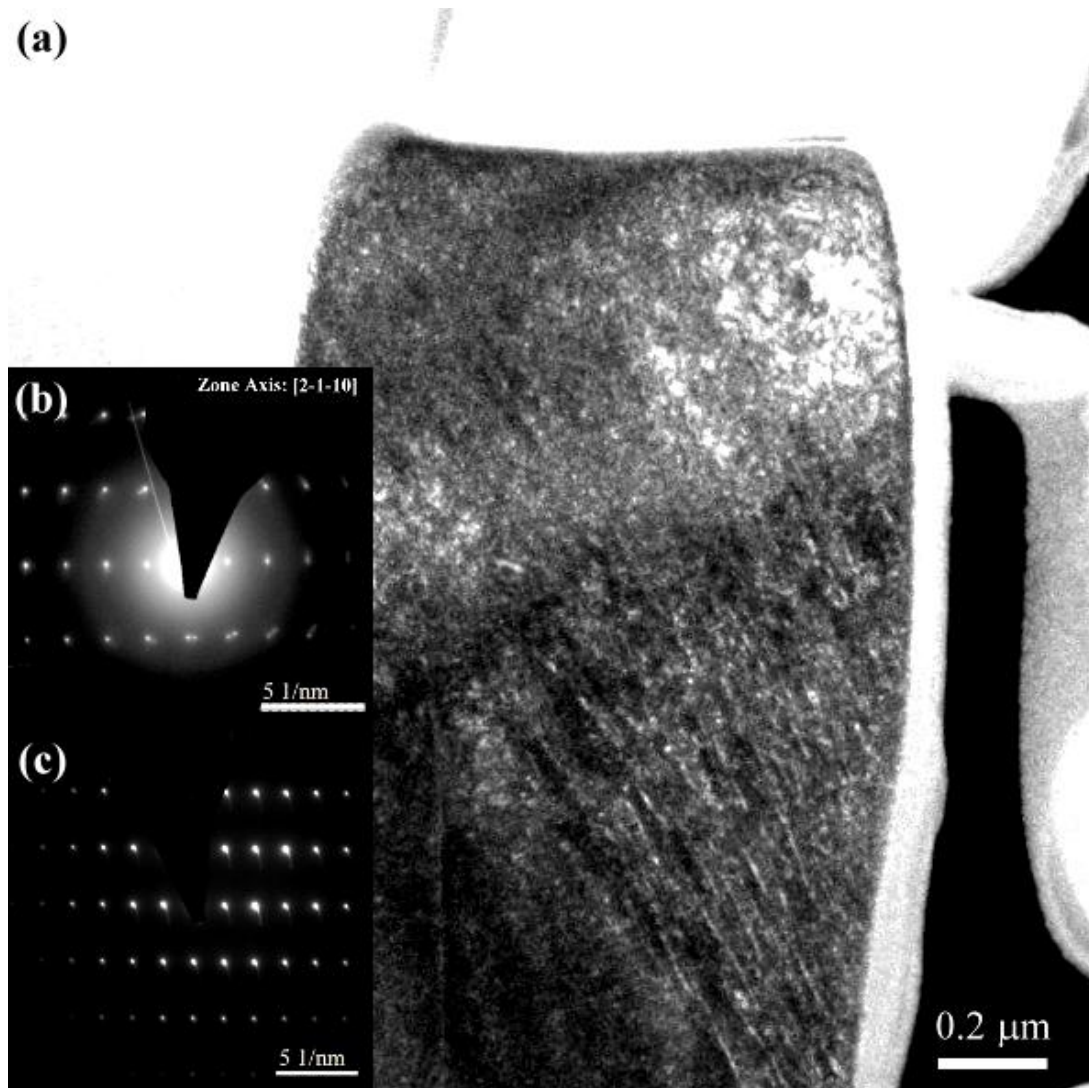


Figure 75 TEM characterization of the GaN micropillar compressed to a preset displacement of 200 nm: (a) bright field image from the longitudinal section, (b) selected area diffraction pattern for the upper region, and (c) selected area diffraction pattern for the lower region of the compressed pillar, with an indexed zone axis of $[10\bar{1}0]$.

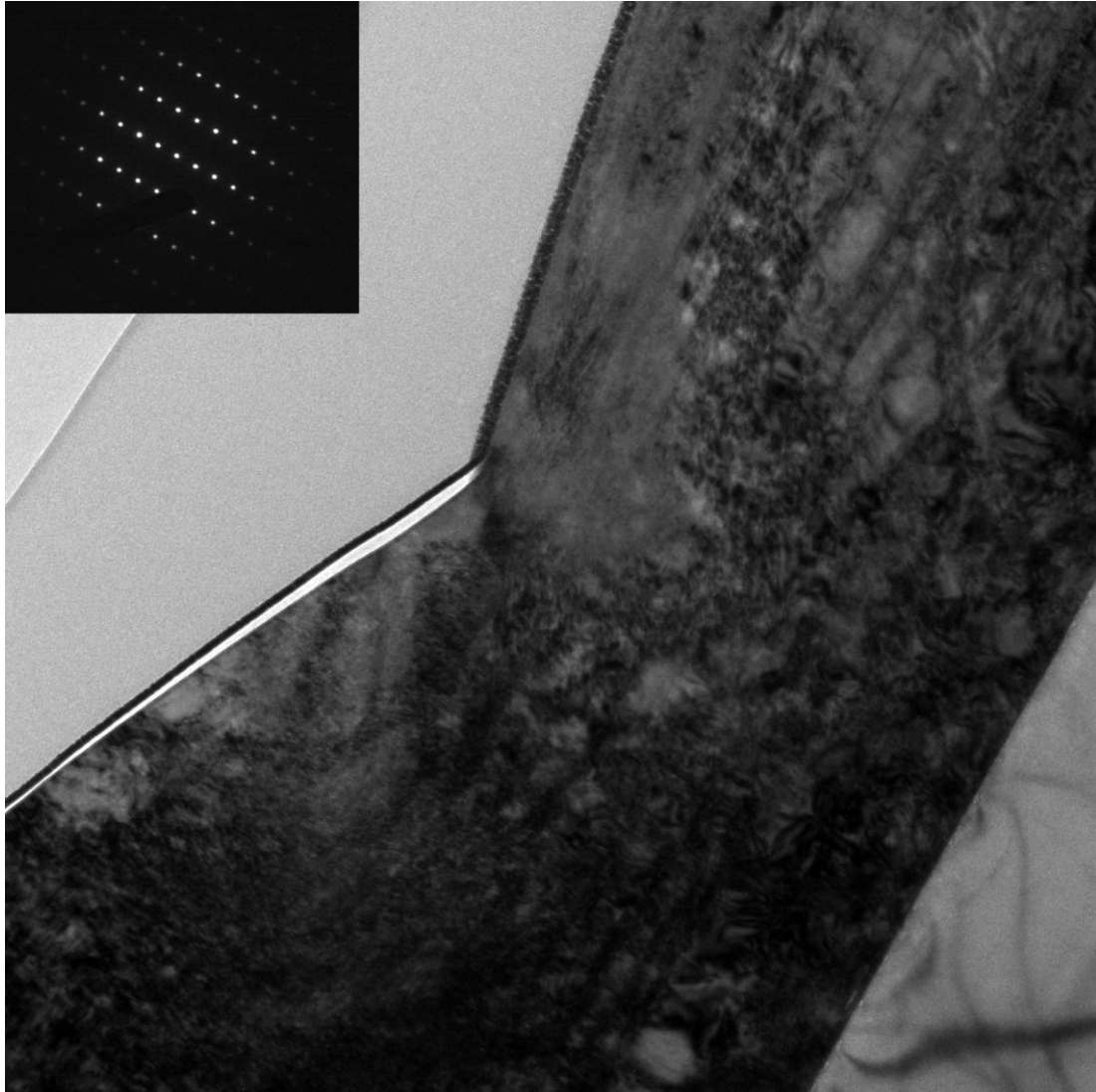


Figure 76 XTEM characterization of the 200 mN nanoindentation mark of the c-plane GaN thin film, with an indexed zone axis of $[10\bar{1}0]$.

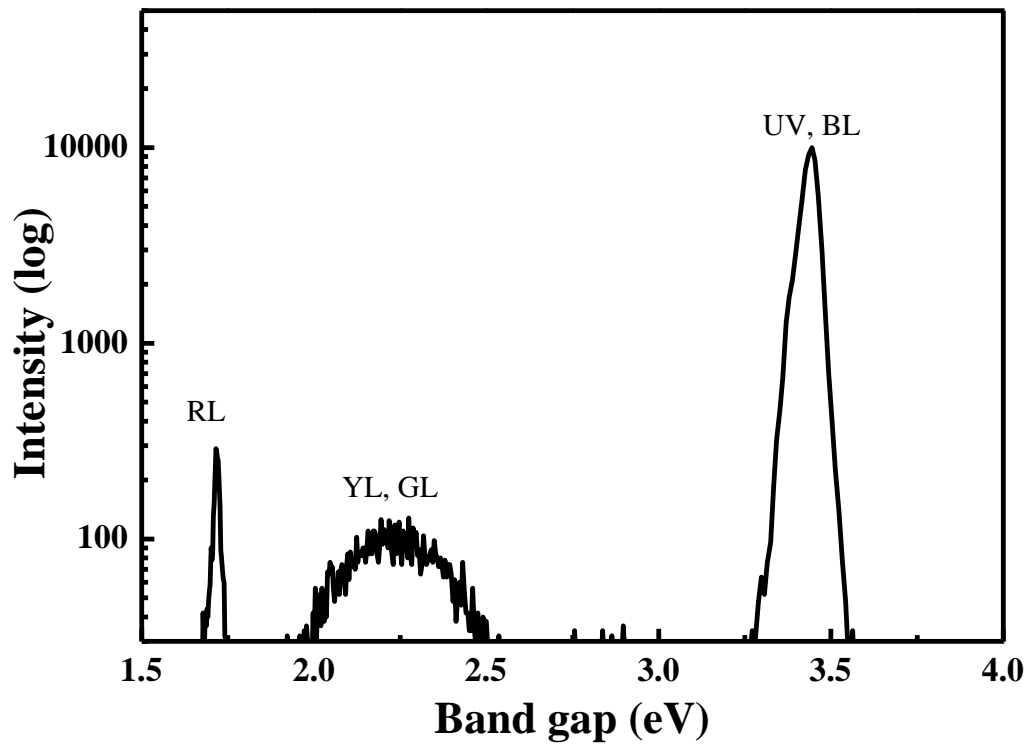


Figure 77 The recorded cathodoluminescence spectrum of GaN from NSYSU.

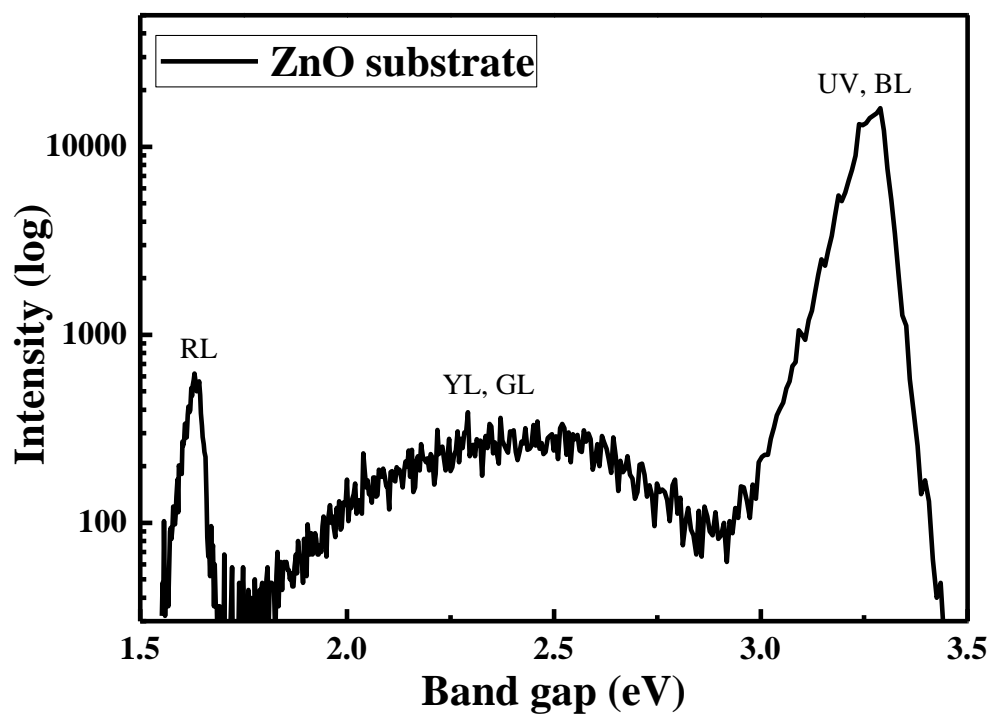


Figure 78 The recorded cathodoluminescence spectrum of bulk ZnO from ISU.

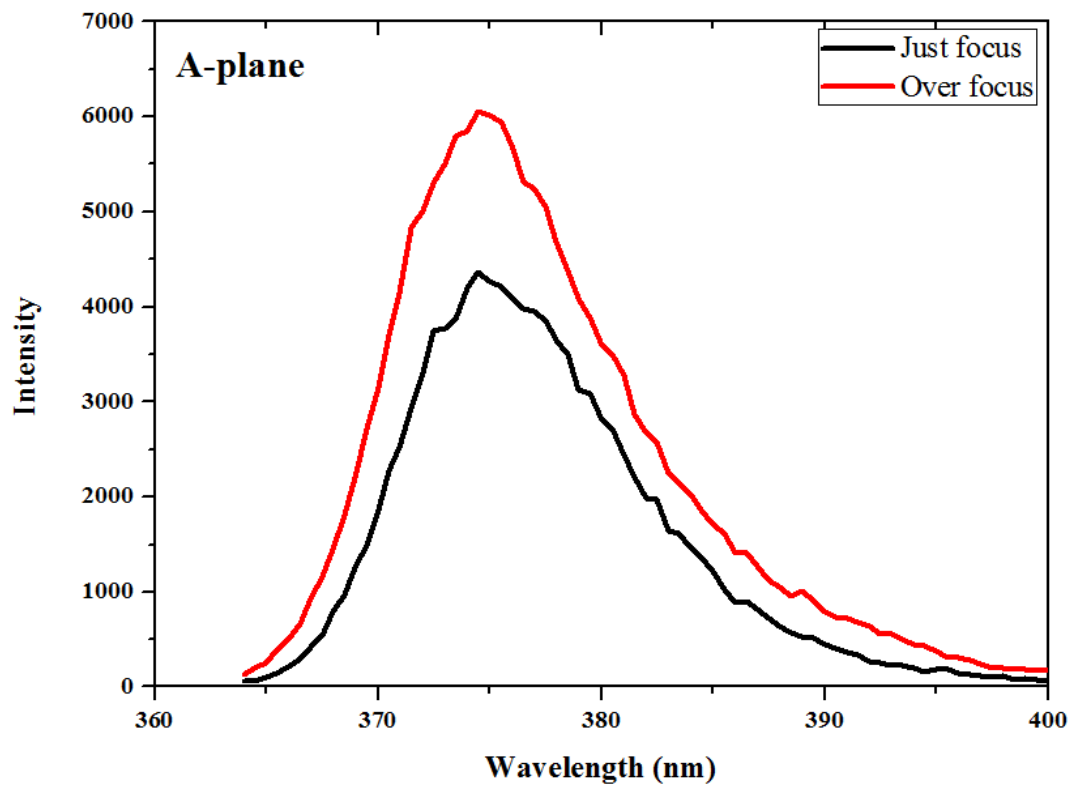


Figure 79 The a-plane ZnO pillar CL spectra of just focus and over focus plane.

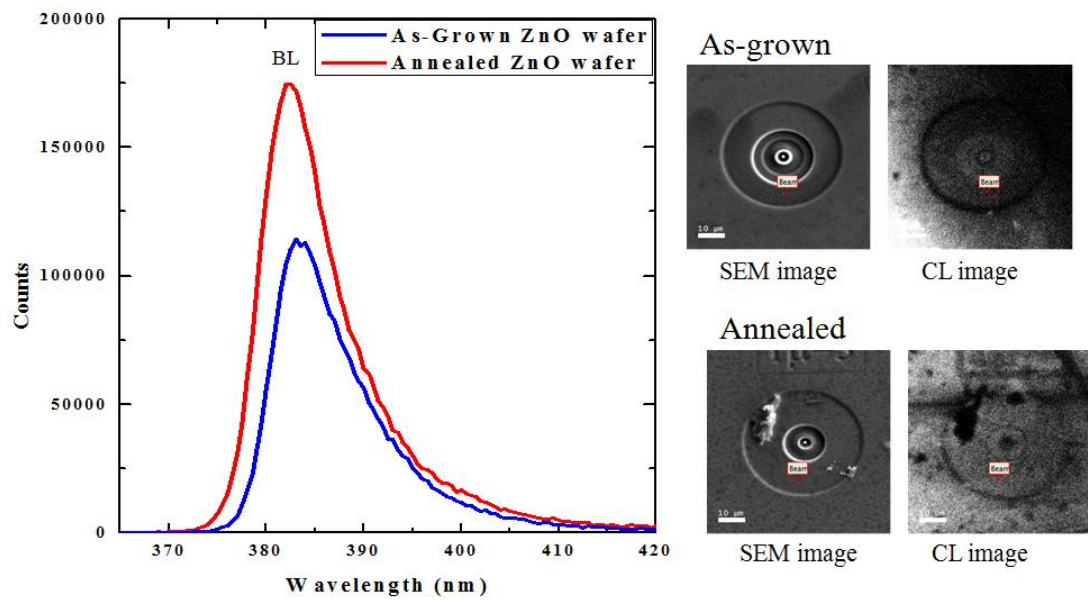


Figure 80 Representative c-plane ZnO CL spectra, and corresponding SEM SEI image and CL image of 383 nm.

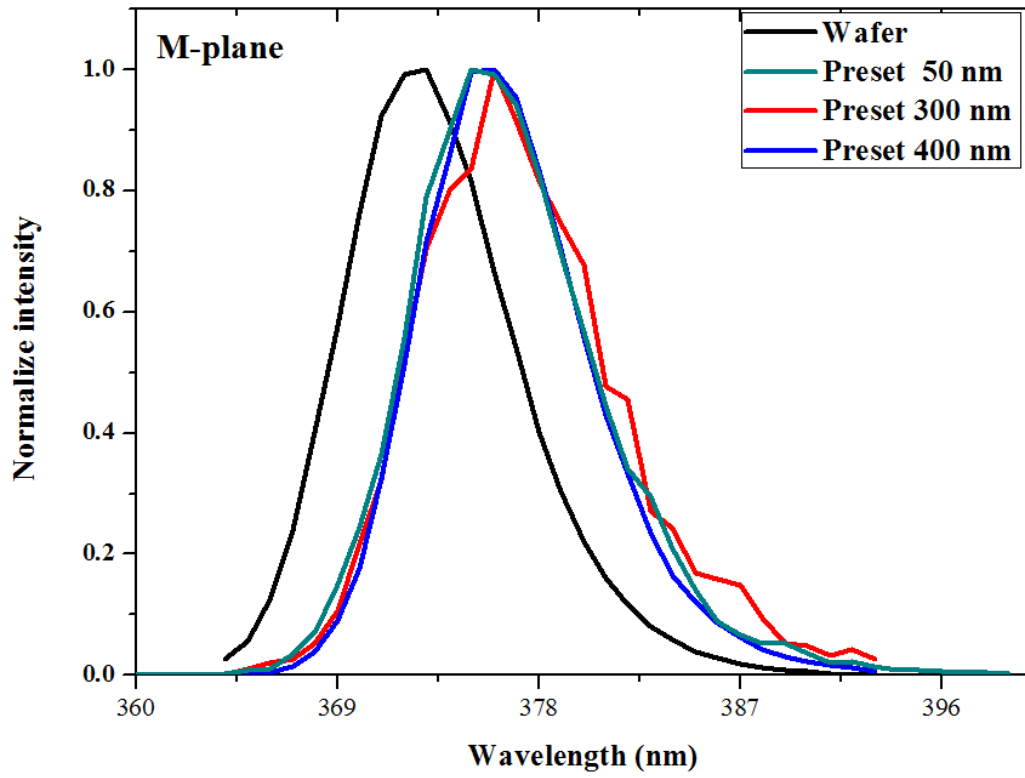


Figure 81 The m-plane ZnO CL spectra of wafer, preset 50, 300 and 400 nm pillars.

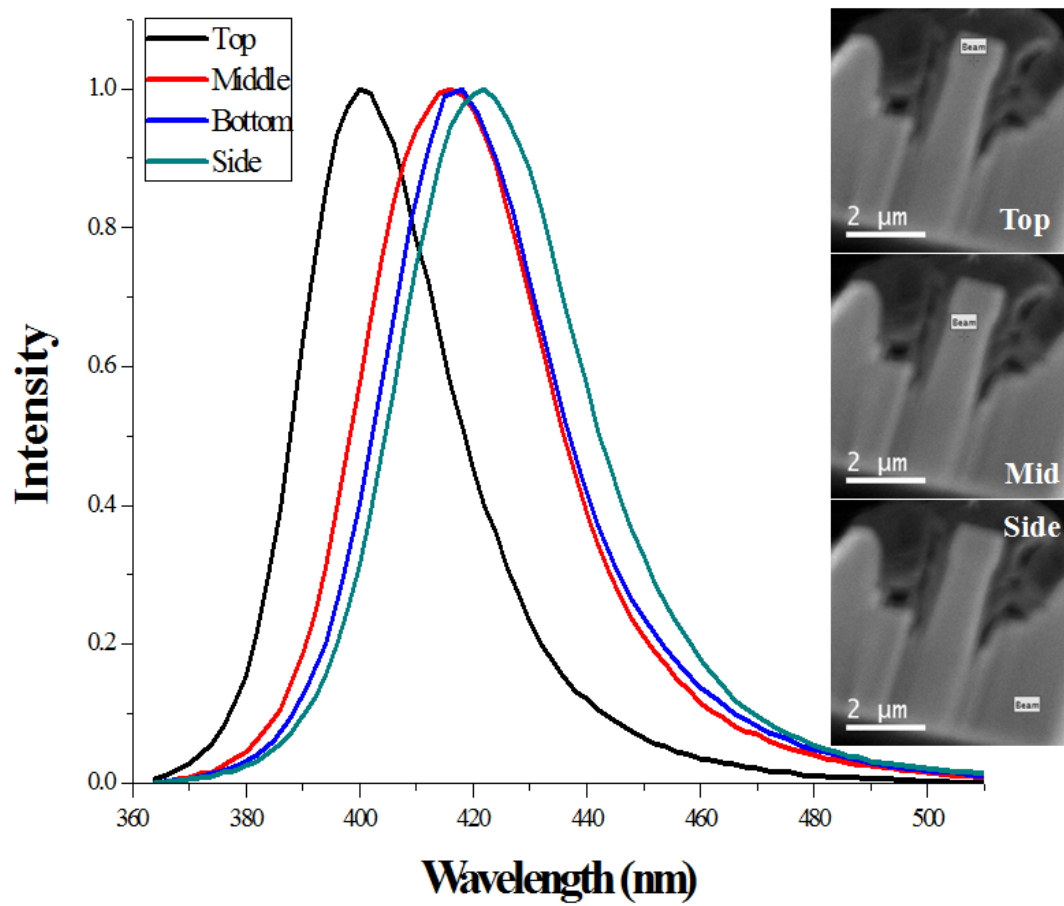


Figure 82 Representative c-plane ZnO X-CL spectra, and corresponding SEM SEI image.

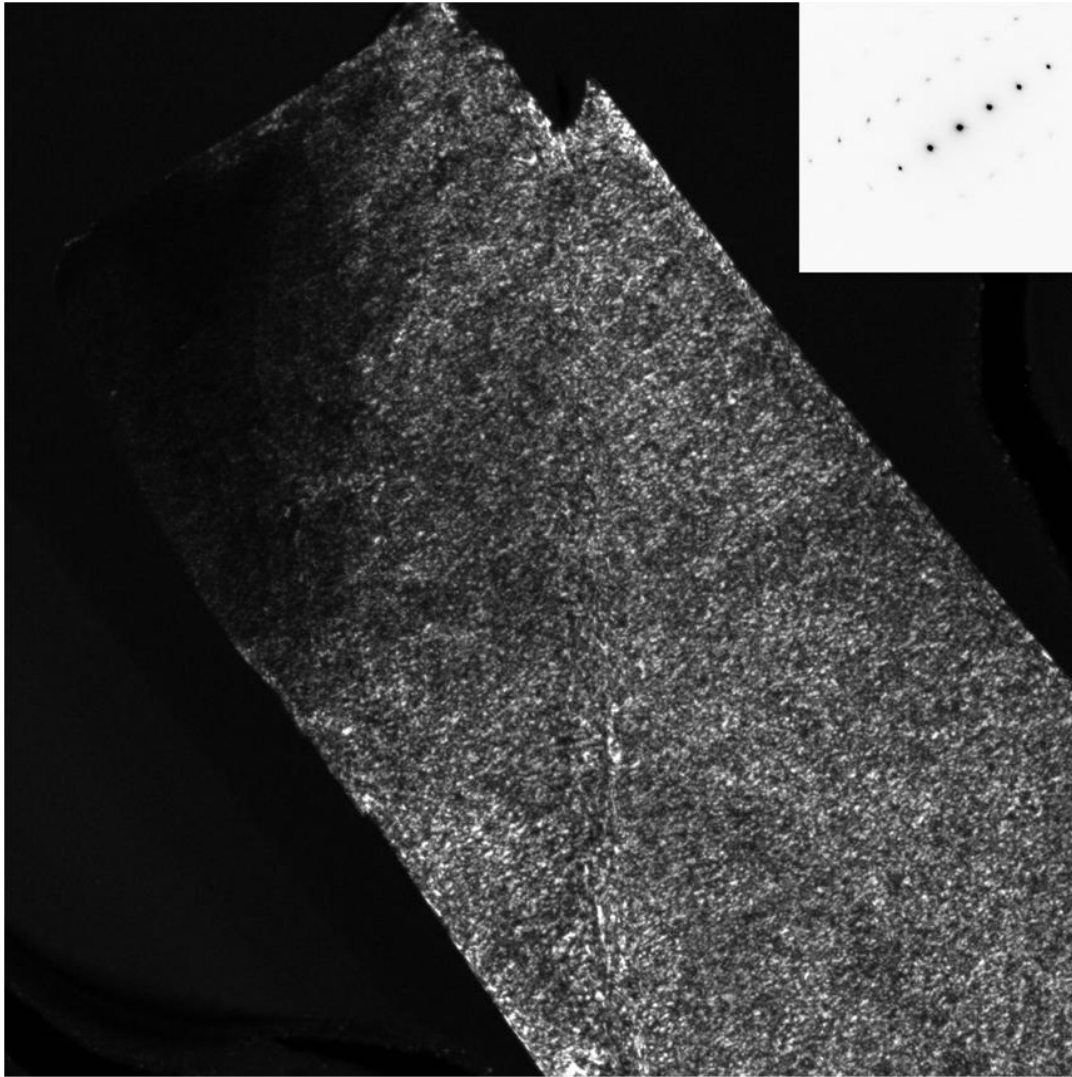


Figure 83 The center dark field (0001) image of c-plane ZnO micropillar, with an indexed zone axis of [0002].